USING ADVANCED MICROSCOPY TECHNIQUES FOR THE STUDY OF MACROPHAGE-CANCER CELL INTERACTIONS IN THE PRESENCE OF THERAPEUTIC ANTIBODIES

APPROVED BY SUPERVISORY COMMITTEE

E. Sally Ward, Ph.D.

Wen-hong Li, Ph.D.

Raimund J. Ober, Ph.D.

Georgios Alexandrakis, Ph.D.

Chandrashekhar Pasare, Ph.D.

DEDICATION

I would like to thank all the people who have inspired and encouraged me during difficult times and allowed the completion of this dissertation.

I am greatly indebted to my lab mentors, Sally Ward, and Raimund Ober, who have been instrumental in guiding me through my graduate studies. They gave me the freedom to pursue things in any direction the science took us, but at the same time taught me important lessons on how science works in a practical world and the compromises one needs to make. Their door was always open for a discussion, and over the years I have learned more from them about science and life than I thought possible. Sripad Ram deserves a special mention, for he too has been my teacher and pseudo-mentor through most of my life in graduate school.

I would like to thank my other committee members Wen-Hong Li, Georgios Alexandrakis and Chandrashekhar Pasare for orienting me through graduate school with a perfect mixture of valuable comments and autonomy. I would also like to dedicate my dissertation to the late Philip Thorpe, who was also part of my committee until his tragic passing in 2013. I shall always remember my interactions with him which have positively shaped this dissertation.

My graduate life also introduced me to many people who have significantly affected how I view science, research and what I want to do in life. My long-time roommates Dilip Challa and Sandeep Kumar Ganji have played instrumental roles in inspiring me to be a better scientist and a better person. They have both questioned many assumptions I had about what a person should do with their life, in their unique way. I also want to thank the other current and past lab mates Sreevidhya Ramakrishnan, Priyanka Khare, Jerry Chao, Siva Devanaboyina, Jeffrey Kang, Sungyong You, Dongyoung Kim, Ran Li, MinGin Kim, Zita Schneider, Anish Abraham, Rafal Swiercz, Marietta Kovacs, Uta Bussemeyer and many more, who have been there for me to either talk science or any other topic, and made my life here a better experience than would have been otherwise. I also want to thank my other roommates Sarath Jupalli, Ganesh Kadamur Bhavani, Virendra Mishra and Sairam Geethanath who have all both voluntarily and involuntarily been part of long discussions about science and life in academia. A special mention to Ramya, who has been supporting me through this journey all along.

My interest in science spans a longer period than my dissertation work., and I would be remiss not to thank my high school teacher Mrs. Nalini, my undergraduate professor Dr. Gautam Pennathur, my undergraduate senior Bala Venkat and my MSc mentors Dr. Jean-Claude Labbé and Dr. Gregory Emery who all have gradually built up my interest in science in ways I shall never forget.

Finally, but most importantly, I dedicate this dissertation to my family. My father is the greatest inspiration of my life, and I chose to do my Ph.D. because of him. I also hope this dissertation will be worth the wait my mother and sister have endured all these years of separation.

USING ADVANCED MICROSCOPY TECHNIQUES FOR THE STUDY OF MACROPHAGE-CANCER CELL INTERACTIONS IN THE PRESENCE OF THERAPEUTIC ANTIBODIES

by

RAMRAJ VELMURUGAN

DISSERTATION / THESIS

Presented to the Faculty of the Graduate School of Biomedical Sciences

The University of Texas Southwestern Medical Center at Dallas

In Partial Fulfillment of the Requirements

For the Degree of

DOCTOR OF PHILOSOPHY / MASTER OF SCIENCE / MASTER OF ARTS

The University of Texas Southwestern Medical Center at Dallas

Dallas, Texas

August 2017

USING ADVANCED MICROSCOPY TECHNIQUES FOR THE STUDY OF MACROPHAGE-CANCER CELL INTERACTIONS IN THE PRESENCE OF THERAPEUTIC ANTIBODIES

Publication No. _____

Ramraj Velmurugan, M.Sc.

The University of Texas Southwestern Medical Center at Dallas, 2017

Supervising Professor: E. Sally Ward, Ph.D.

The use of monoclonal antibodies represents a rapidly expanding area for cancer therapy. One of the main mechanisms of action of these antibodies is Fcγ receptor-mediated engagement of macrophages and other immune cells. When macrophages engage tumor cells opsonized with antibody molecules, they can perform trogocytosis, the process of internalizing fragments of the target cell, or phagocytosis, the internalization of entire cancer cells. This study first establishes whether the process of trogocytosis can lead to cancer cell death. A variety of microscopy and flow cytometric assays were used to quantify the levels of trogocytosis and

cell death, in co-cultures of macrophages and cancer cells. Using HER2-overexpressing breast cancer cell lines and anti-HER2 antibodies, we show that persistent trogocytosis can lead to the killing of cancer cells. The mechanism of trogocytosis was also explored using multifocal plane microscopy (MUM). Imaging the process of trogocytosis using MUM revealed that it proceeds through the macrophage-mediated extrusion of tubular structures of the target cell membrane. This membrane-tubulation results in the preferential uptake of the membrane components from the target cell. The study also investigated the maturation pathway followed by phagosomes containing entire cancer cells. A vacuole-like structure associates with these phagosomes, which whilst also lysosomal in nature, displays characteristics distinct from the phagosome itself. The interface between the vacuole and the phagosome is impermeable to certain solutes as observed through microscopy. Further, the size of the phagosome-associated vacuole is affected by inhibition of the mTOR pathway. Use of advanced microscopy techniques such as MUM in these and other biological problems provides mechanistic insight at the spatiotemporal level. To further develop the algorithms involved in MUM data processing, I have therefore also explored various non-parametric methods of estimating the axial location of point sources from MUM data. A new non-parametric method is proposed, which uses multiple intensities calculated from each image of a point source in MUM data. The performance of this approach is compared with other non-parametric methods through simulations and Fisher information calculations. The effectiveness of this method on experimental data is also evaluated.

TABLE OF CONTENTS

PRIOR PUBLICATIONS

PEER-REVIEWED RESEARCH ARTICLES

1. Li R, Chiguru S, Li L, Kim D, Velmurugan R, Kim D, Devanaboyina SC, Tian H, Schroit A, Mason R, Ober RJ, Ward ES. (2017) Targeting phosphatidylserine with calcium-dependent protein-drug conjugates for the Treatment of Cancer. **Mol Cancer Ther** *(in press).*

2. Velmurugan R, Chao J, Ram S, Ward ES, and Ober RJ. (2017) Intensity-based axial localization approaches for multifocal plane microscopy. **Optics Exp** 25(4): 3394-3410.

3. Velmurugan R, Challa DK, Ram S, Ober RJ, Ward ES. (2016) Macrophage-mediated trogocytosis leads to death of therapeutic antibody-opsonized tumor cells. **Mol Cancer Ther** 15(8):1879-89.

4. Bansal P, Khan T, Bussmeyer U, Challa DK, Swiercz R, Velmurugan R, Ober RJ, Ward ES. (2013) The encephalitogenic, human myelin oligodendrocyte glycoprotein-induced antibody repertoire is directed toward multiple epitopes in C57BL/6-immunized mice**. J Immunol** 191(3): 1091-101.

CONFERENCE PROCEEDINGS

1. Chao J, Velmurugan R, You S, Kim D, Ward ES and Ober RJ. (2017) Remote focusing multifocal plane-microscopy for the imaging of 3D single molecule dynamics with cellular context. **Proc SPIE** 10070: 10070L.

2. Lin D, Lin Z, Velmurugan R, Ober RJ. (2017) Automatic endosomal structure detection and localization in fluorescence microscopic images **IEEE Trans Circuits Syst 2017**.

REVIEWS & BOOK CHAPTERS

1. Challa DK, Velmurugan R, Ober RJ, Ward ES. (2014) FcRn: from molecular interactions to regulation of IgG pharmacokinetics and functions. **Curr Top Microbiol Immunol** 382:249-72.

2. Ward ES, Velmurugan R, Ober RJ. (2014) Targeting FcRn for therapy: from live cell imaging to in vivo studies in mice. **Immunol Lett** 160(2): 158-62.

LIST OF FIGURES

LIST OF DEFINITIONS

2D – Two Dimensions

3D – Three Dimensions

ADCC – Antibody Dependent Cellular Cytotoxicity

ADCP – Antibody Dependent Cellular Phagocytosis

ADE – G236A/S239D/I332E

AE – G236A/I332E

A/I – Activatory to Inhibitory

ANOVA – ANalysis Of VAriance

ATCC – American Type Culture Collection

CDC – Complement Dependent Cytotoxicity

CFSE – CarboxyFluorescein Succinimidyl Ester

CH – Constant Heavy chain

CHO – Chinese Hamster Ovary

CLL – Chronic Lymphoblastic Leukemia

CSF – Colony Stimulating Factor

DIC – Differential Interference Contrast

DMEM – Dulbeco's Modified Eagle Medium

DMSO – DiMethyl SulfOxide

EMCCD – Electron Multiplying Charged Coupled Device

FCS – Fetal Calf Serum

FcγR – Fcγ Receptors

FITC – Fluorescein IsoThioCyanate

GFP – Green Fluorescent Protein

IFN - InterFeroN

ITAM – Immunoreceptor Tyrosine-based Activation Motif

IVIG – IntraVenous ImmunoGlobulin

LPS - LipoPolySaccharide

MFI – Mean Fluorescence Intensity

MHC – Major Histocompatibility Complex

MILA – Multi Intensity Lookup Algorithm

MUM – MUltifocal plane Microscopy

MUMLA – MUltifocal plane Microscopy Localization Algorithm

NK – Natural Killer

PBS – Phosphate Buffered Saline

PLAM – Practical Localization Accuracy Measure

PRR – Pathogen Recognition Receptor

PSF – Point Spread Function

ROI – Region Of Interest

SPB-PLAM – Single Pixel-Based Practical Localization Accuracy Measure

TEM – Transmitted Electron Microscopy

TRITC – Tetramethyl Rhodamine IsoThioCyanate

VH – Variable Heavy chain

VL – Variable Light chain

WCP – Whole Cell Phagocytosis

CHAPTER ONE

GENERAL INTRODUCTION

1.1 ANTIBODY THERAPY OF CANCER

1.1.1 Antibody structure and function

Antibodies are relatively large protein molecules that are produced by the immune system to fight pathogens in the body [1]. These Y-shaped molecules consist of four polypeptide chains: two “heavy chains” and two “light chains” both of which have variable regions while the heavy chain also contains a constant region. Immunoglobulin G (IgG) is the most abundant class of antibody molecules, the other classes being IgA, IgD, IgE and IgM. The variable regions of the two chains in IgG molecules (Variable Light, VL and Variable Heavy, VH) bind to the antigen recognized by the antibodies (Figure 1-1). The constant regions (Constant Heavy chains CH1, CH2, and CH3) serve to engage other receptors which elicit the function of the antibody or determine its pharmacokinetic and immunological properties. The variable region of the antibody molecule is uniquely generated in each B cell through a process called V(D)J recombination. Through a series of cell-cell interactions and signaling, the adaptive arm of the immune system orchestrates the selection and proliferation of clones of differentiated B cells termed plasma cells that produce antibody molecules with VL & VH region sequences that bind a given antigen [1]. The affinity of these antibodies for their antigen is further increased through a process called affinity maturation [2]. The constant regions remain unchanged, although each species has several antibody isotypes with constant region sequences which have different levels of immune system engagement. The glycosylation patterns in the constant region may also be modified, further affecting the levels of engagement of various cells of the

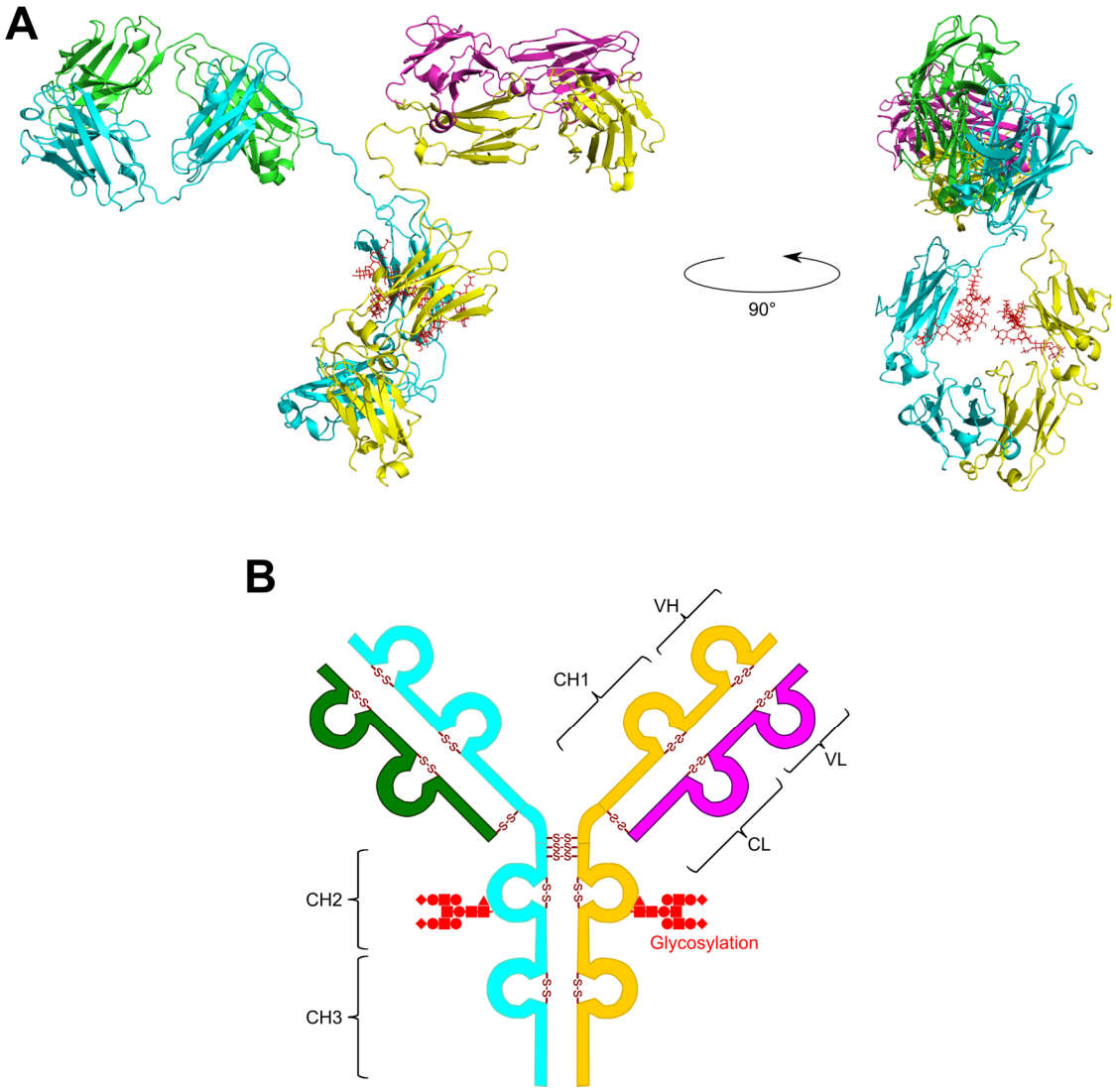

Figure 1-1 The structure of an antibody molecule

A, Structure of a typical IgG antibody molecule (Protein data bank ID 1IGT) shown from two angles. Atomic bonds depicted in red comprise the glycosylation in the constant region. B, a schematic illustration of the domains of the antibody molecule, with chains colored similarly as in the protein structure shown above. Disulfide bonds are depicted by -S-S- linkages.

immune system. The primary functions of the constant region of the antibodies are twofold:

1. Binding sites in the constant region of the antibodies recruit the immune system to bound antigen through Fcγ receptors and complement. Fcγ receptors are found on the surface of numerous types of immune and non-immune cells. These receptors can be broadly classified first into activatory and inhibitory receptor types, based on whether the engagement of the receptor activates or inhibits the inflammatory state of the effector cell, and further classified into low affinity and high affinity binders.

2. The constant region also extends the in vivo half-life of the antibody molecule by binding to the recycling Fc receptor FcRn [3], which can salvage the antibody from lysosomal degradation when the antibody is nonspecifically taken up by fluid phase in various cells.

1.1.2 Antibody therapy of cancer

In 1975, Köhler and Milstein created hybridoma technology [4], where plasma cells isolated from immunized animals are fused with immortalized cells. This process creates immortalized hybridoma cells that can be cloned and produce antibody molecules of the same sequence, also known as monoclonal antibodies. Consequently, it became possible to produce large amounts of 'clonal' antibodies directed against the desired antigen. If tumor-specific antigens could be identified, then monoclonal antibodies against these tumors could function as potential therapeutic interventions. Initial attempts in using monoclonal antibodies of murine origin as therapies faced issues with immunogenicity and short in vivo half-lives [5,6]. However, strategies to produce 'chimeric' or 'humanized' antibodies succeeded in reducing these effects

[7-11]. Rituximab, an antibody specific for the B cell-specific receptor CD20, was one of the first chimeric monoclonal antibodies to be approved for clinical use and is now used to treat a variety of autoimmune diseases in addition to the treatment of hematological cancers [12]. Trastuzumab, a humanized antibody specific for the growth receptor HER2, has also become the standard of care for breast cancers overexpressing HER2 [13]. More therapeutic antibodies have since been developed against HER2, CD20, and multiple other targets. Antibody mediated therapy has become one of the most promising methods to treat cancer and several other disorders, with more than 70 monoclonal antibodies expected to be approved for clinical use by 2020 [14].

1.1.3 Mechanism of action of antibody therapies

While antibody therapies have been successful in treating different cancers, the exact mechanisms of action of these therapies have not been established. HER2 positive breast cancer cells display enhanced proliferative rates due to the signaling induced by HER2 overexpression. Hence, inhibition of this pathway can lead to a block in proliferation, resulting in tumor regression. Such an inhibition of HER2 signaling is considered to be one of the main mechanisms of trastuzumab therapy [15]. However, the trastuzumab molecule can also elicit immune mediated functions with its Fc region. Three immune mediated mechanisms are commonly considered possible candidates for cancer cell killing:

1.1.3.1 Antibody-dependent cellular cytotoxicity (ADCC)

ADCC is the process of cell killing induced by Natural Killer (NK) cells. NK cells have Fcγ receptors which can bind to antibody-opsonized cells and kill them through targeted release of

enzymes such as perforin and granzyme in the cell-cell synapse. ADCC levels elicited by the NK cells of a patient have been shown to correlate with the outcome of trastuzumab therapy, strongly indicating that ADCC could play a major role in the mechanism of action of treatment with this antibody [16,17].

1.1.3.2 Complement-dependent cytotoxicity (CDC)

The complement system consists of a group of soluble proteins found in the serum, which can engage antibody-opsonized particles and aid in their clearance. Antibody-opsonized cells can recruit components of complement which can cause their cell death through CDC. Rituximab-mediated therapy is considered to be at least partly mediated through CDC [18,19]. However, the role of complement in the mechanism of action of other therapeutic antibodies has not yet been established.

1.1.3.3 Antibody-dependent cellular phagocytosis (ADCP)

ADCP is the process through which macrophages and other phagocytes engulf entire cells that have been opsonized with antibodies and degrade them. In vitro studies have clearly established that macrophages of several distinct differentiation states can effectively engulf and degrade antibody-opsonized cancer cells [20,21]. In vivo studies have shown the existence of ADCP synapses in mice [22], the engulfment of circulating tumor cells by macrophages [23] and the critical role of ADCP in the clearance of at least certain tumor types [24]. These and other studies have begun to underscore the importance of ADCP for antibody-mediated tumor therapy [25]. This interest has gained importance only recently because macrophages were traditionally considered to be poor prognosticators of tumor outcomes. In the absence of

opsonizing therapeutic antibodies, macrophages found in the tumor assist in its progression by enabling an immunosuppressive environment and facilitating tumor cell extravasation leading to metastasis. However, macrophages can also elicit ADCP in the presence of opsonizing antibodies. Hence, it can be expected that antibody therapy could reverse the prognostic correlation of tumor outcomes and macrophage infiltration levels. Preliminary clinical reports support this hypothesis [26], with further support from studies in mouse models [27].

1.1.4 Engineering therapeutic antibodies for enhanced engagement with the immune system

Given the importance of immune-mediated effector functions for antibody therapeutics, there has been considerable effort towards engineering antibodies with enhanced engagement with these systems [28,29]. The engineering of antibodies has primarily been focused on manipulating their activatory to inhibitory (A/I) ratio, i.e., the ratio of affinities with which the molecules bind activatory Fcγ receptors to their affinities towards inhibitory Fcγ receptors. For tumor therapy, the goal in these engineering approaches is to increase the affinity of the antibodies to activatory Fcγ receptors found on NK cells and macrophages. Two methods are predominantly used to increase these affinities: First, engineering the glycosylation in the antibody constant regions to enhance Fcγ receptor engagement has been successful, with the approval of therapeutic antibodies from two separate glycoengineering platforms for use in the treatment of hematological malignancies [30,31]. Second, investigators are also pursuing the enhancement of these effector functions through modulation of the amino acid sequences in the antibody constant region [32-35]. The most pronounced enhancement in affinity has been observed when different combinations of these mutations are used: G236A, S239D, A330L

and I332E [32,33,36]. The combination of all these mutations, termed in literature as GASDALIE, has been shown to confer enhanced antibody effector function [37,38]. Studies have also explored the enhancement of effector functions by removing all glycosylation from the constant antibody region followed by addition of further mutations [39,40], although the stability and immunogenicity of these antibody variants require further exploration [41]. Thus, considerable interest has been dedicated towards modulating the interactions between therapeutic antibodies and Fcγ receptors. Such interest further underscores the importance of understanding the various processes through which Fcγ receptors interact with these antibodies.

1.2 PHAGOCYTOSIS

Cells of most eukaryotic organisms can perform the process of phagocytosis, which involves the engulfment and subsequent digestion of large particulate matter. The targets of this phagocytic process include debris, invading pathogens, and dying cells. The mechanisms underlying phagocytosis has been a subject of study throughout the past century. This process was initially identified and examined in detail by Metchnikoff in the 19th century [42,43]. The process of phagocytosis is primarily performed by specialized cells categorized as phagocytes. Macrophages represent an important class of such phagocytes in the mammalian immune system. Phagocytes use a variety of surface receptors to identify varied types of targets. These receptors include pattern recognition receptors that detect pathogens, receptors for phosphatidylserine that detect apoptotic cells, and receptors for antibody molecules that detect particles opsonized with antibodies [44,45]. Once the receptors have identified a target, the phagocyte reorients itself and initiates membrane remodeling processes to wrap the particle with its outer membrane. Following uptake of the particle into the cell, the phagocyte acidifies the "phagosome" through the fusion of degradative compartments called lysosomes [46]. These lysosomes contain enzymes that degrade the main classes of biochemical compounds which typically make up living systems [47]. Consequently, the degraded contents from this process are released by the cell as nutrients. In most cases, phagocytosis also induces changes in the inflammatory state of the phagocytic cell since the engulfment of large particulate matter coincides with a requirement for an immunological response [44]. These immune responses can be either activatory (if the target is detected to contain molecular motifs of foreign origin) or inhibitory (if the target is detected to arise from regular physiological processes) in nature.

1.2.1 Receptors involved in phagocytosis

The receptors involved in eliciting phagocytosis can be classified based on the type of their targets [48]:

1.2.1.1 Opsonic receptors

The opsonic receptors primarily include the Fc receptors, which bind antibody molecules with different affinities across a wide variety of immune and nonimmune cell types [49]. The important classes of opsonizing Fc receptors include the Fcα receptors which bind the IgA class of immunoglobulin antibodies and are involved in the regulation of mucosal immunity [50] and the Fcε receptors which bind the IgE class of immunoglobulins involved in defenses against allergens and parasites [51]. However, the primary class of Fc receptors involved in phagocytosis are the Fcγ receptors, which bind the immunoglobulin G (IgG) class of antibodies, the most important and diverse class of antibodies in the immune system [52-54]. While FcγRI receptors in humans and FcγRI/FcγRIV receptors in mice have a high affinity towards IgG molecules, other Fcγ receptors have a lower affinity. This enables these receptors to selectively engage only when a sizeable particle is opsonized with multiple antibody molecules, making them highly selective phagocytic receptors. The typical targets that are opsonized by antibody molecules are pathogens which have elicited an antibody response from the humoral immune system. Targets of a cellular origin have also become an important area of study with respect to Fcγ receptor-mediated phagocytosis, due to the recent advent of monoclonal antibody therapeutics. Another class of opsonic receptors is the complement receptors, which may also opsonize a target in an antibody-dependent or independent manner and recruit macrophages to engulf these particles [55-57].

1.2.1.2 Pattern recognition receptors

Pattern recognition receptors (PRRs) have evolved to detect conserved pathogen-associated molecular patterns and cellular stresses [58]. PRRs include multiple families of receptors, which recognize different ligands and have different cellular localizations. For example, Toll-like receptors recognize pathogen-associated proteins, sugars or nucleic acids and are localized either on the cell membrane or in the endocytic compartments. The engagement of these receptors by their respective ligands results in the activation of the cells expressing these PRRs which can directly attack the encountered pathogen or prime other immune cells to coordinate the fight against the pathogen.

1.2.1.3 Apoptotic corpse receptors

Apoptosis is a programmed process of cell death that is conserved among all multicellular organisms [59]. This process is vital for the normal functioning of these organisms and an important step in this process is the clearance of apoptotic bodies. Hence, cells undergoing apoptosis and the cells that clear apoptotic bodies have evolved a complex repertoire of signaling molecules and receptors to coordinate this process. Exposure of phosphatidylserine (PS) in the outer leaflet of dying cells is one of the primary signals for phagocytes to engulf them, and hence phagocytes have several receptors that directly or indirectly detect PS to engulf the corpses.

1.2.2 Formation of the phagosome

Once the appropriate receptors in the phagocyte have engaged the target particle, a complex yet orchestrated cell biological pathway leads to the engulfment of the particle to form the

phagosome [45]. The clustering of phagocytic receptors is considered to be an essential prerequisite for the formation of the phagocytic cup. This clustering leads to downstream signaling that induces several processes including phosphorylation of the immunoreceptor tyrosine-based activation motif (ITAM) by Src-family kinases, followed by the recruitment of the kinase Syk, further downstream signaling, and cytoskeletal remodeling [60]. This signaling cascade is essential for successful completion of phagocytosis since the phagocytic targets are often large enough that the effector phagocyte must actively remodel its plasma membrane to completely engulf the target cell. The main signaling steps of this phagosome formation process include the active control of the lipid composition of the phagocytic cup and its surrounding areas, and the coordinated signaling through the Rho family of GTPases. These GTPases consequently coordinate the remodeling of the actin cytoskeleton to assist the engulfment of the target.

1.2.3 Phagosome maturation

Once the phagosome has formed, its contents are degraded through the sequential merging of the endosomal organelles of the cell. The phagocyte eventually delivers enzymes contained in its lysosomes, which can degrade the contents of the phagosome to its biochemical constituents [61]. At this stage, the phagosome is referred by the term phagolysosome, to indicate its similarity in composition and biochemical state to lysosomes. One of the characteristics of this maturation process is the gradual acidification of the phagosome through the action of the vacuolar (H+)-ATPase [62]. While acidification is observed in most phagocytosis studies, the degree of acidification can vary depending on the cell type performing phagocytosis. Dendritic cells for example acidify their phagosomes to a lower extent compared with macrophages,

which permits the preservation of the antigens from the target and their subsequent presentation as peptides on major histocompatibility complex (MHC) class I and II molecules [63].

1.3 TROGOCYTOSIS

The process of trogocytosis derives its name from the ancient Greek word 'trogo' which means to gnaw or nibble. Accordingly, trogocytosis describes the process by which phagocytes internalize small parts of their target instead of completely engulfing them [64]. This process was first observed when Griffin and colleagues studied the mechanisms of phagocytosis using macrophages as effector cells and antibody-coated lymphocytes as targets [21]. While they noted that macrophages completely engulfing the target cells was the primary outcome in these interactions, electron micrographs of "synapses" formed between the macrophages and target cells revealed that often, small parts of the membrane of the target cells were ingested by the macrophages. Antibody-mediated trogocytosis was not studied further until the advent of monoclonal antibodies as therapeutics [12,65]. The therapeutic monoclonal antibody rituximab targeted the CD20 antigen expressed on lymphoma cells. The success of this antibody therapeutic in the treatment of lymphoma and the anti-HER2 antibody therapeutic trastuzumab in the treatment of HER2 positive breast cancers heralded the new era of using monoclonal antibodies against specific surface targets as therapeutics [66]. However, Taylor and colleagues noticed that when rituximab was used in the treatment of chronic lymphocytic leukemia (CLL), another blood cancer, the target receptor CD20 is rapidly removed from the surface of leukemia cells through trogocytosis, without affecting their viability [67]. Subsequent studies revealed that this reduction was due to the 'shaving' or trogocytosis of antibody bound to CD20 by circulating monocytes [68].

While it was identified that trogocytosis could occur on several types of antibody-opsonized target cells including solid tumor cells [69], the therapeutic consequence of this process was

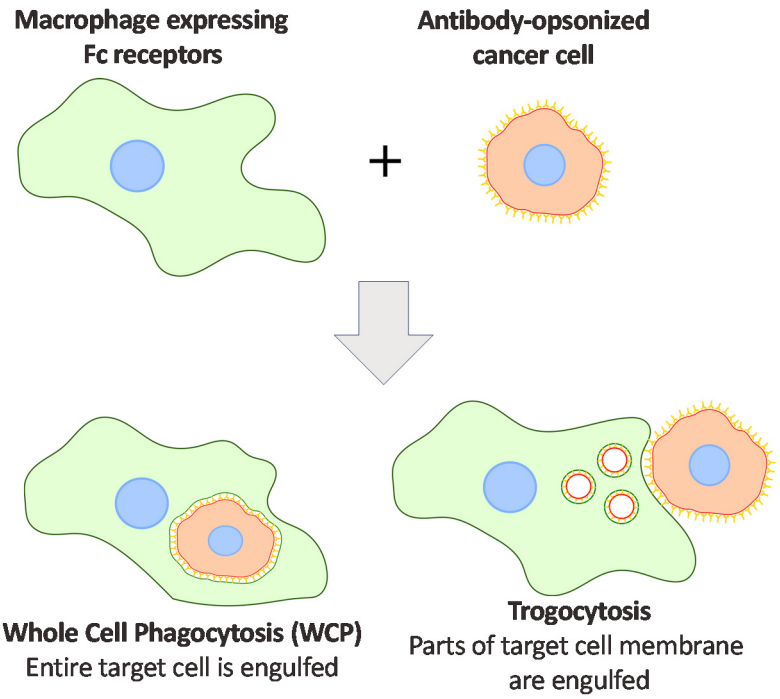

Figure 1-2: Illustration of difference between whole cell phagocytosis and trogocytosis

only studied in CLL. Further, trogocytosis was identified as a hindrance to favorable outcomes in CLL therapy, since the consequence of trogocytosis is that the cells are left unaffected while both the therapeutic antibody and the target antigen is removed from their surfaces [70]. However, it was noted that the primary reason for this effect could be that CD20 does not play any tumor-promoting roles, and hence its removal would not affect tumor cell survival [71]. Indeed, trogocytosis was observed to be therapeutically beneficial when B cell-dependent autoimmune diseases were treated with an anti-CD22 antibody [72]. This antibody-mediated clearance of CD22 and other receptors from the surface of B cells abrogates their autoimmune pathology. Similarly, trogocytosis may be beneficial in therapies where the antibody targets a receptor that is required for the etiology of the disease, such as HER2 in HER2 positive breast cancers. Whether trogocytosis confers a positive or negative therapeutic effect, it is now recognized as an important process that should be carefully considered as an effector function for any class of therapeutic monoclonal antibody [73].

1.3.1 Clarification of terminology

The term trogocytosis has been used in the literature to describe several similar but distinct processes. This dissertation describes trogocytosis as the process of internalizing the surface proteins and membrane of a target cell in an antibody-mediated manner. However, the same term has also been used elsewhere to describe the process of membrane transfer among immune cells where adjacent immune cells “share” their receptors with each other via membrane bridges [74]. Several others have also described trogocytosis performed by T cells, internalizing the peptide-MHC complexes they are engaging, which is similar to antibody-mediated trogocytosis in the directionality of membrane and receptor transfer [64,75]. A recent

report has also defined a similar gnawing process that is performed by amoeba [76]. While these related processes are referred to by the same name, they appear to have different outcomes on the target and effector cells.

1.4 MULTIFOCAL PLANE MICROSCOPY

1.4.1 Fluorescence microscopy

Fluorescence microscopy is a method where fluorescently labeled molecules in a sample are visualized through a microscope by exciting the sample with light of a particular excitation wavelength and recording the image of the sample using light emitted at a different emission wavelength range [77]. Widefield fluorescence microscopy as applied in biology involves the imaging of a relatively thin biological sample (e.g., a monolayer of cells attached to an artificial substrate or a thin section of tissue embedded in some mounting medium) through a high numerical aperture (n_a) objective lens using a pixelated camera. The optical properties of such a microscope configuration result in the formation of an image of the sample structure at a particular focal depth from the objective lens [78]. Structures in the sample that are not near this focal depth also contribute signal to the image but in a "blurred" manner, the properties of this blurring being a function of the point spread function (PSF) of the microscope. The primary determinants of the properties of the PSF are the design characteristics of the objective lens used, such as its numerical aperture and the wavelength of the light used.

1.4.2 Fast three-dimensional imaging with multifocal plane microscopy

The images acquired in a widefield fluorescence microscope are two-dimensional in nature, due to the optical properties of the compound microscope. However, biological structures and

events can only be meaningfully understood when observed in three dimensions (3D), except in specific circumstances. The plasma membrane of eukaryotic cells cultured on glass or plastic substrates presents a relatively flat two-dimensional surface that is easily visualized with widefield microscopes. Hence, biological processes that occur on or near the plasma membrane have been extensively studied using microscopy. On the contrary, biological processes that occur within a cell (e.g., endocytic trafficking) have not been studied as extensively with similarly high spatiotemporal resolution. To visualize samples in 3D using a widefield microscope, multiple images of the sample must be acquired while physically moving the microscope objective or the specimen to change the focal plane whose image is being acquired. Even with fast acquisition speeds, images acquired in this manner exhibit artifacts due to the time differences between the acquisition of the images at each focal plane.

Multifocal plane microscopy (MUM) was developed to address this necessity to rapidly image biological samples in 3D [79]. In MUM, multiple cameras (or special optics that simulate multiple detectors in a single camera) are used such that the light from the objective lens is divided and redirected towards each camera detector (Figure 1-3). By modifying the optics between the tube lens and the detector, each of these detectors can simultaneously image different focal positions within the sample [79,80]. This method has been used to study the movement of endocytic compartments within a cell in 3D at rapid speeds, capturing novel events previously not observed due to restrictions in acquisition speeds [81,82].

1.5 THREE-DIMENSIONAL LOCALIZATION OF SINGLE POINT SOURCES

1.5.1 The biological utility of single molecule/particle imaging

In the examination of biological samples using microscopy, it is often desirable to design experiments such that the acquired images are of isolated point sources of light. If we acquire the image of an isolated point source using a widefield microscope, we can estimate its location with high accuracy depending mainly on the following factors: the numerical aperture of the objective, the emission wavelength of the fluorophore, the number of photons detected from the fluorophore, the pixelation of the detector and various noise sources in the microscope system [83]. Using the approach of imaging isolated point sources, we can extract insightful spatial information from biological samples by two broadly different methods. In the first method, a biological sample may be labeled sparsely such that only a small number of point sources are located in the field of view of a microscope detector. This allows us to image and estimate their individual locations with high accuracy and track the point sources over time [84]. The other method involves stochastically "switching on" a small subset of fluorophores in a biological sample at a time, so that their position may be estimated with high accuracy. Such estimated information from numerous repetitive acquisitions of different subsets can be combined to form a super-resolved reconstruction of the sample [85-87].

1.5.2 Estimating the 2D location of a point source

Both the single molecule methods described above depend on our ability to estimate with high accuracy the two- or three-dimensional location of a point source from its image. The estimation of the 2D or 3D location of a point source is often performed by fitting the data to a parametric equation that models the image formation process of the microscope. The Airy

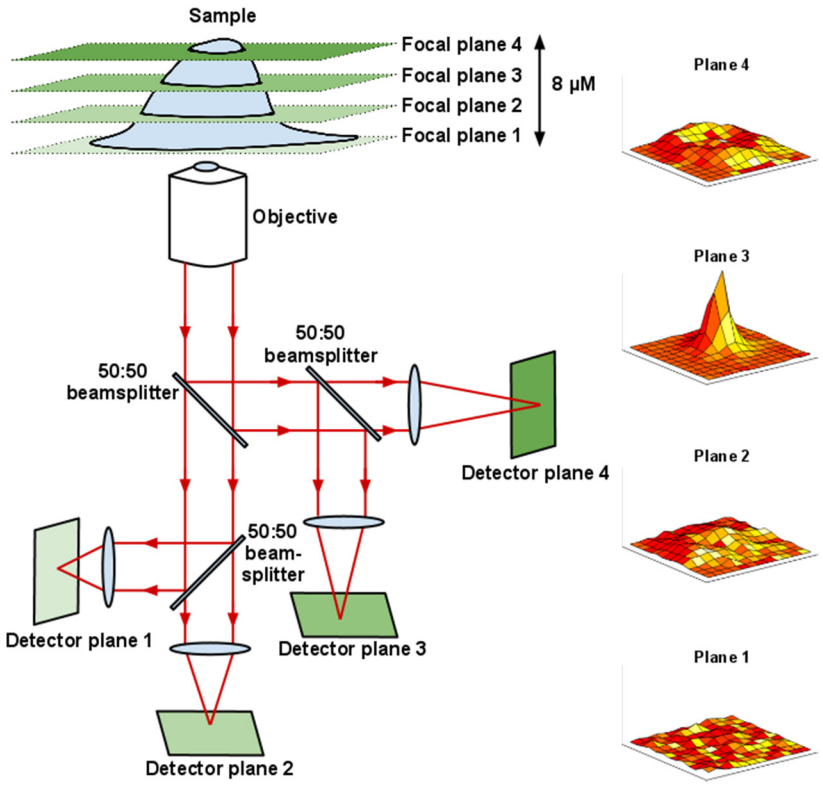

Figure 1-3: Schematic illustration of a MUM configuration imaging four focal planes.

The schematic illustration shows a cellular sample being imaged by an objective in a MUM microscope. The emitted light from the sample is equally split and focused on four detectors. The distance between the tube lens and the detector is changed for each detector allowing them to simultaneously image different focal planes. The panels in the right show intensity plots of images of a typical point source when it is imaged by such a four-plane MUM configuration.

profile is an established expression that approximates the PSF of an in-focus point source. This profile is defined as follows:

$$I(x,y) = A\frac{J_1^2\left(\alpha\sqrt{(x-x_0)^2+(y-y_0)^2}\right)}{\pi((x-x_0)^2+(y-y_0)^2)}.$$

Here I is the intensity at any given position in a detector with coordinates x and y, if the point source is located at (x_0, y_0) in the object space. A and α are parameters that specify the brightness and width of the Airy profile, respectively, and J_1 represents the first order Bessel function of the first kind (a magnification factor has been assumed to take the value of 1 for simplicity).

A more commonly used simple parametric equation that can approximate the PSF of an in-focus point source is the 2D Gaussian equation,

$$I(x,y) = Ae^{-\left(\frac{(x-x_0)^2+(y-y_0)^2}{2\sigma^2}\right)},$$

where A and σ are parameters that specify the brightness and width of the 2D Gaussian function, respectively. Figure 1-4 shows an illustration of the fitting process and the extraction of the higher accuracy location of the point source using the 2D Gaussian estimation method. While the 2D Gaussian method provides a simple 2D parametric model of the PSF, the Airy function can better recapitulate its properties [88,89].

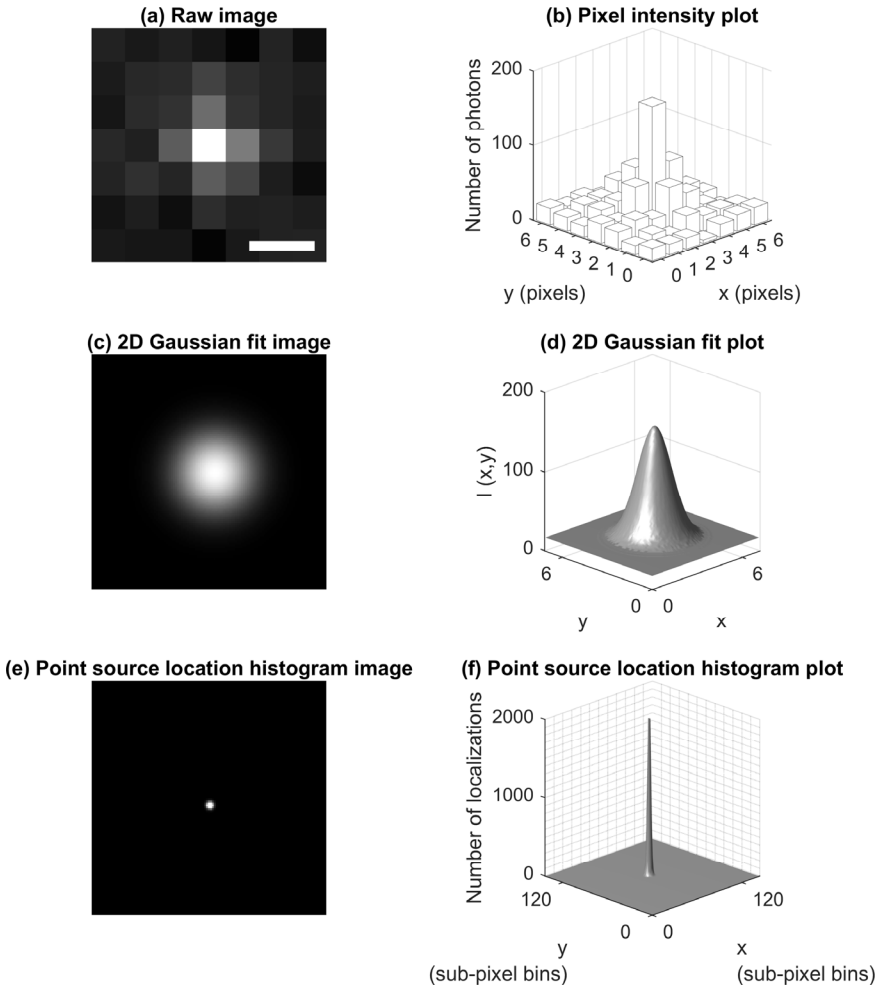

Figure 1-4: Illustration of the estimation of the 2D location of a point source from its image formed in a widefield microscope.

The pixelated grayscale image (a) and the corresponding pixel-intensity plot (b) of a simulated point source as imaged by a compound microscope are shown. (c) and (d) show two visualizations of a 2D Gaussian function whose parameters have been set so that it best fits the raw pixel intensities of the point source shown of (a) and (b). (e) and (f) show two visualizations of a 2D histogram of the locations estimated from repeat images of the point source of (a) and (b), indicating the accuracy with which the location can be estimated. Both panels show the number of localizations that belong to each 2D bin of dimensions 6.5 nm × 6.5 nm. (e) shows the localization density using intensity values that are proportional to the number of localizations in the bins. (f) shows the histogram of localization densities as a smooth 2D surface. Scale bar = 250 nm.

1.5.3 Estimating the 3D location of a point source

While simple parametric equations often provide acceptable estimation results when estimating the 2D location of a point source, similar use of parametric models is complicated when the 3D location of the point source needs to be estimated. The extension of the simple 2D Gaussian equation to the third dimension results in a significant mismatch between model and data [90]. However, appropriate functions exist that parametrically model the 3D image formation process in a microscope. For example, the "Born and Wolf" model is a relatively simple and commonly used function which models the imaging medium as a single layer of uniform refractive index [78]. By contrast, the "Gibson and Lanni" model assumes that the imaging medium is divided into layers of different refractive indices, providing a more realistic representation of the imaging system [91,92].

Another factor affecting the accurate 3D localization of a point source is that determining the axial location of a point source that is near focus is an inherently difficult problem: it has been shown that there is almost no information about the axial location of the point source encoded in its image when the point source is near focus, at least for some PSF models [93]. Hence, the microscope or its PSF has been modified using various approaches to encode more information about the axial location of a point source into the PSF [94-96]. MUM solves the near-focus 3D localization problem by simultaneously acquiring images of the same point source from two or more focal planes. When a point source is near focus on one focal plane of a MUM configuration, it is out of focus in other focal planes. Hence, images acquired from different focal planes can complement each other and synergistically provide a consistent amount of information about the axial location of the point source for point sources located at different

axial positions [97]. An optimization algorithm termed the MUM-Localization Algorithm (MUMLA) has been proposed and verified, which can apply any of the above-mentioned parametric functions to the image data of a point source from a MUM configuration, and estimate its 3D location [96,98]. Assuming that the PSF model used is a reasonable approximation of the PSF of the microscope, MUMLA has been shown to potentially provide the best theoretically possible localization accuracy [96].

However, the implementation of such parametric models is non-trivial and may require careful optimization of parameters used by the algorithm, given the complex minimization landscape presented by these modeling functions. Hence, several groups have used “non-parametric” methods to estimate the axial location of the point source with MUM configurations [99,100]. These non-parametric methods utilize the observation that the local brightness of the PSF changes as the point source moves in and out of focus [79,99]. These methods generate a lookup table of normalized intensities and use the lookup table to estimate the 3D location of the point source.

1.6 INTRODUCTION TO DISSERTATION

Trogocytosis and whole cell phagocytosis are processes that govern important aspects of antibody-based tumor therapy and hence an improved understanding of these processes would permit the better design of future antibody therapies. The present work aims to study the effect of trogocytosis on target cell viability, the immune cell degradative pathways involved in ingested-target cell material and the development of new microscope image processing algorithms that will assist such studies. The first aim focuses on answering an important question of whether the process of trogocytosis can lead to target cell death and to further understand its mechanism. The second aim focuses on studying the fate of whole cell phagosomes primarily using microscopy techniques. The microscopy techniques used in these aims and other studies depend on the continual development of software and algorithms that allow the appropriate processing of advanced microscopy data. To that end, the third aim focuses on providing a simple solution for an important problem in 3D single molecule microscopy, the rapid estimation of the axial location of a point source.

Aim 1: Study the effect of macrophage-mediated trogocytosis on antibody-opsonized tumor cell numbers and viability

The effect of trogocytosis on the survival of antibody-opsonized cancer cells was studied using microscopic and flow cytometric assays. Flow cytometric analysis was used to measure long-term cancer cell viability in co-cultures with macrophages as well as to distinguish between the levels of phagocytosis and trogocytosis. Long-term microscopy imaging methods were used to study the fate of cancer cells undergoing continuous trogocytosis over several days.

Macrophage model systems that only performed trogocytosis and no phagocytosis were used to study the effect of trogocytosis on long-term target cell viability.

Aim 2: Study the degradative pathways of phagocytosed target cells

The fate of whole cell phagosomes was studied using live imaging microscopy, and a novel vacuole-like structure was identified to be aiding the degradation of large phagosomes containing antibody-opsonized cancer cells. The vacuole structure was characterized using various microscopy modalities.

Aim 3: Develop fast non-parametric 3D tracking algorithms that can assist the tracking of trogosome material in microscopy images of macrophages

The accurate localization of point sources in whole cell 3D microscopy data is a prerequisite for the practical use of this modality. Hence, we identified a non-parametric method of calculating the axial position of a point source to solve the 3D localization problem. We also evaluated its performance in comparison to other parametric methods and advanced microscope configurations. The performance of this algorithm was also tested with real data.

CHAPTER TWO
MACROPHAGE-MEDIATED TROGOCYTOSIS LEADS TO DEATH OF ANTIBODY-OPSONIZED TUMOR CELLS

This study has been published in the journal *Molecular Cancer Therapeutics* [Velmurugan R, Challa DK, Ram S, Ober RJ, Ward ES. (2016) Macrophage-mediated trogocytosis leads to death of therapeutic antibody-opsonized tumor cells. **Mol Cancer Ther** 15(8):1879-89]. It is reprinted here with permission from the American Association for Cancer Research.

2.1 INTRODUCTION

Defining the consequences of the interactions of immune effector cells with cancer cells in the presence of tumor-specific antibodies has direct relevance to both immunosurveillance and cancer therapy. The effects of therapeutic antibodies can include the direct inhibition of cell signaling through growth factor receptor binding and the indirect consequences of tumor cell opsonization and recruitment of effector cells such as macrophages or natural killer (NK) cells [66]. For example, monocytes or macrophages can interact with antibody-opsonized tumor cells and engulf whole cells or internalize fragments of the target cell plasma membrane during phagocytosis or trogocytosis, respectively [23,101-104]. Although the tumoricidal effects of phagocytosis are clear, the effect of trogocytosis is less certain. It has been speculated that trogocytosis can have a positive effect during cancer therapy [104]. Conversely, trogocytosis can result in escape from antibody-dependent cell-mediated cytotoxicity (ADCC), complement-dependent cytotoxicity (CDC) or phagocytic cell death. This mechanism of escape has been extensively studied for anti-CD20 antibodies [70,101,102,105] and involves the depletion of target antigen from the cell surface combined with the exhaustion of effector

pathways. These observations have led to the development of dosing regimens to reduce trogocytosis and minimize the pro-tumorigenic effects during CD20 targeting [73]. However, in different settings, it remains possible that trogocytosis results in tumor cell death. To date, such analyses have been limited by the challenges in distinguishing trogocytosis from phagocytosis in effector:target cell co-cultures. In the current study, we have developed an assay to distinguish these two processes. This assay has been used to investigate whether trogocytosis leads to the attrition of HER2-overexpressing breast cancer cells. Establishment of trogocytosis as a pathway for tumor cell death has implications for strategies to optimize antibody-based therapies.

The involvement of FcγR-expressing effector cells in anti-tumor effects has motivated the use of antibody engineering approaches directed toward the Fc region to enhance FcγR binding affinity [33,34,39,106-108]. However, due to the challenges associated with quantitating trogocytosis, how Fc engineering affects this activity is unexplored. Also, despite the expansion in the development and use of antibody-based therapeutics during the past decade [54,109], the factors leading to the induction of long-lived anti-tumor immunity are ill-defined. Consequently, understanding the mechanisms through which macrophages interact with tumor cells is not only important for Fc engineering but also has relevance to elucidating the subcellular trafficking processes resulting in antigen acquisition and presentation by this antigen presenting cell subset [110,111].

The process of trogocytosis was first visualized by Griffin and colleagues [21] when they observed conjugates between macrophages and antibody-opsonized lymphocytes through

electron microscopy. They observed that endosome-like structures were found inside the macrophages near the synapse that contained material from the lymphocyte surface. Other studies have since attempted to capture the trogocytosis process through live imaging [102,104], and while these studies show the gradual appearance of the trogosomes in the macrophages containing target cell material, these results did not clarify the exact mechanism of trogocytosis. Of interest is the question of how macrophages may "nibble" parts of the target cell membrane without compromising its membrane integrity, which may be the reason why leukemia therapy with CD20 antibodies is not successful [73]. Further, a study has shown a related process of trogocytosis performed by *Entamoeba histolytica* [76] where the amoeba engulfs parts of target cells, but in the process, causes their instantaneous death. It has been shown that this trogocytosis process engulfs not just the membrane of the target cell but also the cytoplasm of the target cell. While the precise ratio of target cell cytoplasm and target membrane engulfed by phagocytes like macrophages has not been established, most studies of this trogocytosis process have only observed material from the target cell membrane being internalized. Hence it becomes important to establish the precise mechanism through which macrophages perform this trogocytosis process to compare it to the trogocytosis performed by other species.

One of the possible reasons for the difficulties in studying this process is the inherent 3D nature of it: to follow the formation of an individual trogosome from the target cell membrane; we need to image the synapse between the macrophage and the cancer cell. However, such macrophages-cancer cell synapses form perpendicular to the imaging plane, increasing the complexity of visualizing the process using conventional two-dimensional microscopy.

Previous studies have visualized the synapse between an NK cell and its target by precisely placing one cell over another [112]. However, they were also limited to studying just the membrane dynamics in the synapse in two dimensions and not the formation of any internalization structures, which would form in a different focal plane.

Multifocal plane Microscopy (MUM), where one can image multiple focal planes of a sample at the same time, is an ideal tool to study this process. The interactions between the macrophages and target cells can be studied in 3D with high temporal resolution as they form naturally, and even if the formation of the trogosome occurs in a different focal plane as the synapse, its formation can be captured given the precise design of the focal planes in the MUM configuration.

In the current study, we have used a novel approach to investigate the ability of macrophages of different sources to carry out trogocytosis and phagocytosis of antibody-opsonized HER2-overexpressing breast cancer cells. The RAW264.7 macrophage cell line very rarely phagocytoses complete cells but has trogocytic activity similar to that of other macrophage types. Combined with analyses of apoptotic markers on opsonized target cells in the presence of both human and mouse macrophages, this behavior has allowed us to demonstrate that trogocytosis can lead to tumor cell death. Of direct relevance to Fc engineering, the enhancement of antibody affinity for FcγRs results in increased trogocytosis and target cell death. Importantly, this higher activity is only manifested in the presence of physiological levels of intravenous gammaglobulin (IVIG). Collectively, these studies indicate that trogocytosis can have tumoricidal effects that are further enhanced by antibody engineering.

2.2 RESULTS

2.2.1 Quantitation of cancer cell killing by macrophages

We initially analyzed the effects of different macrophage cells on the viability of opsonized, HER2-overexpressing breast cancer cells. The co-culture of J774A.1 or RAW264.7 macrophages with MDA-MB-453 or SK-BR-3 cells in the presence of the anti-HER2 antibody, trastuzumab, resulted in ~90% and ~50% decreases in target cell numbers, respectively (Figure 2-1A,B). The efficiency of tumor cell recovery was similar for all co-culture conditions, excluding the possibility that variability in cell harvesting efficiency contributes to the differences in cell numbers (Figure 2-2). Incubation of target cells with trastuzumab alone resulted in ~ 10-20% reduction in cell numbers within 72 hours, consistent with earlier studies [113] (Figure 2-1C), although larger decreases (~50%) were observed following longer incubation times [114]. The significant reductions in cell numbers within 72 hours (Figure 2-1A,B) are therefore due to the presence of macrophages rather than the cytostatic effects of trastuzumab. Similar results were obtained for co-cultures maintained in growth media recommended for either the macrophage or tumor cell lines (Figure 2-1, Figure 2-3). To investigate whether the death of opsonized target cells in the presence of macrophages was due to the release of soluble mediators, cancer cells were cultured for 72 hours in the lower chambers of transwell plates containing macrophage:target cell co-cultures plus trastuzumab in the upper chambers (Figure 2-4). The results demonstrate that macrophage:cancer cell contact is necessary for cell number attrition. Also, treatment of cultures with an inhibitor of oxygen radical generation, edaravone, did not reduce cell death (Figure 2-5).

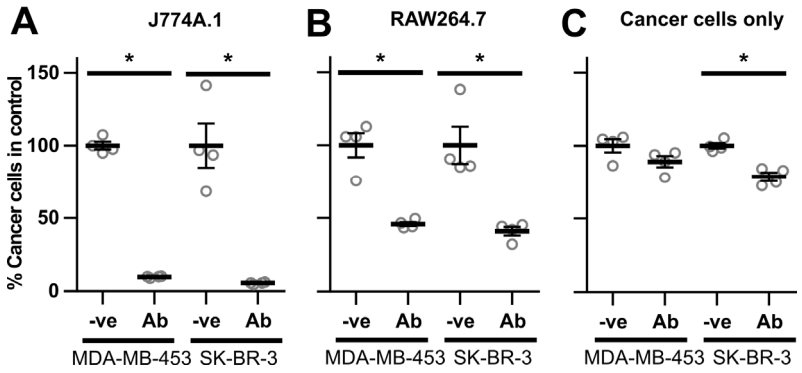

Figure 2-1: Macrophages reduce breast cancer cell viability in the presence of trastuzumab

J774A.1 (A) or RAW264.7 (B) macrophages were plated in 48 well plates with MDA-MB-453 or SK-BR-3 breast cancer cells at a 4:1 effector:target cell ratio (2.5×10^4:6.25×10^3 cells) and 1 μg/ml trastuzumab (Ab) or PBS vehicle (-ve) was added 24 hours later. Following 72 hours, cells were harvested and the remaining number of cancer cells quantitated by flow cytometry. The number of live cancer cells in each sample is shown as a fraction of the corresponding vehicle control. C, cell numbers following incubation of cancer cells as in A,B but without macrophages. Error bars represent standard errors. Student's t-test was performed to indicate statistical significance (denoted by *; $p< 0.05$).

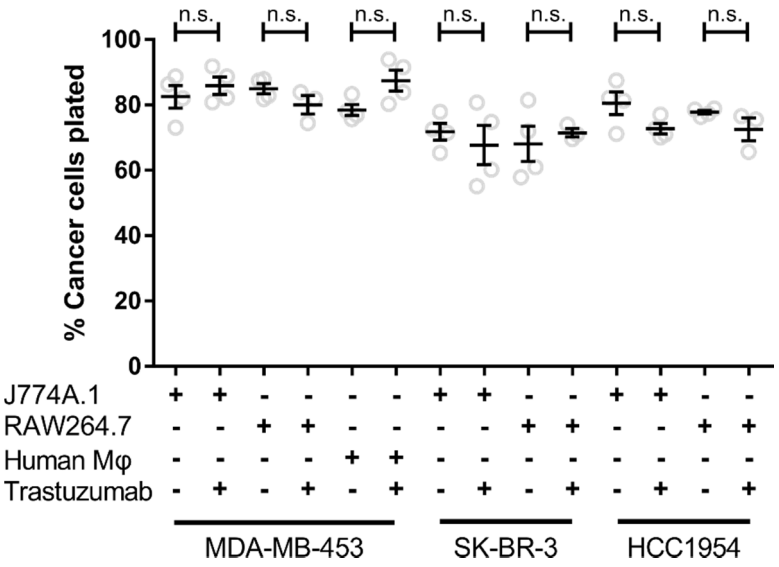

Figure 2-2: Harvesting efficiency of cancer cells in macrophage:cancer cell co-cultures

To label MDA-MB-453, SK-BR-3 or HCC1954 cells, the cancer cells were incubated with 50 μg/ml Alexa 647-labeled dextran overnight (dextran accumulates by fluid phase uptake within the endolysosomal pathway). Labeled cells were harvested, counted in duplicates using a hemocytometer and mixed with macrophages at a 4:1 ratio and plated in 48 well plates, in the presence or absence of 1 μg/ml trastuzumab. Following a 4-hour incubation at 37°C, the cells were harvested into flow cytometry tubes, and 50 μl of a solution containing a defined number of Flow Check beads (counted using a hemocytometer) added to each tube. The samples were analyzed by flow cytometry and the total number of cancer cells harvested from each well was calculated by dividing the number of dextran-positive events by the fraction of added beads counted in each sample. This cell count corresponds to all cancer cells, including those present in macrophage:cancer cell conjugates and in phagosomes inside macrophages. The number of cancer cell events collected was plotted as a fraction of the number of cancer cells plated in the 48 well plates (Mφ = macrophage). Statistically significant differences between samples were determined using one-way ANOVA analysis followed by a Tukey's multiple comparisons test between all the indicated sample pairs. n.s., no significant difference (95% confidence interval).

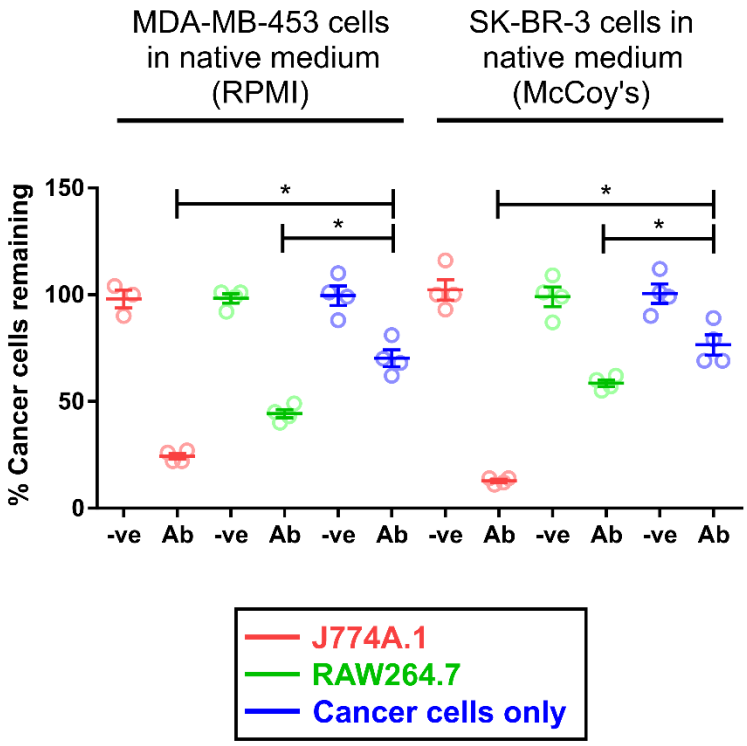

Figure 2-3: Macrophage-mediated reduction of opsonized target cell numbers occurs in media optimized for cancer cell growth

J774A.1 or RAW264.7 macrophages were plated in 48 well plates with CFSE-labeled MDA-MB-453 or SK-BR-3 cancer cells at a 4:1 effector:target ratio (2.5×10^4:6×10^3 cells) with 1 μg/ml trastuzumab (Ab) or PBS vehicle (-ve) and incubated at 37°C in either RPMI-based or McCoy's-based medium for 72 hours. The cells were then harvested and the remaining number of cancer cells quantitated by flow cytometry. The number of live cancer cells in each sample is shown as a fraction of the control. Error bars represent standard errors. Statistically significant differences between samples were determined using Student's *t*-test. * indicates significant differences between samples ($p < 0.05$).

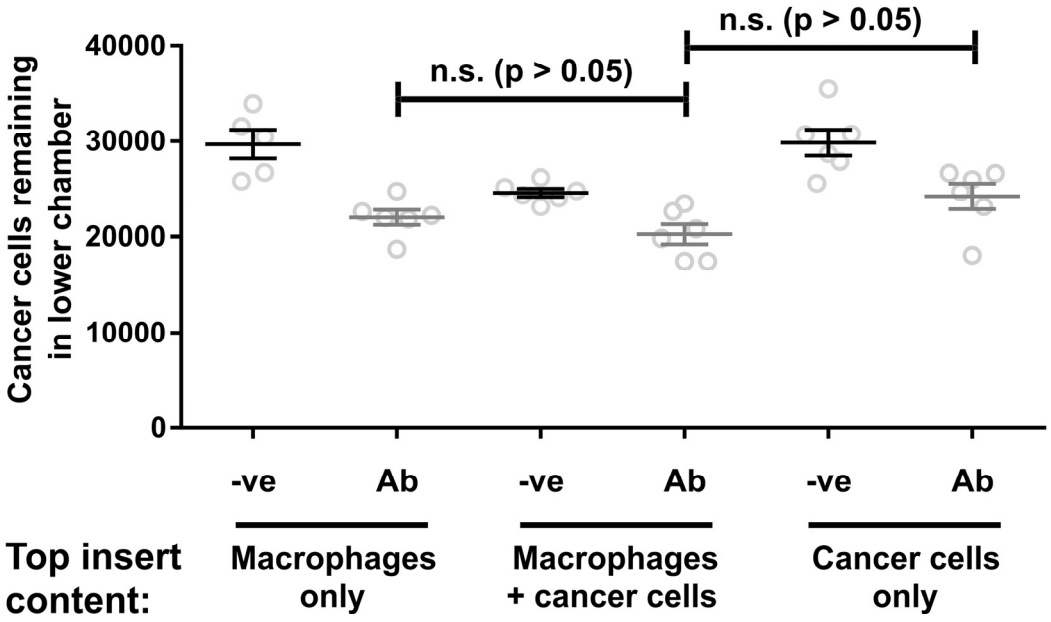

Figure 2-4: Macrophage-mediated killing of opsonized target cells is contact-dependent

Different combinations of 1×10^5 RAW264.7 cells, $2.5x10^4$ MDA-MB-453 cells and 1 μg/ml trastuzumab were mixed in the inserts of transwell plates (0.4 μm pores; Corning) and $1x10^5$ MDA-MB-453 cells were cultured in the lower chambers. Following incubation at 37°C for 72 hours, the cancer cells in the lower chambers were harvested and live cells quantitated by flow cytometry. Error bars represent standard errors. Statistically significant differences between samples were determined using Student's *t*-test. n.s., no significant difference ($p > 0.05$).

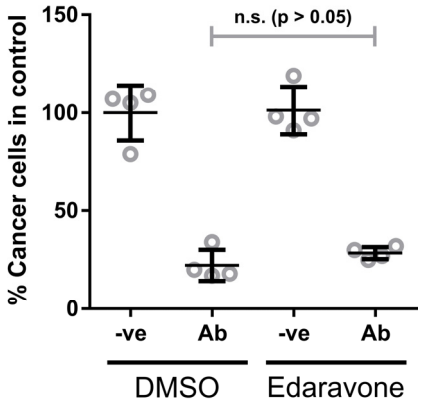

Figure 2-5: Macrophage-mediated killing of opsonized target cells occurs in the presence of the reactive oxygen species scavenger, edaravone

RAW264.7 macrophages were co-cultured with CFSE-labeled MDA-MB-453 cancer cells at 4:1 effector:target ratio (2.5×10^4:6×10^3 cells) and incubated at 37°C for 72 hours in the presence of 1 μg/ml trastuzumab (Ab) or PBS vehicle (-ve). Edaravone (1 μM) or vehicle (DMSO) were added to the cultures. Live cancer cell numbers were determined using flow cytometry and expressed as % cancer cell levels in control. Statistically significant differences between samples were determined using Student's *t*-test. n.s., no significant difference ($p > 0.05$).

The different levels of cell killing induced by incubation of trastuzumab-opsonized cancer cells with J774A.1 or RAW264.7 macrophages prompted us to use fluorescence microscopy to investigate the interactions between these effector:target cell combinations. Co-incubation of J774A.1 macrophages and MDA-MB-453 cells in the presence of trastuzumab led to the appearance of both phagocytosed cancer cells (whole cell phagocytosis, WCP) and cancer cell fragments, or trogosomes, within the CD45-positive macrophages (Figure 2-6A, Movie S1). Permeabilization of the cells before staining with anti-mouse CD45 antibody demonstrated that the phagosomes and trogosomes had associated CD45, indicating that they were encapsulated by the macrophage plasma membrane (Figure 2-6B). Similar observations were made using SK-BR-3 and HCC1954 cells as targets (Figure 2-7A). By marked contrast, although RAW264.7 cells were active in trogocytosis, phagocytic events involving complete cells were not observed when these macrophages and trastuzumab-opsonized breast cancer cells (MDA-MB-453, SK-BR-3 or HCC1954) were co-cultured (no WCP events were observed in 21 fields of view for RAW264.7 cells whereas 12/31 fields of view contained WCP events for J774A.1 macrophages; Figure 2-7B). Consistent with the earlier observations of others [20,33,115], the use of human monocyte-derived macrophages as effectors with trastuzumab-opsonized tumor cells resulted in both trogocytosis and phagocytosis, combined with a decrease in cancer cell numbers (Figure 2-8).

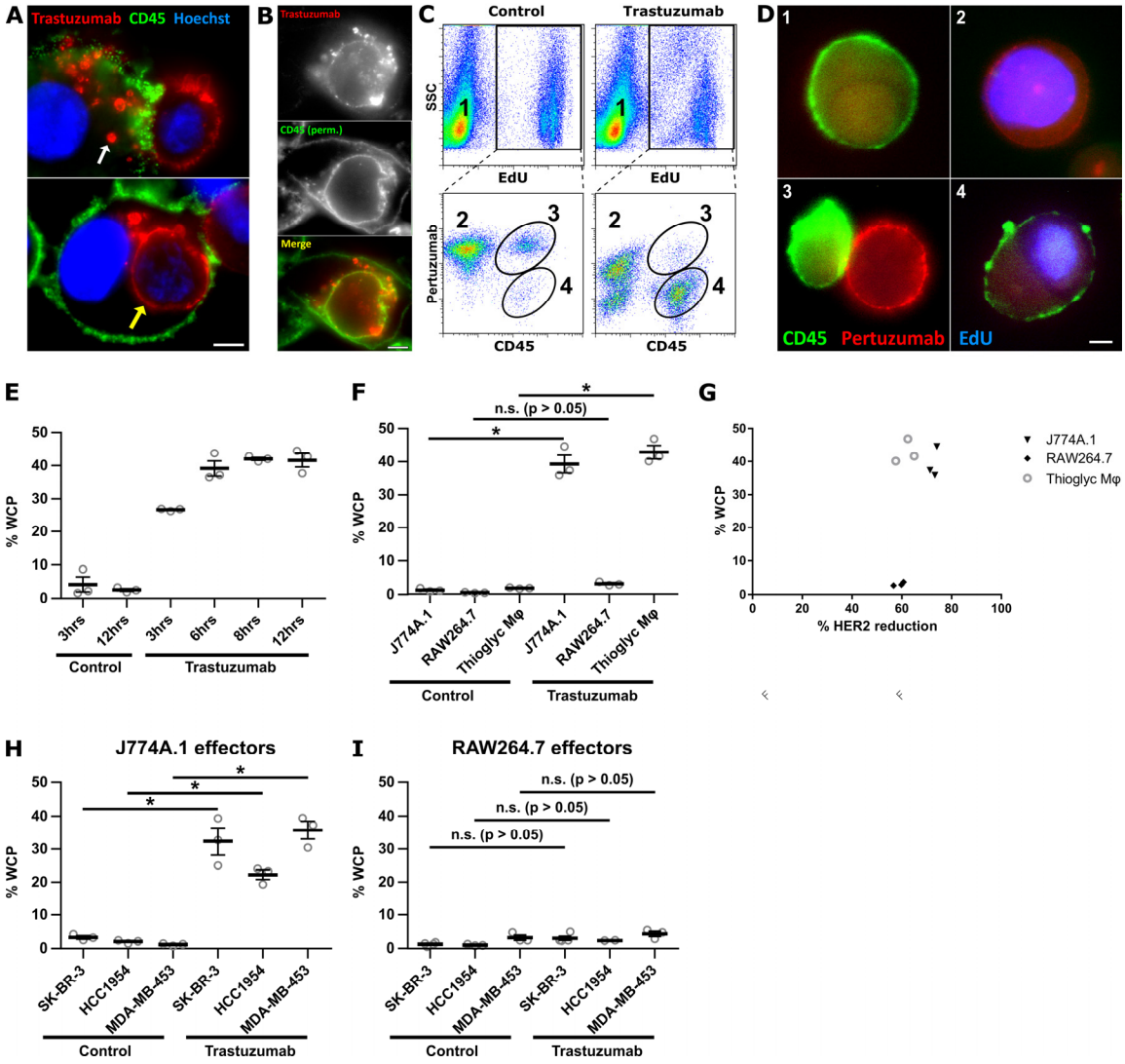

Figure 2-6: J774A.1 and RAW264.7 macrophages exhibit different phagocytic activities

A, MDA-MB-453 cells were harvested and opsonized by incubation with 10 µg/ml Alexa 555-labeled trastuzumab at room temperature for ten minutes followed by washing. The opsonized cancer cells (2.5×10^4 cells/imaging dish) were added to adhered, IFNγ-activated J774A.1 macrophages (4×10^4 cells) for 30 minutes and the samples fixed and stained. Trogosomes and a completely engulfed cancer cell are indicated by white and yellow arrows, respectively. B, J774A.1 macrophages, and MDA-MB-453 cells were incubated as in A, fixed, permeabilized and mouse CD45 detected using FITC-labeled mouse CD45-specific antibody. C, representative flow cytometry plots to show the identification of the whole cell phagocytosis (WCP) population. Macrophages were plated for 18 hours, followed by addition of EdU-treated cancer cells at a 10:1 effector:target cell ratio in the presence of 1 µg/ml trastuzumab or PBS vehicle for 6 hours. The samples were

then harvested and stained for mouse CD45 (macrophages), and cancer cells accessible to the medium were detected using labeled pertuzumab. The following cell populations can be identified: macrophage only (1); cancer cell only (2); macrophage:cancer cell conjugate (3); macrophage that has performed WCP (4). D, fluorescence microscopy images of cells representative of the populations numbered 1, 2, 3 and 4 in panel C. E, time-course of WCP using J774A.1 macrophages and MDA-MB-453 cancer cells. F, comparison of WCP activity using different macrophage cells with MDA-MB-453 cells after co-incubation for 6 hours. G, the plot of percentage WCP against percentage HER2 reduction for the data shown in Fig. 2F. The percentage of HER2 reduction from the cell surface was calculated from the ratio of the surface pertuzumab (MFI) remaining in the non-phagocytosed cancer cell population to surface pertuzumab (MFI) in samples without antibody treatment. H,I, comparison of WCP activity using J774A.1 (H) or RAW264.7 (I) macrophages with different breast cancer cell lines after co-incubation for 6 hours. Control in panels C, E-I, represent co-cultures incubated without trastuzumab. Error bars represent standard errors. Student's *t*-test was performed to indicate statistical significance (denoted by *; $p < 0.05$). n.s., no significant difference ($p>0.05$). For panels A, B and D, scale bars = 5 μm.

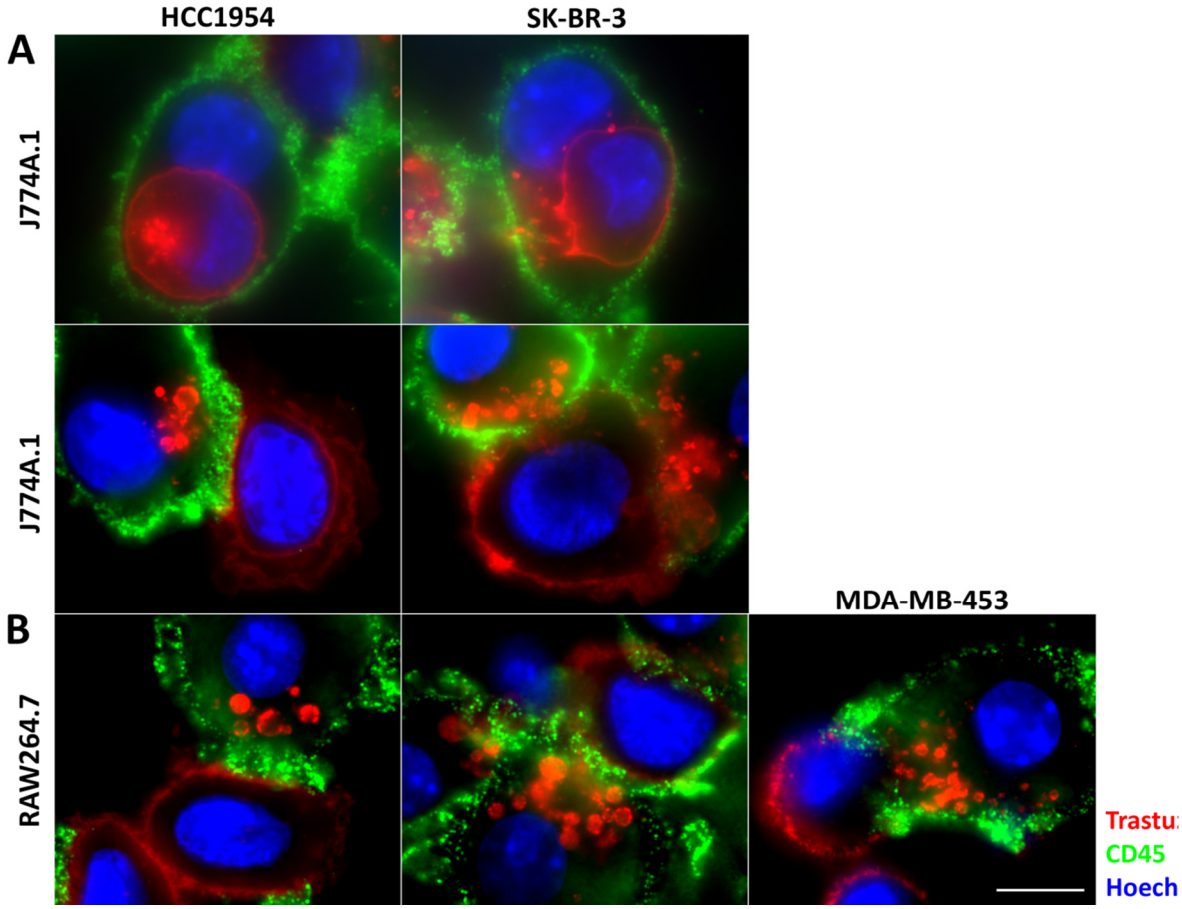

Figure 2-7: Representative images of conjugates formed between two macrophage cell lines and three cancer cell lines

SK-BR-3, HCC1954 or MDA-MB-453 cells were harvested and opsonized by incubation with 10 µg/ml Alexa 555-labeled trastuzumab at room temperature for ten minutes followed by washing. The opsonized cancer cells ($2.5x10^4$ cells/imaging dish) were added to adhered, IFNγ-activated J774A.1 macrophages for 30 minutes and the samples fixed and stained for CD45 using a mouse CD45-specific antibody (pseudocolored green). Nuclei were stained with Hoechst dye (pseudocolored blue). The upper row shows examples of WCP for J774A.1 macrophages, and the second and third rows show examples of trogocytosis for J774A.1 and RAW264.7 macrophages as indicated. Scale bar = 20 µm.

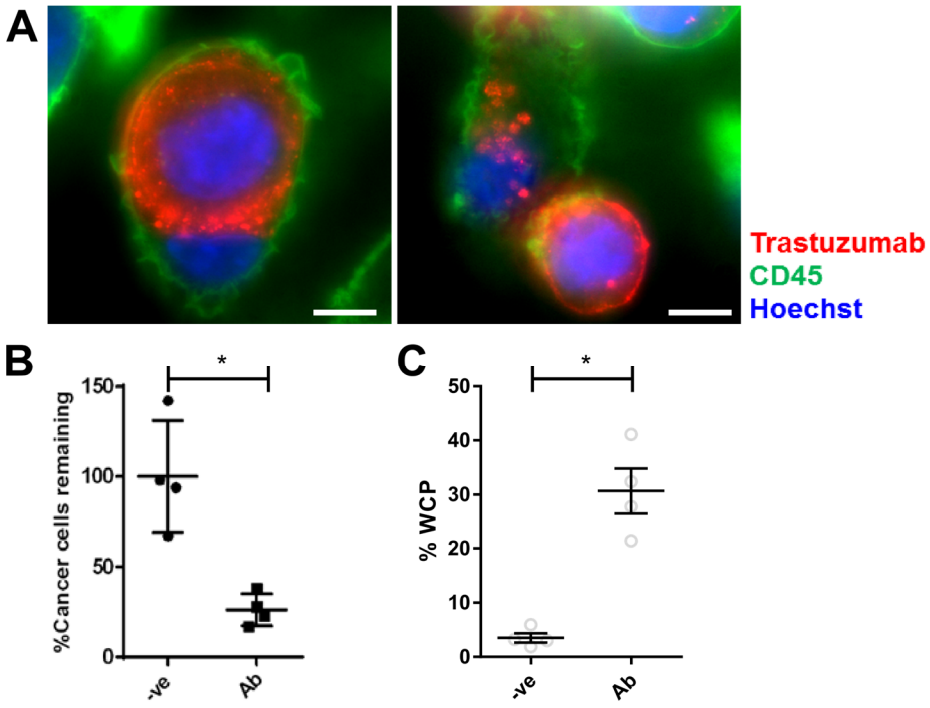

Figure 2-8: Human macrophages perform both phagocytosis and trogocytosis of antibody-opsonized target cells and reduce cancer cell numbers

A, 4×10^4 human monocyte-derived macrophages were cultured in MatTek dishes for six days and treated with 25 ng/ml IFN-γ for six hours, followed by the addition of 2.5×10^4 MDA-MB-453 cells opsonized with Alexa 555-labeled trastuzumab. The samples were incubated for 30 minutes, fixed and stained with a human CD45-specific antibody and Hoechst dye to detect macrophages and nuclei, respectively. Representative images show examples of WCP and trogocytosis performed by the human macrophages. B, CFSE-labeled MDA-MB-453 cells were added to monocyte-derived macrophages cultured in 48-well plates at a 4:1 effector:target cell ratio, with 1 µg/ml trastuzumab (Ab) or PBS vehicle (-ve) for 72 hours. The cells were harvested, and the remaining CFSE-positive live cancer cell fraction was quantitated by flow cytometry. C, EdU-labeled MDA-MB-453 cells were added to monocyte-derived macrophages cultured in 48-well plates at a 10:1 effector:target cell ratio with 1 µg/ml trastuzumab (Ab) or PBS vehicle (-ve) for 6 hours. The cells were harvested and stained for human CD45. Cancer cells accessible to the medium (i.e., not phagocytosed) were detected using fluorescently labeled pertuzumab, followed by fixation and staining for EdU. Stained samples were analyzed by flow cytometry. % WCP was calculated as the fraction of EdU-positive cells that were CD45-positive and pertuzumab-negative. Error bars represent standard errors. All experiments were performed using macrophages differentiated from monocytes isolated from fresh PBMCs, and similar results were obtained using purified monocytes from frozen stocks. Statistically significant differences between samples were determined using Student's *t*-test. * indicates a significant difference between samples ($p < 0.05$).

2.2.2 Trogocytosis leads to tumor cell death

To quantitate trogocytosis and WCP in a high-throughput manner, we developed a flow cytometric assay involving the labeling of the DNA of tumor cells with EdU (Figure 2-6C,D). To distinguish macrophage-associated tumor cells that were phagocytosed from those that formed macrophage:cancer cell couples, we reasoned that phagocytosed cells would be inaccessible to the anti-HER2 antibody, pertuzumab [116]. Importantly, we and others have demonstrated that pertuzumab does not compete with trastuzumab for binding and can, therefore, be used to detect HER2 in the presence of trastuzumab [98,117,118]. To quantitate cancer cells that had not been phagocytosed, co-cultures were harvested and stained with labeled pertuzumab, whereas EdU staining was used to identify all cancer cells. WCP activity was quantitated by determining the fraction of EdU-positive cells that were mouse CD45-positive and pertuzumab-negative, whereas cell couples were positive for all three markers. In the absence of trastuzumab, for J774.1 macrophages the number of cell couples was higher than in the presence of this antibody (Figure 2-6C), most likely because cell couples formed with antibody-opsonized cancer cells are expected to lead to efficient target cell phagocytosis. The CD45-negative, pertuzumab-low population represents cancer cells that have substantially reduced surface HER2 levels due to trogocytosis.

We first used the flow cytometric assay to characterize the dynamics of WCP in J774A.1:MDA-MB-453 co-cultures. Using an effector:target cell ratio of 10:1, approximately 25% of the target cells were phagocytosed within 3 hours. This number increased over time, reaching a plateau level of 40-50% following 8 hours (Figure 2-6E). WCP events are detectable even when the numbers of macrophages and cancer cells are equivalent or cancer cells

outnumber the macrophages (effector:target ratios of 1:1 or 1:5), although the fraction of cancer cells that undergo WCP decreases (Figure 2-9).

Thioglycollate-elicited primary peritoneal mouse macrophages and human monocyte-derived macrophages exhibited similar phagocytic activity to that observed for J774A.1 cells (Figure 2-6F, Figure 2-8). Concordant with the microscopy data, RAW264.7 cells rarely performed WCP (Figure 2-6F), whereas trogocytic activity was similar for all macrophage cell types (Figure 2-6G). Analogous results were obtained for phagocytosis using SK-BR-3, HCC1954 or MDA-MB-453 cells as targets, demonstrating that the low phagocytic activity of RAW264.7 macrophages is not target cell-dependent (Figure 2-6H,I). The percentage recovery of cancer cells for cell co-cultures with mouse and human macrophages were similar (70 – 80%; Figure 2-2), excluding the possibility that differential recovery contributes to the observed differences in phagocytic activity between macrophage:cancer cell combinations.

The relatively high level of tumor cell death in the presence of RAW264.7 cells (Figure 2-1B) combined with the very low levels of WCP activity indicated that trogocytosis can lead to tumor cell killing. To further investigate this, we performed long-term imaging of J774A.1:SK-BR-3 or RAW264.7:SK-BR-3 co-cultures (at a 4:1 effector:target ratio) in the presence of trastuzumab for approximately 3 days. In agreement with the fixed cell and flow cytometry data, multiple phagocytic events involving whole cells were observed for J774A.1 macrophages, whereas WCP rarely occurred for RAW264.7 macrophages. Individual cancer cells undergoing trogocytosis by both J774A.1 and RAW264.7 macrophages could be observed, and in multiple cases cancer cell death was observed following several days of

intermittent trogocytic attack (Movie S2 for J774A.1, Figure 2-10A and Movie S3 for RAW264.7 macrophages; data shown are representative of at least 14 events observed for each macrophage type). Similar trogocytic attack followed by cell death was observed when human macrophages were used as effectors (Movie S4).

Live cell fluorescence microscopy also demonstrated that the non-phagocytic interactions between macrophages and cancer cells involved the transfer of trastuzumab from cancer cells to macrophages via trogocytosis (Movie S5). CellEvent Caspase 3/7 Green Detection Reagent was not detectable in the opsonized target cells during the early stages of trogocytic attack (within 3 hours of co-culture set up; Movie S5), indicating that the macrophages accumulate trogosomes from live cells during this time frame. However, following 36 hours of co-culture incubation of opsonized tumor cells with J774A.1, RAW264.7 and human monocyte-derived macrophages, ~10% of target cells were positive for propidium iodide (PI) and fluorescently labeled annexin V (Figure 2-10B,C,D, Figure 2-11A,B). The annexin V-positive cells also accumulated CellEvent Caspase-3/7 Green Detection Reagent, indicating the induction of apoptosis (Figure 2-11A). The percentages of PI/annexin V-positive cells are lower than those for the cumulative cell death following 72 hours incubation (Figure 2-1) since PI/annexin V staining identifies a specific phase of the cell death pathway. Also, surface HER2 levels were reduced on all the opsonized cancer cells in the presence of macrophages Figure 2-10B,E,F). Combined with the survival of a proportion of cancer cells following 72 hours co-culture with macrophages (Figure 2-1), this indicates that not all trogocytosed cells undergo cell death within this time frame. Nevertheless, in combination with our live cell imaging experiments and the observation that soluble mediators do not contribute to macrophage (RAW264.7).

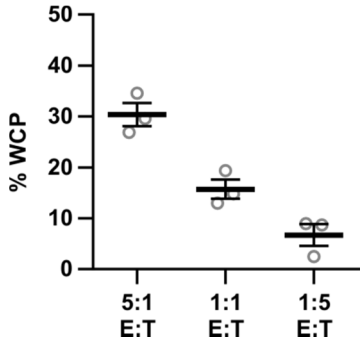

Figure 2-9: Effect of effector:target ratio on WCP activity

J774A.1 macrophages were plated for 18 hours, followed by addition of EdU-treated MDA-MB-453 cancer cells at different effector:target cell ratios in the presence of 1 µg/ml trastuzumab or PBS vehicle for 6 hours (3×10^5:6×10^4 cells for 5:1, 1.5×10^5:1.5×10^5 cells for 1:1 and 6×10^4:3×10^5 cells for 1:5 ratios, respectively). The samples were then harvested and stained for mouse CD45, and cancer cells accessible to the medium detected using labeled-pertuzumab, followed by fixation and staining for EdU. The samples were then analyzed by flow cytometry and % WCP was calculated as the fraction of EdU-positive cells that were CD45-positive and pertuzumab-negative. Error bars represent standard errors.

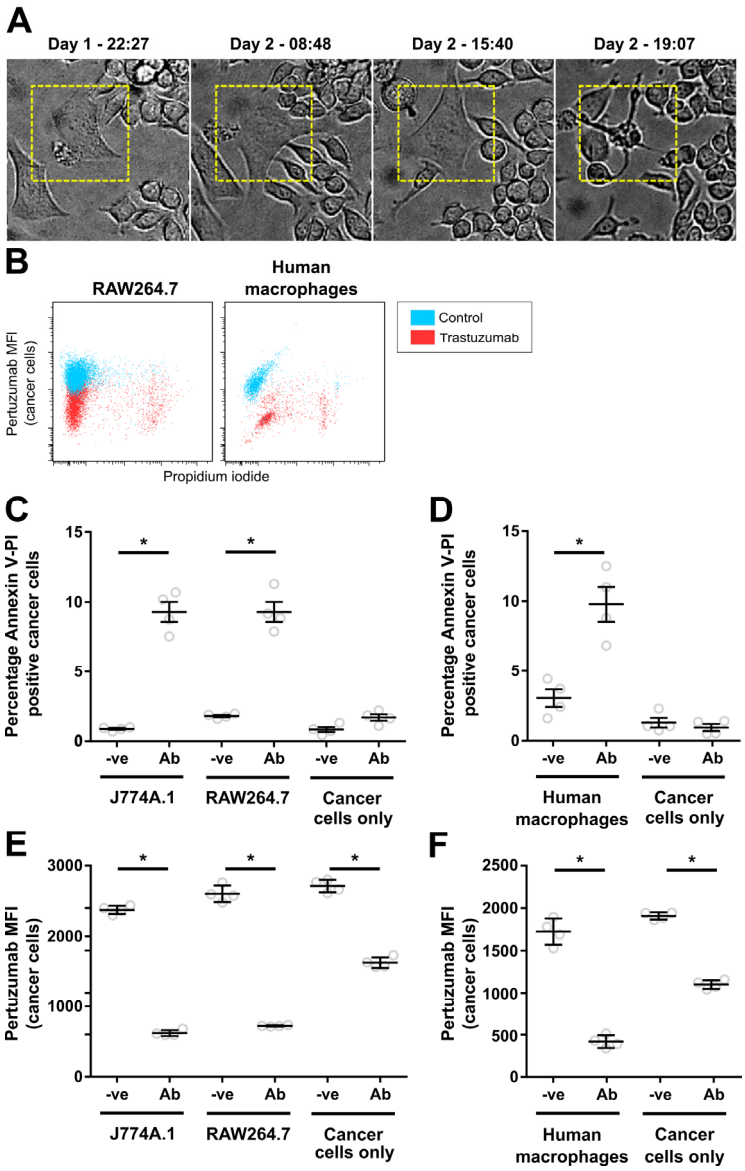

Figure 2-10: RAW264.7, J774A.1 and human monocyte-derived macrophages induce similar levels of apoptosis in opsonized cancer cells

Macrophages and cancer cells were plated at an effector:target cell ratio of 4:1 in a T25 culture flask (3×10^6:7.5×10^5 cells), 1 µg/ml trastuzumab was added 18-24 hours later and the cells were imaged. A, individual frames showing an SK-BR-3 cell undergoing cell death in a long-term light microscopy imaging experiment for a co-culture of SK-BR-3 and RAW264.7 cells in the presence of 1 µg/ml trastuzumab. Times of acquisition of each image are indicated. B,C,D, MDA-MB-453 cells were plated alone or co-incubated with RAW264.7, J774A.1 or human monocyte-derived macrophages at a 4:1 effector:target cell ratio in the presence of 1 µg/ml trastuzumab (Ab) or PBS vehicle (-ve) for 36 hours. B, representative dot-plots for pertuzumab fluorescence vs. PI fluoresence for cancer cells

from co-cultures of RAW264.7 or human macrophages with cancer cells in the presence (trastuzumab) and absence of antibody (control). C,D, fraction of annexin V, PI double-positive cancer cells in co-cultures determined by flow cytometry. E,F, samples shown in C and D, respectively, were stained with fluorescently labeled pertuzumab after harvesting and the mean fluorescent intensity (MFI) of pertuzumab on the cancer cell populations determined. Error bars represent standard errors. Student's *t*-test was performed to indicate statistical significance (denoted by *; $p < 0.05$).

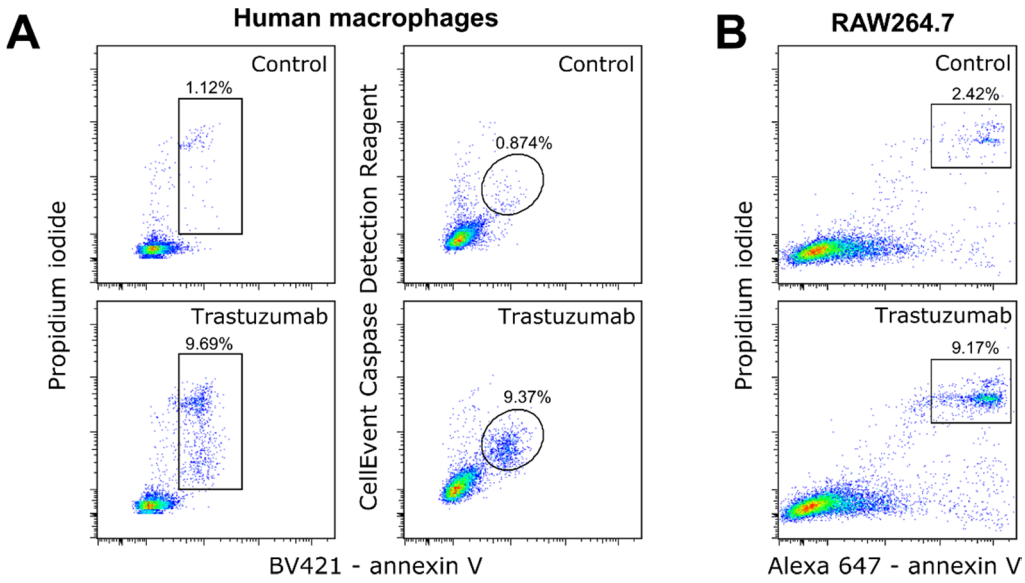

Figure 2-11: Macrophages induce apoptosis in opsonized cancer cells

MDA-MB-453 cells were co-incubated with human monocyte-derived macrophages or RAW264.7 macrophages at a 4:1 effector:target cell ratio in the presence of 1 µg/ml trastuzumab or PBS vehicle (control). Following 36 hours, cells were harvested and stained with fluorescently labeled annexin V and propidium iodide as indicated. CellEvent caspase-3/7 Green Detection Reagent was added to human macrophage:cancer cell co-cultures for the last 4 hours of culture prior to harvesting. Representative dot-plots for cancer cell populations following co-incubation with human macrophages (A) or RAW264.7 macrophages (B) are shown. Cell populations that are positive for cell death/apoptotic markers and their percentage (of total cancer cells) are indicated.

mediated death of opsonized targets, these data demonstrate that trogocytosis can lead to tumor cell attrition.

2.2.3 Trogocytosis involves tubular extensions of opsonized cancer cells

We employed live cell imaging to study the uptake of labeled trastuzumab from the cancer cell surface into the macrophage. Macrophages accumulate punctate, trastuzumab-positive trogocytic compartments, resulting in depletion of trastuzumab from the cancer cell surface in the region adjacent to the macrophage (Figure 2-12A). Following trastuzumab depletion, antibody levels in the region between the apposed cells recover within about 10 minutes, indicating that HER2/trastuzumab complexes are mobile on the cell surface. We next used MUM [79,81] combined with live cell imaging to analyze the dynamics of trogocytosis in three dimensions (Figure 2-12B,C). MUM enables the simultaneous visualization of cellular trafficking processes in multiple different focal planes [81,98]. Using MUM, we observed that trogocytosis involves the extension of tubular structures from the tumor cells into invaginations in the macrophage that are subsequently pinched off to form trogosomes within the effector cells (Figure 2-12B,C, Movie S6). Flow cytometry analyses indicated that although the levels of surface HER2 decrease on the target cells (Figure 2-12D), the CFSE fluorescence level does not change following two days of co-incubation with macrophages in the presence of trastuzumab (Figure 2-12E), indicating the engulfment of tubular extensions with high surface area:volume ratios. Also, following two hours of incubation of macrophages with tumor cells, many trastuzumab-positive trogosomes are located in lysosomes (Figure 2-13).

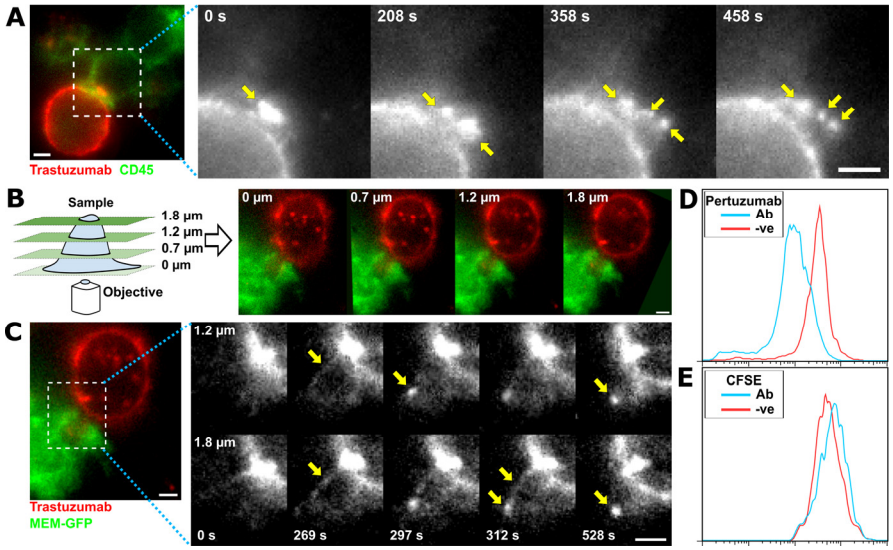

Figure 2-12: Fluorescence microscopy analyses using MUM reveals that trogocytosis involves tubular extensions of the cancer cells

A, individual frames from a live imaging experiment of MDA-MB-453: RAW264.7 cell conjugates. The cancer cells were opsonized by incubation with 10 µg/ml Alexa 555-labeled trastuzumab at room temperature for ten minutes followed by washing. These cells were added to IFN-γ-activated RAW264.7 macrophages expressing MEM-GFP (to label the plasma membrane; pseudocolored green) plated in dishes 30 minutes prior to imaging at a 1:1 effector:target cell ratio (2.5×10^4 cells). Grayscale images represent individual frames of the trastuzumab signal for the boxed region in the pseudo-colored image showing trastuzumab (red) and MEM-GFP (green) signals. Yellow arrows indicate punctate structures accumulating inside the macrophage. B, schematic diagram of the MUM configuration and representative images from multiple focal planes of a macrophage:cancer cell conjugate formed between IFN-γ-activated MEM-GFP expressing RAW264.7 macrophages and MDA-MB-453 cancer cells opsonized with Alexa 555-labeled trastuzumab as above. C, individual frames showing the trastuzumab signal (black and white panels) of live cell imaging from two focal planes displaying a trogocytic event involving tubulation. Yellow arrows indicate intermediates in the tubulation process. Numbers in the lower part of each panel represent the acquisition time (seconds) for each image pair. The left panel shows an overlay of the MEM-GFP (pseudocolored green) and trastuzumab (pseudocolored red) at 1020 sec in the 1.8 µm focal plane. The boxed region is expanded in the grayscale images. D, E, flow cytometry analyses of pertuzumab and CFSE staining levels in MDA-MB-453 cells co-incubated with RAW264.7 macrophages as described in Fig. 1B. Scale bars = 5 µm.

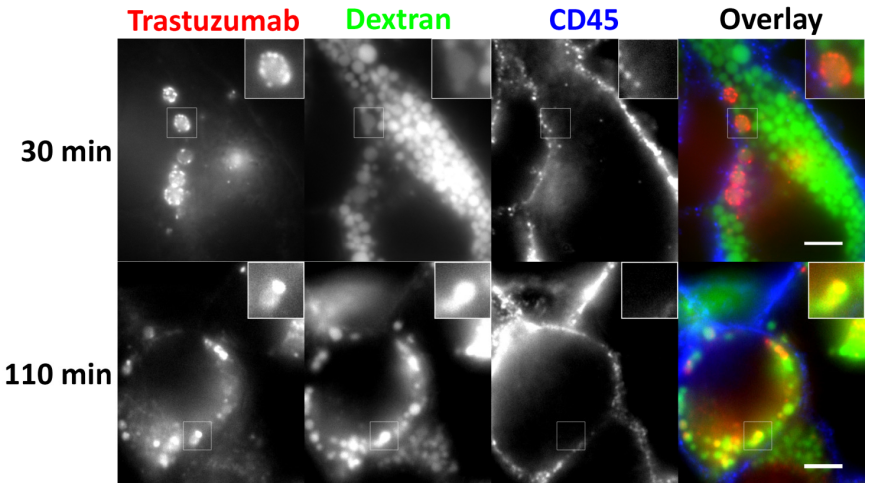

Figure 2-13: Trogosomes are rapidly targeted to lysosomes

MDA-MB-453 cells were harvested and opsonized by incubation with 10 µg/ml Alexa 555-labeled trastuzumab for ten minutes at room temperature followed by washing. J774A.1 macrophages (4×10^4 cells/dish) were incubated with the opsonized cancer cells (2.5×10^4 cells) for 30 minutes or 110 minutes, stained for mouse CD45 at room temperature (without fixation) followed by imaging. Before the addition of the cancer cells, lysosomes in J774A.1 macrophages were labeled by incubating cells with 100 µg/ml Alexa 488-labeled dextran for 1 hour followed by washing and incubating the cells in medium containing 25 ng/ml IFN-γ for 6 hours. Cells were imaged as live cells without fixation. Boxed regions are enlarged in the upper right-hand corners of each panel. Scale bars = 5 µm.

Although RAW264.7 cells rarely performed WCP, fluorescence microscopy indicated that the cell contacts with opsonized tumor cells were similar for both J774A.1 and RAW264.7 cells with respect to membrane ruffling and accumulation of actin and mouse CD45 (Figure 2-14). Also, both cell lines express all of the mouse FcγRs (Figure 2-15). Interestingly, we did not observe capping of HER2 at the interface between cancer cells and macrophages or in cancer cells incubated with antibody only (Figure 2-14, Figure 2-16A). By contrast, in the presence of the anti-CD20 antibody, rituximab, capping of CD20 occurred on the surface of B cells isolated from human peripheral blood mononuclear cells (PBMCs; Figure 2-16B), consistent with earlier observations [21,119]. Further, following 30 or 60 minutes incubation, rituximab was more rapidly depleted from B cells compared with the reduction of trastuzumab-associated with MDA-MB-453 breast cancer cells (Figure 2-16C).

2.2.4 FcγR affinity enhancement modulates the levels of trastuzumab-mediated trogocytosis

The engineering of antibodies to selectively enhance their affinity for binding to activating FcγRs over inhibitory FcγRs provides a pathway for improving antibody efficacy in vivo [33,34,39,106-108]. However, it is unknown whether this enhancement affects trogocytosis. We, therefore, analyzed the effects of two sets of mutations, G236A/I332E (AE) and G236A/S239D/I332E (ADE), on trogocytic activity. These mutations selectively increase the affinity of IgG1 for FcγRIIa or FcγRIIIa over the inhibitory receptor, FcγRIIb, resulting in higher 'Activatory/Inhibitory ratios' [33,120]. Also, the ADE mutations result in higher affinity interactions with FcγRs than the AE mutations [33]. Thioglycollate-elicited peritoneal macrophages isolated from transgenic mice that express human FcγRs, but not mouse FcγRs

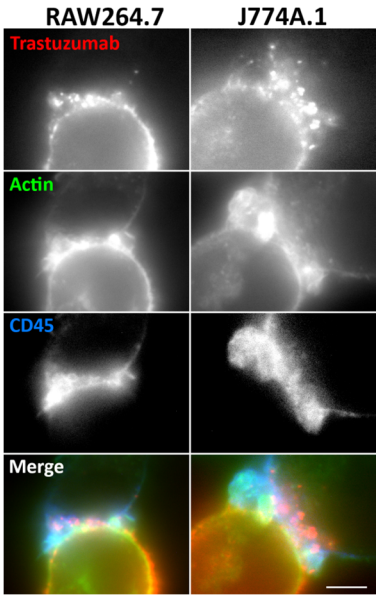

Figure 2-14: The macrophage:cancer cell synapse is similar for both RAW264.7 and J774A.1 macrophages

MDA-MB-453 cells were harvested and opsonized by incubation with 10 µg/ml Alexa 555-labeled trastuzumab for ten minutes at room temperature followed by washing. The opsonized cancer cells were then added to RAW264.7 or J774A.1 macrophages plated in a dish (2.5×10^4 cancer cells and 4×10^4 macrophages) and allowed to settle at room temperature for ten minutes. The dishes were subsequently transferred to 37°C for 2 minutes, fixed and stained for mouse CD45 and actin (using fluorescently labeled phalloidin). Scale bar = 5 µm.

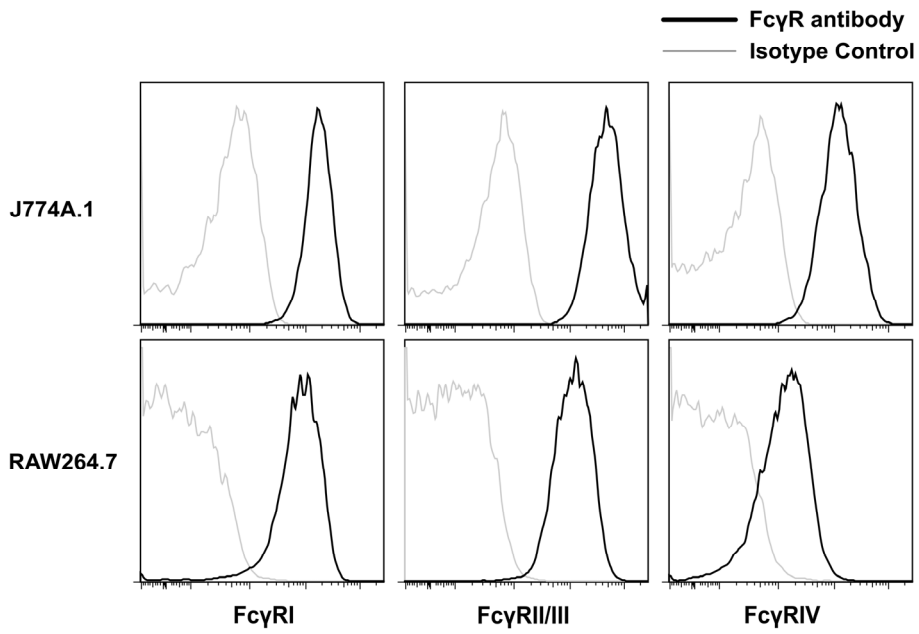

Figure 2-15: J774A.1 and RAW264.7 macrophages express all the mouse FcγRs

The FcγR expression profile of J774A.1 and RAW264.7 macrophages were analyzed by incubation with phycoerythrin-labeled antibodies (1 μg/ml) specific for mouse FcγRs for 1 hour at 37°C. Cells were then harvested and analyzed by flow cytometry. Isotype controls for the respective FcγR-specific antibodies are shown in each histogram plot.

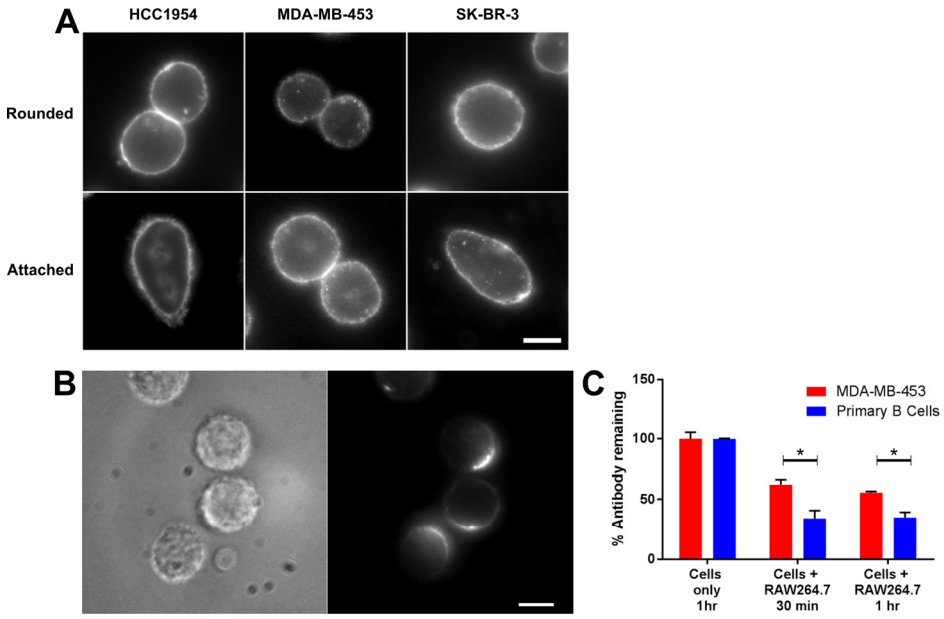

Figure 2-16: Breast cancer cell lines and B cells exhibit different capping behavior in response to antibody opsonization

A, HCC1954, MDA-MB-453 or SK-BR-3 cells were plated in glass-bottomed dishes overnight, followed by treatment with medium containing 10 µg/ml Alexa 555-labeled trastuzumab for 30 minutes at 37°C. Unbound trastuzumab was washed out and cells were fixed directly, or induced to round up by treatment with trypsin for 5 minutes at 37°C and then fixed, followed by microscopy analyses. B, primary B cells were opsonized with 10 µg/ml Alexa 555-labeled rituximab at room temperature for ten minutes, followed by washing and incubation at 37°C for 30 minutes. The cells were then transferred to MatTek dishes and analyzed as live cells by microscopy. C, primary B cells or MDA-MB-453 cells were opsonized with 10 µg/ml Alexa 555-labeled rituximab or 10 µg/ml Alexa 555-labeled trastuzumab, respectively. The cells were then added to RAW264.7 macrophages in a 48-well plate for 30 minutes or 1 hour at a 4:1 effector:target cell ratio, harvested and the fluorescent antibody levels associated with the cancer cell populations quantitated using flow cytometry. Scale bars = 10 µm. Statistically significant differences between samples were determined using Student's *t*-test. * indicates significant differences between samples ($p < 0.05$).

[121], were used for these experiments. Trogocytosis of cancer cells opsonized with wild-type trastuzumab or FcγR-enhanced variants of this antibody was analyzed using a flow cytometric assay that quantitates the amount of labeled pertuzumab-Fab fragment associated with macrophages. To distinguish cancer cell:macrophage conjugates from macrophages that had trogocytosed material derived from cancer cells, we used an antibody specific for the cancer cell marker EpCAM in the absence of cell permeabilization.

Although the AE mutant displayed higher trogocytic efficiency than the WT antibody, the ADE mutant did not lead to an enhancement of trogocytosis over WT trastuzumab (Figure 2-17A). Further, quantitation of WCP demonstrated that the addition of trastuzumab harboring AE or ADE mutations did not result in increased WCP activity following 3-6 hours' incubation (Figure 2-17B, Figure 2-18). These results prompted us to explore the effects of the mutations in the presence of high concentrations of endogenous IgG to mimic in vivo conditions. In the presence of 10 mg/ml IVIG, the addition of trastuzumab harboring AE and ADE mutations resulted in substantially increased trogocytic activity over the almost background levels observed with WT trastuzumab (Figure 2-17C). These low levels of trogocytic activity of WT antibodies in the presence of competing IgG are consistent with the observations of others [68]. Interestingly, the WCP activities were significantly decreased by the addition of IVIG for both WT trastuzumab and the mutated variants (Figure 2-17B,D). Similar inhibitory effects were observed when polyclonal, non-aggregated IgGs were purified from IVIG (Figure 2-19), indicating that aggregated IgG does not contribute to this activity of IVIG. To investigate the consequences of IVIG addition on tumor cell death, cancer cell

numbers were quantitated following 5 days co-incubation with WT trastuzumab or AE/ADE variants in the presence of

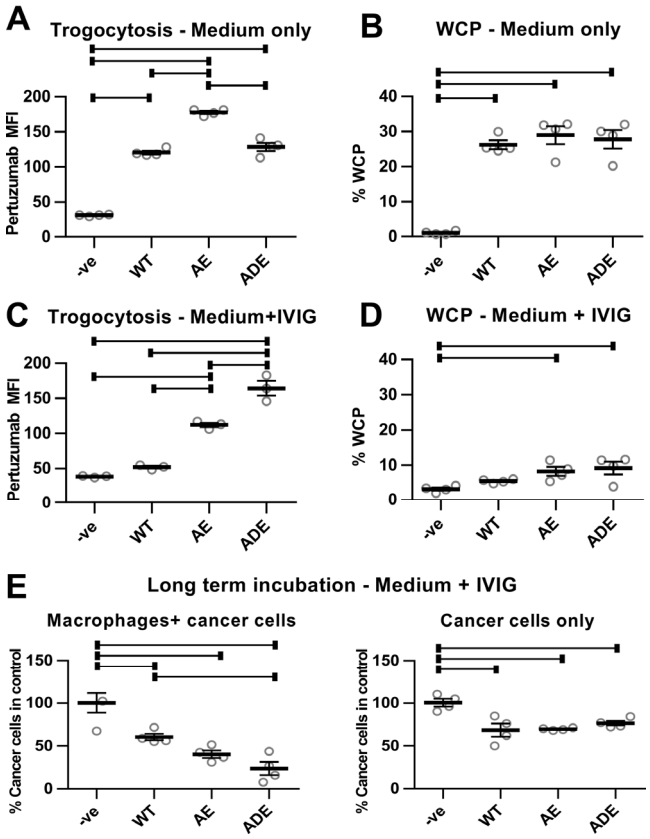

Figure 2-17: Antibodies with enhanced affinity for activating FcγRs have increased trogocytic and cell-killing activity

A, thioglycollate-elicited macrophages isolated from C57BL/6 mice transgenically expressing human FcγRs (hFcγR macrophages; 26) were plated with MDA-MB-453 cells at an effector:target ratio of 0.4:1 (4×10^4:1×10^5 cells). 18 hours later, 1 μg/ml wild type (WT) trastuzumab or engineered trastuzumab variants with enhanced affinity for FcγRIIa and FcγRIIIa (AE and ADE), combined with 0.5 μg/ml Alexa 488-labeled Fab fragments derived from pertuzumab, were added to the co-cultures for 60 minutes. As controls, cells were also co-cultured without trastuzumab (-ve). The mean fluorescence intensity (MFI) values for pertuzumab Fab staining in the macrophage population are shown. B, WCP assay was performed as before using hFcγR macrophages plated for 18 hours, followed by addition of 10-fold lower numbers of cancer cells and 10 μg/ml WT, AE or ADE trastuzumab variants for 6 hours. Trogocytosis (C) and WCP (D) assays were performed as in A,B, but in the presence of 10 mg/ml IVIG. Under the conditions of the trogocytosis assays (60 minutes incubation), phagocytosis of cancer cells was at background, control levels (data not shown). E, hFcγR macrophages were plated with cancer cells at an effector:target cell ratio of 2:1 (5×10^4:2.5×10^4 cells) or cancer cells alone for 24 hours, followed by addition of 10 mg/ml IVIG and 10 μg/ml WT, AE or ADE variants of trastuzumab. The medium was replaced by new medium containing the same additions after 3 days. Cells were harvested after 5 days and the remaining numbers of cancer cells

quantitated. Error bars represent standard errors. For A-E, one-way ANOVA analyses were carried out followed by a Tukey's multiple comparisons test between all sample pairs with a confidence interval of 95%. Horizontal lines indicate significant differences between sample pairs.

macrophages and 10 mg/ml IVIG (Figure 2-17E). The results demonstrate that the ADE variant is significantly more active than WT trastuzumab in reducing cancer cell numbers in the presence of macrophages, whereas the cytostatic effects of the antibodies alone on the cancer cells were similar for WT trastuzumab and the AE/ADE variants (Figure 2-17E). Comparison of the effects of WT trastuzumab and the ADE variant in the presence of human monocyte-derived macrophages and IVIG on target cell death also demonstrated increased tumoricidal activity of the FcγR-enhanced mutant (Figure 2-20). Consistent with the low level of trogocytic and phagocytic activity of WT trastuzumab in the presence of competing IVIG, our observations indicate that the cytostatic effect of trastuzumab is the major contributor to the target cell death induced by this antibody (Figure 2-17E, Figure 2-20). Collectively, these observations demonstrate that although the effector mechanisms of the macrophages have been significantly impaired by IVIG, their tumoricidal effects in the presence of trastuzumab can be increased by FcγR-enhancement.

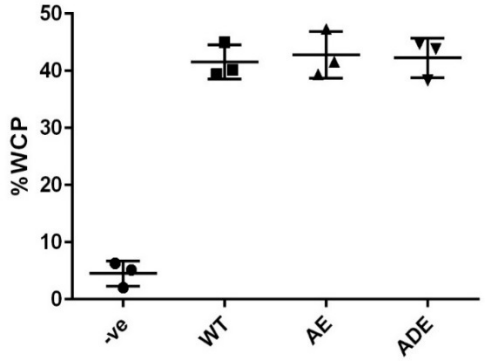

Figure 2-18: Engineered antibodies with enhanced FcγR binding affinities do not increase WCP activity during a 3-hour incubation

The WCP assay was performed as in Fig. 5B using thioglycollate-elicited macrophages from mice expressing human FcγRs and opsonized MDA-MB-453 cells as targets following a 3 hour incubation period. Samples were treated with PBS vehicle (-ve) or 10 μg/ml WT, AE or ADE variants of trastuzumab as indicated.

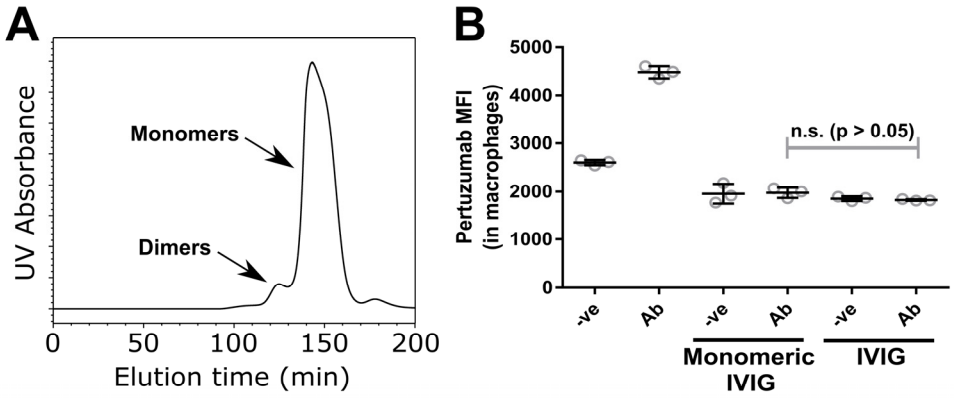

Figure 2-19: The inhibitory effect of IVIG on trogocytosis is not due to the effect of aggregated IgG or IgM

Size exclusion chromatography (HiLoad 16/600 Superdex 200 pg column) was used to separate the IgG monomers (150 kDa), IgG dimers, aggregates, and IgM in IVIG. A, elution profile of IVIG from the size exclusion column showing monomeric and dimeric IgG peaks. B, the effect of the monomeric IgG fraction on trogocytosis was compared with that of IVIG. Thioglycollate-elicited macrophages isolated from C57BL/6 mice transgenically expressing human FcγRs (4) were plated with MDA-MB-453 cells at an effector:target ratio of 0.4:1 (4×10^4:1×10^5cells). 18 hours later, 1 µg/ml wild type (WT) trastuzumab, together with 0.5 µg/ml Alexa 488-labeled Fab fragments derived from pertuzumab, were added to the co-cultures for 60 minutes with monomeric IVIG or unfractionated IVIG at a final concentration of 10 mg/ml. As controls, cells were co-cultured without trastuzumab (-ve). The mean fluorescence intensity (MFI) values for pertuzumab Fab staining in the macrophage population are shown. Statistically significant differences between samples were determined using Student's *t*-test. n.s., no significant difference ($p > 0.05$).

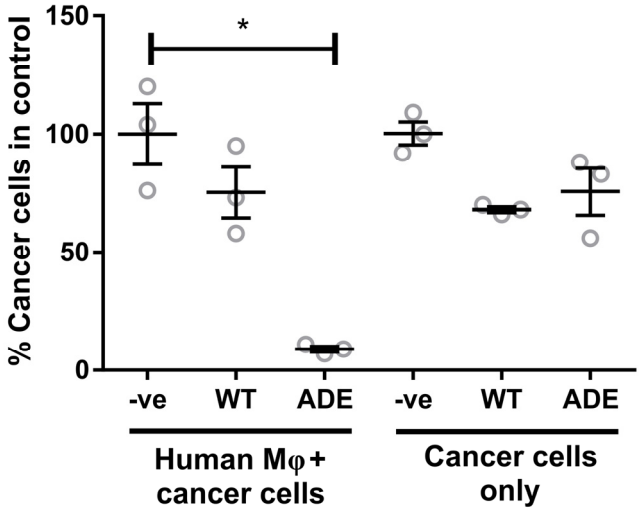

Figure 2-20: Human macrophage (Mφ) effectors can deplete cancer cells in the presence of IVIG and antibodies with enhanced binding affinities for FcγRs

2×10^5 purified human monocytes were plated in 48 well plates with M-CSF for six days, followed by the addition of 5×10^4 MDA-MB-453 cancer cells. 24 hours later, mixtures of 10 μg/ml WT or ADE variants of trastuzumab were added with 10 mg/ml IVIG. PBS vehicle (-ve) and cancer cells plated without macrophages were used as controls. The medium was replaced with fresh medium containing the same additions after 3 days. Cells were harvested after 5 days and the remaining numbers of cancer cells quantitated. Error bars represent standard errors. Statistically significant differences between samples were determined using Student's *t*-test. * indicates significant difference between samples ($p < 0.05$).

2.3 DISCUSSION

In the current study, we demonstrate that macrophage-mediated trogocytosis can lead to relatively efficient death of antibody-opsonized breast cancer cells, with around 50% reduction in target cell numbers over a period of three days. Consequently, cancer cells can sustain limited membrane damage, but they are not resistant to persistent trogocytosis over extended periods. A possibility that is not mutually exclusive is that the depletion of HER2 from the plasma membrane ablates growth factor-mediated signaling in HER2-addicted cells, resulting in cell death [104]. Interestingly, in earlier studies trogocytosis has been shown to efficiently remove target receptors such as CD20 from the plasma membrane, leading to amelioration of the tumoricidal effects of NK cells and macrophages in the presence of antibodies such as rituximab [70,105].Macrophages can have both tumor promoting or inhibitory effects [27,122] and our observations extend this dichotomous behavior to trogocytosis.

By contrast with the induction of clustering of lymphocyte receptors at the effector:target cell interface in the presence of opsonizing antibodies such as rituximab [21,119,123,124], we do not observe trastuzumab capping on cancer cells. In addition, during live cell imaging, following the trogocytic removal of fluorescently-labeled trastuzumab from the closely apposed target cell membrane, trastuzumab redistributes to the interface within around 10 minutes. This indicates that trastuzumab-HER2 complexes are mobile in the plasma membrane. The difference in receptor clustering suggests that the proportion of targeted receptor over other membrane constituents is lower in trogosomes derived from breast cancer cells. In addition, capping of receptors followed by their rapid removal from rituximab-opsonized lymphocytes is expected to not only reduce NK cell- and complement-mediated

target cell death, but also limit the duration of trogocytosis [68]. This is consistent with the observation that trogocytosis of rituximab-CD20 complexes on CD20-expressing EL4 cells does not lead to therapeutic effects in tumor-bearing mice (9) and can result in tumor escape during CD20-targeted therapy [125]. Consequently, the dynamic behavior of the opsonized antigen on the target cell surface is expected to modulate tumor cell killing by trogocytosis.

Recent studies in mouse models have demonstrated that Kupffer cells phagocytose antibody-opsonized circulating tumor cells (CTCs), leading to reductions in metastatic lesions [23]. By contrast, in the absence of tumor-specific antibody, trogocytosis rather than WCP of CTCs was observed which did not lead to tumor cell death. The apparent discrepancy between our study and these earlier analyses is most likely due to the limited contact time between CTCs and macrophages in the absence of antibody, although we cannot exclude a contribution of the difference in target [23]. In the current study, tumor cell death is observed when the target cells are adhered to the substratum and remain in contact with trogocytic macrophages for prolonged periods. This setting might more closely resemble macrophage-mediated attack on solid tumors rather than CTCs. Specifically, the physical constraints of surrounding cells in solid tumors are expected to favor trogocytosis over phagocytosis.

The contribution of trogocytosis to tumor cell death in the current study has been elucidated through our observation that WCP of several different cancer cells is very rarely observed when using RAW264.7 macrophages as effector cells. The behavior of RAW264.7 cells is consistent with the observations of others [104], and has been suggested to be due to the large size of the target cells. However, our observations that RAW264.7 cells rarely phagocytose

three different breast tumor cell lines, combined with the relatively efficient phagocytic engulfment of these cell lines by J774A.1 macrophages, indicates that there are intrinsic properties of RAW264.7 cells restricting their ability to perform WCP. This could relate to differences in cytoskeletal organization or differentiation state. In this context, actin and CD45 accumulation at the macrophage:cancer cell interface did not indicate differences between RAW264.7 and J774A.1 macrophages when analyzed by fluorescence microscopy. However, by contrast with our observations and those of others [104], it was recently reported that RAW264.7 cells phagocytose trastuzumab-opsonized BT-474 cells [126]. Further studies are required to determine the reasons for this apparent discrepancy.

Our microscopy studies of the spatiotemporal aspects of trogocytosis indicate that this process involves the engulfment of tubules extending from the target cell membrane rather than vesicular structures. These tubules are subsequently pinched off to form trogosomes within the macrophage. The involvement of tubular extensions, which can in multiple cases only be visualized using MUM due to their three-dimensional, highly dynamic nature, is consistent with the accumulation of high levels of plasma membrane relative to the cytosolic contents of the target cell. This tubulation also has implications for antigen presentation by trogocytic macrophages, since it would bias toward the delivery of plasma membrane-associated proteins over cytosolic proteins to the intracellular, degradative compartments that represent the sites of antigen loading onto MHC class II molecules [127].

Our studies also have direct relevance to the affinity enhancement of antibodies for FcγRs [33,34,39,106-108]. In the absence of competing IgG, we observe that the AE mutations, but

not the ADE mutations, confer increased trogocytic activity. Further, WCP was not affected by either of the mutation sets. In the absence of IVIG, it is possible that increased activity due to affinity/avidity enhancement is obscured through the WT antibody/FcγR interactions already being at maximal levels under the conditions of these assays. By contrast, in the presence of competing IVIG both AE and ADE mutations significantly increase macrophage-mediated trogocytosis, and to a lesser extent, phagocytosis. This translates to greater reductions in cancer cell viability for cells opsonized with trastuzumab-ADE compared with WT trastuzumab. In agreement with the observations of others [107], this reinforces the importance of performing such assays in the presence of endogenous antibody to ensure that the observations are physiologically relevant.

Several functions have been proposed for trogocytosis [64]. For example, it can lead to the acquisition of antigen in the form of peptide-MHC complexes by T cells followed by their fratricide [128]. Also, trogocytosis has been suggested to provide a conduit for cell-cell transfer of materials [75,129,130]. These studies and our current observations indicate that cells are tolerant to limited amounts of trogocytosis. This leads to the speculation that this process represents a tolerizing mechanism for self-antigens that is important for normal physiology. Consequently, the binding of autoreactive antibodies to cells may lead to trogocytic uptake by antigen presenting cells and immunological tolerance. Under these conditions, target cell death would be detrimental. By contrast, for tumor targeting with therapeutic antibodies, the relatively high antibody load could convert low level ‘background’ trogocytosis into an active tumoricidal effect.

Collectively, our studies have resulted in novel insight into the spatiotemporal dynamics and consequences of macrophage-mediated trogocytosis. Importantly, we demonstrate that this process involves the engulfment of tubular extensions and can lead to substantial attrition of tumor cells. Further, FcγR affinity enhancement results in significant increases in trogocytic activity. These observations extend the anti-tumor effects of macrophages to trogocytosis and have implications for the design of efficacious therapeutic antibodies.

2.4 MATERIALS AND METHODS

2.4.1 Cell lines and primary cells

The murine macrophage cell lines RAW264.7 (TIB-71) and J774A.1 (TIB-67), the human breast cancer cell lines MDA-MB-453 (HTB-131), SK-BR-3 (HTB-30) were purchased from the American Type Culture Collection (ATCC). The HCC1954 cell line was a gift from Drs. Adi Gazdar, John Minna and Kenneth Huffman, UT Southwestern Medical Center, Dallas. The cell lines were maintained in the following media supplemented with 10% fetal calf serum (FCS; Gemini Bio-products): macrophages, phenol red-free Dulbecco's Modified Eagle Medium (DMEM 11965-092); MDA-MB-453, RPMI-1640 (11875-093); SK-BR-3, McCoy's (16600082). HCC1954 cells were maintained in RPMI-1640 with 5% FCS. All experiments were conducted in medium containing FCS depleted of IgG [131], except experiments using Fc-engineered antibodies. Identities of all cancer cell lines were authenticated by short tandem repeat analysis on October 9, 2015 (University of Arizona Genetics Core). Murine macrophage cell lines purchased from the ATCC were maintained for less than 6 months in the laboratory. Purified human monocytes were purchased as frozen cells (Catalog no. 1008, Astarte Biologics) or purified from peripheral blood mononuclear cells (PBMCs, kindly provided by Darrell Pilling, Texas A&M University) using the EasySep Human Monocyte Enrichment Kit (Catalog no. 19059, Stemcell Technologies). The monocytes were cultured in DMEM containing 10% FBS supplemented with 50 ng/ml M-CSF (Catalog no. 300-25, Peprotech) in 48 well plates, MatTek dishes or T25 flasks for six days before use in assays. Purified primary human B cells were purchased as frozen cells (Astarte Biologics), thawed according to the manufacturer's protocols and used in experiments within 24 hours.

2.4.2 Antibodies

Clinical-grade trastuzumab, pertuzumab, rituximab and intravenous gammaglobulin (IVIG; Gamunex) were obtained from the UT Southwestern Pharmacy. Monovalent Fab fragments derived from pertuzumab were generated using a Pierce Fab Preparation Kit (Thermo Scientific). Trastuzumab, rituximab, pertuzumab and pertuzumab Fab fragments were labeled using Alexa 488 or 555 labeling kits (Life Technologies). The construction of trastuzumab heavy and light chain expression constructs was performed as described previously [114]. Mutations to enhance the binding of trastuzumab (human IgG1) to FcγRs, G236A/I332E (AE) and G236A/S239D/I332E (ADE) [33] were introduced into the trastuzumab expression construct by splicing by overlap extension [132]. Sequences of expression constructs are available upon request. Wild-type (WT) and mutated trastuzumab were expressed in transfected CHO cells using previously described methods [114]. Pharmacy grade trastuzumab was used in all assays except the comparison of WT trastuzumab and AE/ADE variants. Antibodies specific for mouse FcγRs (clone X54-5/7.1 for FcγRI, 93 for FcγRII/III and 9E9 for FcγRIV) and the corresponding isotype controls were purchased from Biolegend.

2.4.3 Isolation of thioglycollate-elicited macrophages

C57BL/6J mice (purchased from The Jackson Laboratory) or human FcγR-transgenic C57BL/6J mice (gift from Dr. Jeffrey Ravetch, The Rockefeller University) [121] were housed in a pathogen-free animal facility at UT Southwestern Medical Center or the Texas A&M Health Science Center and handled according to protocols approved by the Institutional Animal Care and Use Committees. 8-12 week old male mice were intraperitoneally injected with 3 ml aged thioglycollate (gift from Dr. Chandrashekar Pasare, UT Southwestern Medical

Center). After 72 hours, the mice were sacrificed and peritoneal macrophages isolated by peritoneal lavage. The macrophages were plated in the assay plates in complete DMEM containing 10% FCS, and assays were performed 1-3 days later using the same conditions as for the macrophage cell lines.

2.4.4 Analyses of macrophage effects on tumor cell numbers

Target cells were harvested, labeled with carboxyfluorescein succinimidyl ester (CFSE; Life Technologies) and mixed with effector cells at the indicated effector:target ratios in wells of 48-well plates, centrifuged to obtain an even distribution in the wells and allowed to attach overnight. Cells were treated with 1 μg/ml trastuzumab and incubated at 37°C for 72 hours. The cells were harvested by trypsinization, incubated with PerCP-labeled anti-mouse CD45 antibody (clone 30-F11, BD Biosciences) and Alexa 488-labeled pertuzumab, washed and fixed with formalin. For human macrophage effectors, anti-human CD45 antibody (HI30, Biolegend) was used to identify macrophages. A constant number of Flow Check 6 μm high-intensity yellow-green beads (PolySciences, Inc.) were added to each tube and the samples analyzed by flow cytometry (BD FACSCalibur or LSR Fortessa). The number of cancer cells in each sample was calculated by counting the CFSE-positive events, followed by normalization with the bead counts.

For the analysis of staining of tumor cells by annexin V and propidium iodide (PI), co-cultures were incubated as above for 36 hours. Harvested cells were stained with Alexa 647-labeled annexin V and PI (Life Technologies) or BV421-labeled annexin V (BD Biosciences), followed by quantitation of the fraction of annexin V-positive, PI-positive, CD45-negative

cells using flow cytometry. For the analysis of caspase activity in the tumor cells, the co-cultures were treated with 2 μM CellEvent Caspase-3/7 Green Detection Reagent (Life Technologies) for the last four hours of incubation.

2.4.5 Whole cell phagocytosis assay

Effector cells were plated in 24 well plates, centrifuged to ensure an even distribution and incubated for 18 hours. Six hours prior to addition of target cells and opsonizing antibody, cells were treated with 25 ng/ml IFN-γ. Target cells were incubated with 5 μM 5-ethynyl-2'-deoxyuridine (EdU) provided with the Click iT EdU Flow Cytometry Kit (Life Technologies) for 48 hours prior to the assay, harvested by trypsinization, added at the appropriate effector:target ratios and incubated at 37°C for 3-6 hours in the presence of 1 μg/ml trastuzumab. The cells were harvested, treated with 10 μg/ml human IgG1 to block non-specific binding and incubated with 3 μg/ml PerCP-labeled anti-mouse CD45 antibody and 10 μg/ml Alexa 488-labeled pertuzumab for ten minutes on ice. The cells were subsequently washed, resuspended in 50% formalin in PBS and stained for EdU using the EdU flow cytometry kit protocol. Samples were analyzed using flow cytometry (BD FACSCalibur or LSR Fortessa). Percentage whole cell phagocytosis (WCP) was calculated as the fraction of EdU+ cells that were also CD45-positive and pertuzumab-negative.

2.4.6 Statistics

Tests for statistical significance between groups were carried out using Student's t-test or one-way ANOVA with Tukey's multiple comparisons test in GraphPad Prism (GraphPad Software). p-values of less than 0.05 were considered significant.

2.4.7 Sample preparation for fixed cell microscopy

Cells were plated in glass-bottomed dishes (MatTek Corporation) overnight and treated as indicated in the figure legends. Fixation was carried out using 3.4% paraformaldehyde (Electron Microscopy Sciences) for 10 minutes at 37°C. When necessary, samples were permeabilized with 0.5 mg/ml saponin (Sigma Aldrich). Mouse CD45 was detected by incubating the sample with biotinylated anti-CD45 antibody (BD Biosciences), followed by detection with streptavidin-conjugated quantum dot (QD) 655 (Life Technologies). FITC-labeled anti-mouse CD45 antibody (BD Biosciences) was used in Fig. 2B for CD45 detection in permeabilized cells. Treatment of cells with DiD (Vybrant DiD Cell-Labeling Solution; Life Technologies), Alexa 647-labeled phalloidin (Life Technologies) and Hoechst 33528 (AnaSpec, Inc.) was carried out using protocols recommended by the manufacturer. Macrophages were treated with 25 ng/ml recombinant mouse interferon-γ (IFN-γ; BD Biosciences) for 6 hours prior to use in fixed cell microscopy experiments.

2.4.8 Sample preparation for live cell microscopy

For imaging WCP events, J774A.1 macrophages were plated overnight and activated with 25 ng/ml IFN-γ six hours prior to addition of target cells. Macrophages were labeled with biotinylated anti-mouse CD45 antibody followed by streptavidin-coated QD655 as described above and Alexa 555-labeled, trastuzumab-opsonized MDA-MB-453 cells added. The cells were imaged using single plane microscopy.

For the long-term imaging of macrophage-cancer cell interactions, macrophages and cancer cells were plated at appropriate ratios in non-vented T25 flasks. The cells were labeled

following 24 hours with Alexa 555-labeled trastuzumab and FITC-labeled anti-mouse CD45 antibody. Alexa 488-labeled anti-human CD45 antibody was used when human macrophages were imaged. A pre-marked region of the flask was imaged using the Axiovert 200M fluorescent microscope and a Zeiss 20X Plan Apochromat objective to identify the cancer cells and macrophages. The flask was then gassed by injecting a sterile 95% air /5% CO2 mixture and subsequently sealed. The same pre-marked region was then imaged at 37°C in the long-term imaging setup.

2.4.9 Sample preparation for trogocytosis live imaging

For live cell imaging of trogocytosis using single plane microscopy or MUM, MDA-MB-453 cells were plated in MatTek dishes and labeled with 10 μg/ml Alexa 555-labeled trastuzumab for ten minutes at room temperature. Six hours prior to the experiment, MEM-GFP expressing RAW264.7 macrophages or J774A.1 macrophages labeled with FITC-labeled anti-mouse CD45 antibody were treated with 25 ng/ml IFN-γ. 30 minutes prior to imaging, opsonized cancer cells were added to the macrophages at a 1:1 effector:target cell ratio. CellEvent Caspase-3/7 Green Detection Reagent (Life Technologies) was added to the medium at a concentration of 2 μM throughout assays in which target cell viability was assessed for up to three hours. RAW264.7 macrophages were transfected with MEM-GFP (Clonetech) using the Amaxa Nucleofection device and Cell Line Nucleofecter Kit V (Lonza).

2.4.10 Microscopy imaging configurations

For fixed cell microscopy, images were acquired using a Zeiss Axiovert 200M inverted fluorescence microscope with a Zeiss 63×/1.4NA Plan Apochromat objective as described

previously [133]. Single plane imaging of trogocytosis in live cells was performed with the Deltavision epifluorescence microscope (Applied Precision) at the UT Southwestern Live Cell Imaging Core Facility.

To image phagocytic events in live cells, the same configuration as above was used but with a Zeiss 40x/1.4NA Plan Apochromat objective and a triband emission filter. The fluorescence signal from excitation at 543 nm was split between two cameras using a 630 DCLP filter, with both cameras positioned at the design focal plane. Images were acquired in two colors simultaneously at 0.9 Hz, registered and processed using MIATool.

The long-term imaging experiments using transmitted light were performed using phase contrast on an Olympus IX70 microscope through an LCPlanFl 20x/0.40 objective. The images were acquired every 30 seconds through an 8.0 Mega Pixel Autofocus Camera module (See3CAM_80, e-con Systems, Inc) that was attached to the eyepiece of the microscope. The configuration was housed in a 37°C warm room to maintain the temperature. The images were processed with MIATool software.

The MUM configuration used to image trogocytosis was based on a Zeiss Axio Observer.A1 body and a Zeiss 100x/1.4NA Plan Apochromat objective. The sample was illuminated with a 488 nm solid state laser (Coherent) for GFP excitation and a 543 nm diode laser (Opto Engine LLC) for Alexa 555 excitation. The illumination was directed to the sample and fluorescence filtered back using a polychroic beamsplitter/emission filter combination (488/543/633 RPC and 488/543 M; Chroma Technology Corporation). The emission was split equally between four Andor iXon EM-CCD cameras (Andor Technology Ltd.) using 50:50 beamsplitters

(Chroma Technology Corporation). The focal plane imaged by each camera was calibrated and light splitting performed as described previously [98]. The cameras were run on conventional gain mode and images were acquired in two colors at a frame rate of 0.67 Hz. Camera acquisition and shuttering of excitation lasers were controlled using custom acquisition software written in LabWindows/CVI (National Instruments Corporation). The acquired images were registered and processed using the Microscopy Image Analysis Tool (MIATool, http://wardoberlab.com/software/miatool) [134] written in MATLAB (MathWorks, Inc).

CHAPTER THREE
STUDYING THE FATE OF WHOLE CELL PHAGOSOMES
3.1 INTRODUCTION

The process by which eukaryotic cells engulf and degrade particulate matter is known as phagocytosis [48]. Specialized phagocytes such as macrophages are known to be particularly active in this process. Fusion of endolysosomal compartments with the maturing phagosome as it acidifies results in delivery of degradative enzymes followed by the destruction of the phagosomal contents [45]. Phagocytosed targets, such as mammalian cells, that approach the size of the phagocyte comprise a large proportion of the cellular content of a phagocyte, and as such, present unique challenges for degradation due to their relatively large size. By contrast with beads, which are typically used as models for the study of phagocytic processes, phagocytosed cells contain degradable content. Consequently, the release of metabolites such as amino acids during the degradation process could induce osmotic stress within the phagosome, causing it to increase in volume [135]. Hence, effector cells may employ specific mechanisms during the degradative processing of cells within phagosomes in order to limit cellular stress.

The mechanistic target of rapamycin (mTOR) is a component of the mTOR complex 1 that localizes to lysosomes and acts as a sensor of nutrient availability and growth factor signaling [136,137]. Specifically, this pathway is responsive to the accumulation of amino acids in the lysosomal lumen [138]. This suggests that the degradation of cells within phagosomes may be coordinated by the mTOR pathway, particularly in cases where the degradation process leads to amino acid release [139]. By contrast, the phagocytosis of

beads or other targets such as red blood cells for which the generation of amino acids does not occur or is relatively limited would not be expected to affect mTOR signaling.

The study of cellular phagosomes is directly relevant to ADCP of targets such as tumor cells. Antibodies represent a rapidly expanding class of therapeutics for the treatment of cancer [66]. The recognition of tumor-specific antigens by therapeutic antibodies results in coating, or opsonization, of the cancer cells which can lead to ADCP [25,140]. The presence of macrophages as the most abundant immune cell type in the majority of tumors [141], suggests that macrophage-mediated ADCP may contribute to the anti-tumor effects of antibodies. Although macrophages can have pro-tumorigenic consequences, results from multiple studies are consistent with a contribution of macrophage-mediated effector activity to tumor cell death [20,23,24,27,103,126,142]. Further, antigen can be processed from these phagosomes and presented in the context of major histocompatibility complex class I or II molecules to cognate T cells [111,143]. Hence, studying the maturation pathway of cellular phagosomes is expected to be of direct relevance to the successful use of therapeutic antibodies and induction of anti-tumor immunity.

In the current study, we have analyzed the fate of phagosomes containing antibody-opsonized cancer cells within macrophages. Interestingly, we observe the formation of a distinct phagosome-associated vacuole during phagosome maturation. This phagosome-associated vacuole is separated from the phagosome by a barrier that selectively restricts diffusion of solutes between the two compartments based on their size. Further, vacuoles are not detected with phagocytosed beads, indicating that amino acid levels regulate their

formation. Consistent with the involvement of amino acid release, vacuole formation was found to be under the control of the mTOR pathway. Collectively, our results suggest that this vacuole is a common feature associated with the degradation of cellular targets by phagocytes.

3.2 RESULTS

3.2.1 Identification of a phagosome-associated vacuole

Initially, we used live cell microscopy to analyze the phagocytic process involving J774A.1 macrophages as effectors and MDA-MB-453 breast cancer cells as targets. MDA-MB-453 cells were opsonized with Alexa 555-labeled HER2-specific antibody (trastuzumab) and co-incubated with macrophages that had been preloaded with Alexa 647-labeled dextran to identify lysosomes. At approximately three hours following phagocytosis, we observed the formation of a vacuole-like structure with a clear phase-contrast profile adjacent to the phagosome (Figure 3-1A, Movie S7). Time-lapse images showed the gradual increase in the size of this vacuole over 2-6 hours (Figure 3-1A). We observed that the vacuole and phagosome were positive for both Alexa 555 and Alexa 647 fluorophores (Figure 3-1B, Movie S7), indicating that the vacuole contains both lysosomal components and opsonizing antibody (fragments) derived from the macrophages and cancer cells, respectively. Interestingly, by contrast with phagocytosed cancer cells, vacuoles were not detected in macrophages that had phagocytosed antibody-opsonized latex beads (10 μm diameter; n = 128 phagocytosed beads; Figure 3-1C).

3.2.2 The contents of the phagosome and the vacuole are redistributed into lysosomes

We next investigated the time-course of the formation of the vacuole. Antibody-opsonized target cells were mixed with macrophages, and intravenous immunoglobulin (IVIG) was added to the conjugates following 1 hour to prevent further phagocytosis (by competitive inhibition of Fcγ receptor binding [142]). The numbers of phagosomes containing an

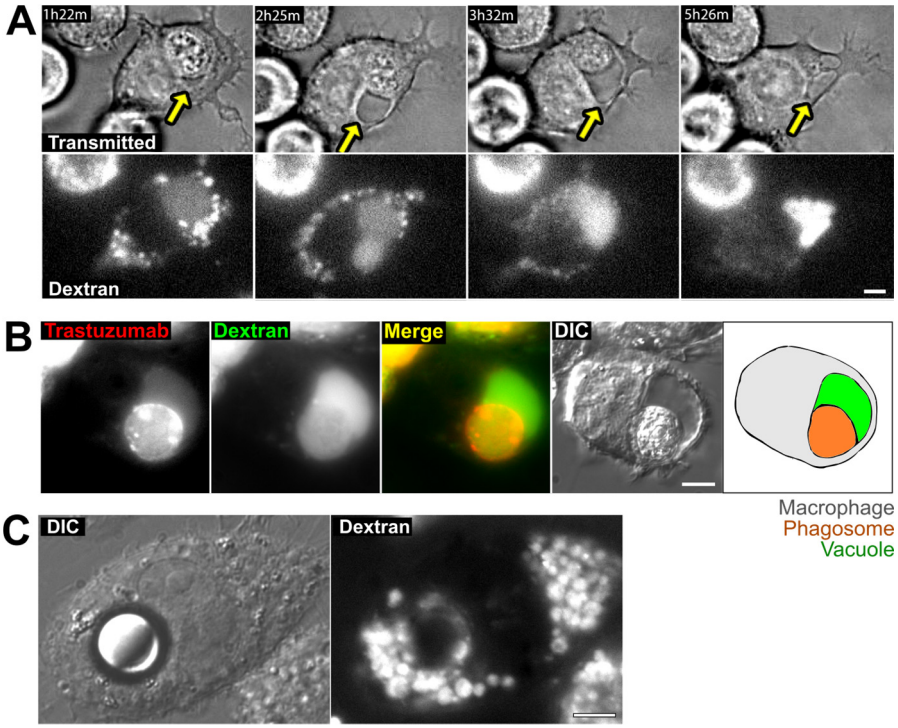

Figure 3-1 Phagosomes containing cancer cells have associated vacuoles

A, MDA-MB-453 cancer cells were opsonized with Alexa 555-labeled trastuzumab and co-incubated with J774A.1 macrophages for 1 hour. The macrophages were preloaded with Alexa 647-labeled 10 kDa dextran. A macrophage containing a phagocytosed target cell was identified and imaged live for 12 hours. The images show transmitted light and dextran fluorescence for this macrophage at the four indicated time points. Yellow arrows indicate the position of the vacuole adjacent to the phagosome. B, Image of a phagosome from a sample prepared as in A following a 4.5-hour incubation. Alexa 555 (trastuzumab) is pseudocolored red, and Alexa 647 (dextran) is shown pseudocolored green. The right-hand panel shows a schematic diagram of the approximate location of the phagosome-associated vacuole (green), the phagosome containing the corpse of the target cell (orange) and the boundary of the macrophage (gray). C, Streptavidin-coated beads (10 µm diameter) were opsonized with biotinylated trastuzumab, washed and added to J774A.1 macrophages. The macrophages were preloaded with Alexa 647-labeled 10 kDa dextran. The cells were subsequently incubated for 6 hours and imaged. Scale bars = 5 µm.

associated vacuole following a 2, 4, 6 or 8-hour incubation period were quantitated by microscopy. This quantitation showed that the percentage of phagocytosed cells with associated vacuoles is maximal at ~75% at 7 hours following phagocytosis, and this percentage decreases to ~50% at 9 hours (Figure 3-2A).

To further characterize the fate of the vacuole, similarly prepared samples were incubated for 6 hours and phagosome-associated vacuoles in these samples were analyzed by long-term live cell imaging. In this experiment, the lysosomes of the target cells were labeled instead of trastuzumab, to distinguish phagocytosis from trogocytosis (‘nibbling,' in which membrane fragments but not lysosomes of the target cell, accumulate in macrophages) [69,104,142]. Time-lapse images from long-term imaging reveal that as the phagosome-associated vacuoles begin to decrease in size around 8 hours, the dextran originating from the target cell, which was initially present in both the phagosome and the vacuole, redistributes throughout the lysosomal network of the macrophage during the following 14 hours (Figure 3-2B, Movie S8). This indicates that the phagosome-associated vacuole is a temporary structure formed during the maturation of large-cell phagosomes and that the contents of the vacuole are subsequently redistributed into the lysosomal network.

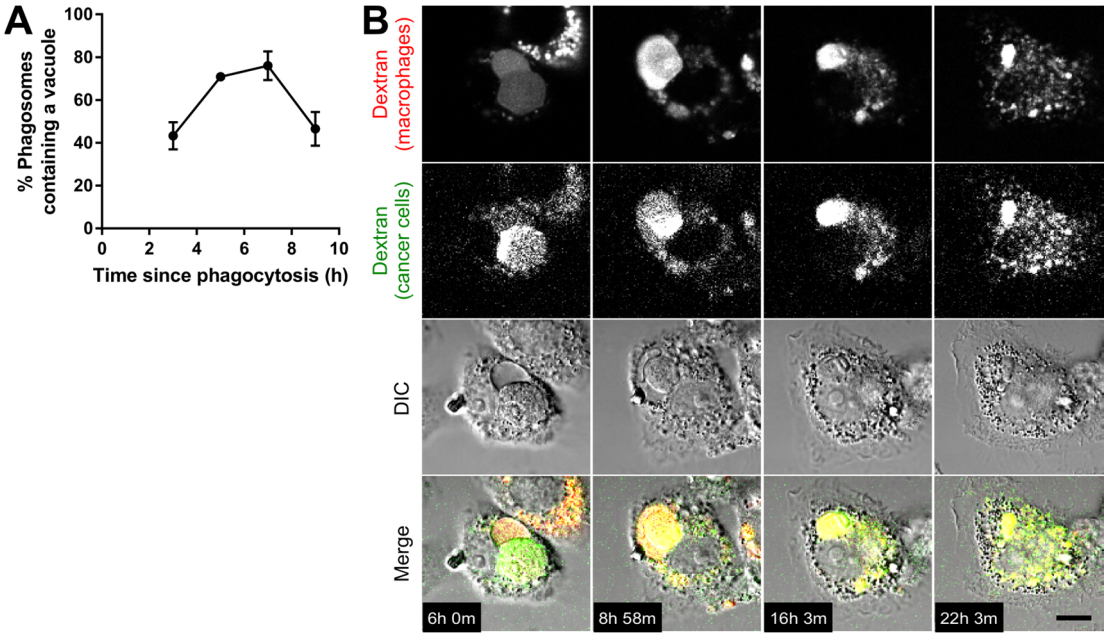

Figure 3-2 The contents of the phagosome and the vacuole are redistributed throughout the lysosomal network of the macrophage

A, MDA-MB-453 cells were opsonized with Alexa 488-labeled trastuzumab and co-incubated with J774A.1 macrophages preloaded with Alexa 647-labeled 10 kDa dextran. After co-incubation for 1 hour, 10 mg/ml IVIG was added to prevent further phagocytic activity. Images of the phagosomes were then taken at different time points, and the phagosomes with an associated vacuole were counted. Data from three independent experiments are plotted. Error bars represent standard errors. B, MDA-MB-453 cancer cells opsonized with trastuzumab were co-incubated with J774A.1 macrophages. The cancer cells were preloaded with Alexa 555-labeled 10 kDa dextran (pseudocolored green), and the macrophages were preloaded with Alexa 488-labeled 10 kDa dextran (pseudocolored red). Imaging was initiated 6 hours following the start of the co-incubation. The panels show 4 frames from the time series, with times corresponding to each frame indicated. Scale bars = 5 μm.

3.2.3 The phagosome and vacuole are discrete compartments

To investigate whether the vacuole is lysosomal in nature, we treated samples containing phagosome-associated vacuoles with the dye LysoTracker Red, which is membrane permeant and accumulates through trapping by protonation in acidic compartments, including lysosomes [144]. Interestingly, although the phagosome was, as expected from earlier studies [139], positive for LysoTracker, the dye was undetectable in the phagosome-associated vacuole (Figure 3-3A). To further explore the properties of the vacuole, we treated the samples with LysoSensor Blue DND-192, that is also membrane permeant and protonated in acidic compartments [145]. As expected, the phagosome was also positive for LysoSensor Blue fluorescence. Although the intensity of the LysoSensor staining in the vacuole was lower relative to that in the phagosome, LysoSensor signal could be detected in the vacuolar region, by contrast with very low to undetectable levels of LysoTracker signal (Figure 3-3B). Collectively, these data suggest that the pH of the vacuole is higher than that of the phagosome, and/or that the vacuolar membrane is not permeable to these dyes.

Although the vacuole had very low to undetectable levels of fluorescent signal from Lysotracker, we detected higher levels of fluorescence around the limiting membrane of the vacuole (Figure 3-3A, inset). Hence, to further understand the ultrastructural properties of the vacuole, we prepared specimens of phagocytosed target cells for analysis using transmitted electron microscopy (EM). EM images showed that the vacuoles had very low

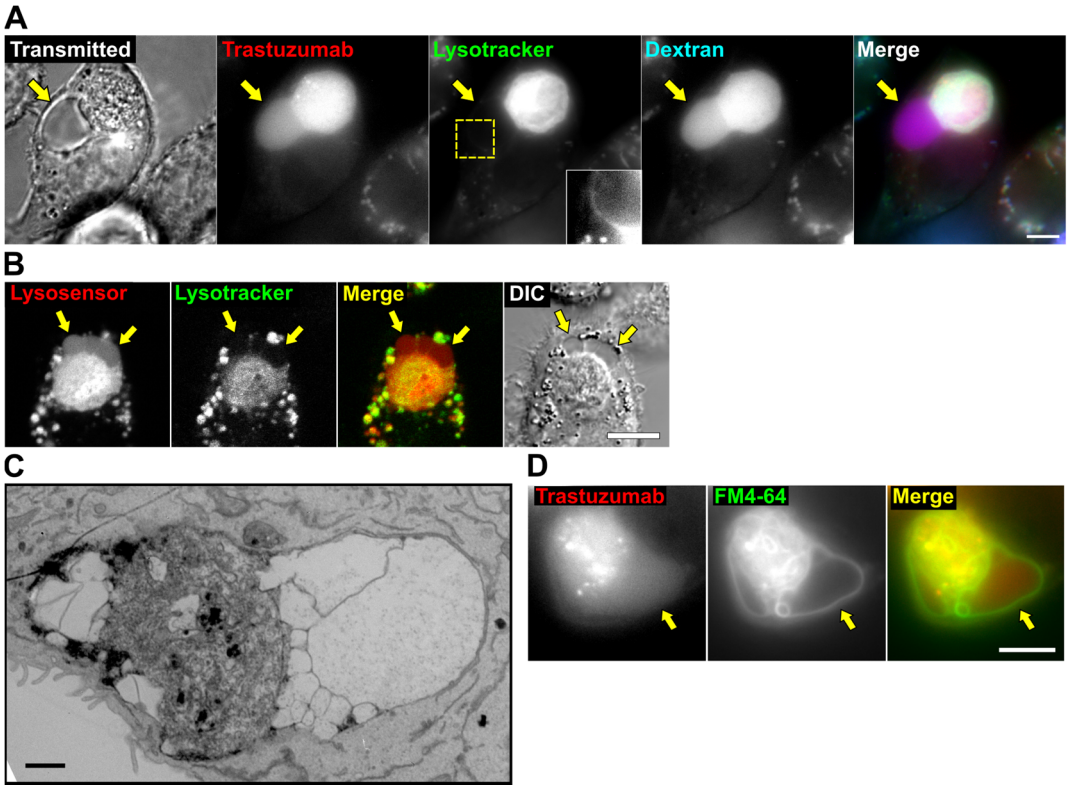

Figure 3-3 The vacuole contains membranous subcompartments

A, MDA-MB-453 cells were opsonized with Alexa 488-labeled trastuzumab (pseudocolored red), added to J774A.1 macrophages preloaded with Alexa 647-labeled 10 kDa dextran (pseudocolored blue), and incubated for 13 hours. Lysotracker Red (pseudocolored green) was then added to the medium, and the cells were imaged. The inset in the center panel corresponds to an enlargement of the cropped area (dotted lines) to show the region of interest with enhanced contrast. Scale bar = 5 µm. B, MDA-MB-453 cells were opsonized with trastuzumab and co-incubated with J774A.1 macrophages, and incubated for 6 hours. LysoSensor Blue (pseudocolored red) and LysoTracker Red (pseudocolored green) were then added to the medium, and the cells were imaged. Scale bar = 5 µm. C, MDA-MB-453 cells opsonized with trastuzumab were added to J774A.1 macrophages, incubated for 6 hours, fixed and processed for EM. An EM image of a phagosome with associated vacuoles is shown (representative of 9 phagosomes). Scale bar = 1 µm. D, MDA-MB-453 cells were harvested, labeled with the FM 4-64FX dye (pseudocolored green), opsonized with Alexa 488-labeled trastuzumab (pseudocolored red) and co-incubated with J774A.1 macrophages. Co-cultures were then incubated for 6 hours and imaged. Scale bar = 5 µm. Yellow arrows in A, B and D indicate the location of the vacuole.

density compared with the surrounding cytoplasm, whilst the target cell corpse had morphology analogous to that observed by others for cellular phagosomes (Figure 3-3C) [146]. The EM images of the vacuole also displayed membrane-limited subcompartments within this structure. To identify if these membrane sub-divisions are also found inside phagosome-associated vacuoles in live specimens, the target cells were labeled with the membrane dye FM 4-64FX before co-incubation with the macrophages. Analyses of phagosome-associated vacuoles with these FM dye-labeled targets revealed that this dye labeled the limiting membranes of subcompartments within the vacuolar region (Figure 3-4D).

The differential accumulation of pH-sensitive dyes in the vacuole suggested that the phagosome and vacuole are discrete compartments. However, the accumulation of Alexa Fluor dye following phagocytosis of cancer cells opsonized with Alexa 555-labeled trastuzumab indicated that some macromolecules could transfer between the compartments. To investigate whether the barrier between these two compartments limits movement of solutes above a particular size threshold, we labeled the surface of target cells with QDot 655-labeled trastuzumab. These quantum dot nanoparticles have an approximate diameter of 20 nm [147]. Vacuoles associated with phagosomes containing target cells did not contain any quantum dots, indicating that the barrier is impermeant to these nanoparticles (Figure 3-4A).

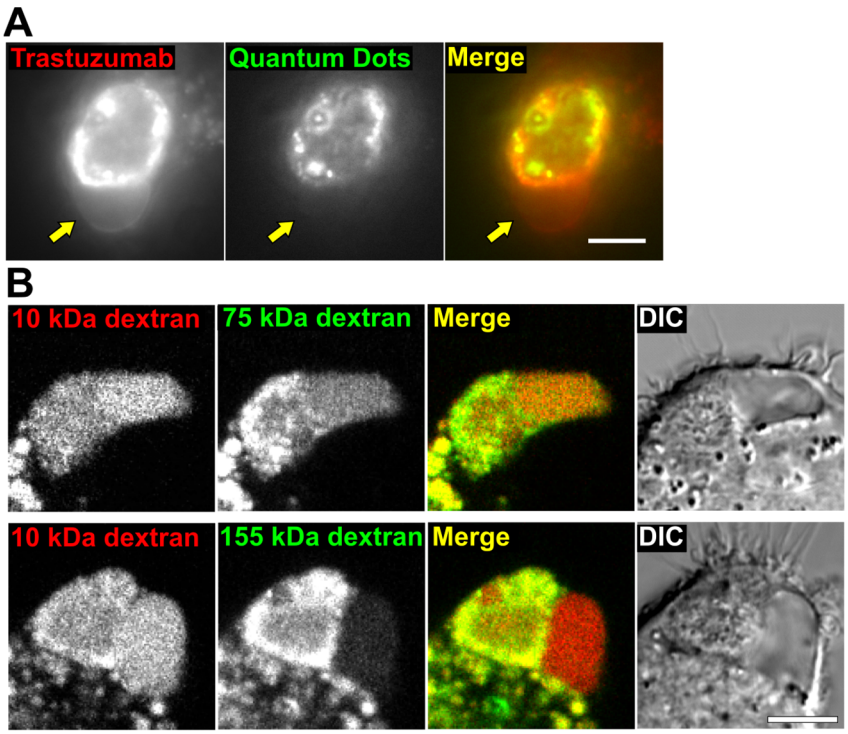

Figure 3-4 Inhibition of the mTOR pathway results in increased vacuole size

A, MDA-MB-453 cells opsonized with Alexa 488-labeled trastuzumab (pseudocolored red) were co-incubated with J774A.1 macrophages for 1 hour. The cells were then treated with DMSO vehicle control or Torin 1 (100 nM) in the presence of 10 mg/ml IVIG and incubated for 6 hours. LysoTracker Red (pseudocolored green) was then added to the medium and cells were imaged. Images show representative vacuoles observed for each treatment condition. B, the size of the vacuoles was quantitated by manually segmenting the areas positive for trastuzumab and negative for LysoTracker Red surrounding each phagosome and counting the number of pixels covered by these segmentations. The groups were compared using Student's t-test, and * indicates a statistically significant difference ($P < 0.01$). Scale bar = 5 μm.

Previous studies have used fluorescently labeled dextrans of different molecular weights to investigate the effect of size on subcellular transport processes (e.g. phagosomal-lysosomal and lysosomal fusion) [148,149]. We therefore labeled the lysosomes of the macrophage with fluorescent dextrans of different molecular weights (65-85 kDa, referred to as 75 kDa, and 155 kDa) and subsequently co-incubated these cells with trastuzumab-opsonized cancer cells. As a control, lysosomes of the macrophage were also labeled with 10 kDa dextran. When 75 kDa and 10 kDa dextrans were preloaded together in macrophage lysosomes, both dextrans accumulated in the vacuoles to similar levels (Figure 3-4B; 40/40 phagosomes). However, when 155 kDa and 10 kDa dextrans were preloaded together in macrophage lysosomes, the accumulation of 155 kDa dextran was substantially lower compared with 10 kDa dextran in the majority (81%, n = 71 phagosomes) of the vacuole compartments. The differential vacuolar localization of these dextrans and quantum dot nanoparticles indicate that the barrier between the phagosome and the vacuole can exclude the transfer of molecules/particles above a particular size threshold.

3.2.4 Formation of the phagosome-associated vacuole is independent of the effector or target cell-type

Using LysoTracker to differentiate the phagosome-associated vacuole from the phagosome, we investigated whether the phagosome-associated vacuole is observed for other macrophage:cancer cell couples. Target cells were co-incubated with bone marrow-derived macrophages and human monocyte-derived macrophages. Similar vacuole structures were associated with phagosomes for all macrophage types (Figure 3-5A,B). The vacuole was also observed when trastuzumab-opsonized SK-BR-3 breast cancer cells or

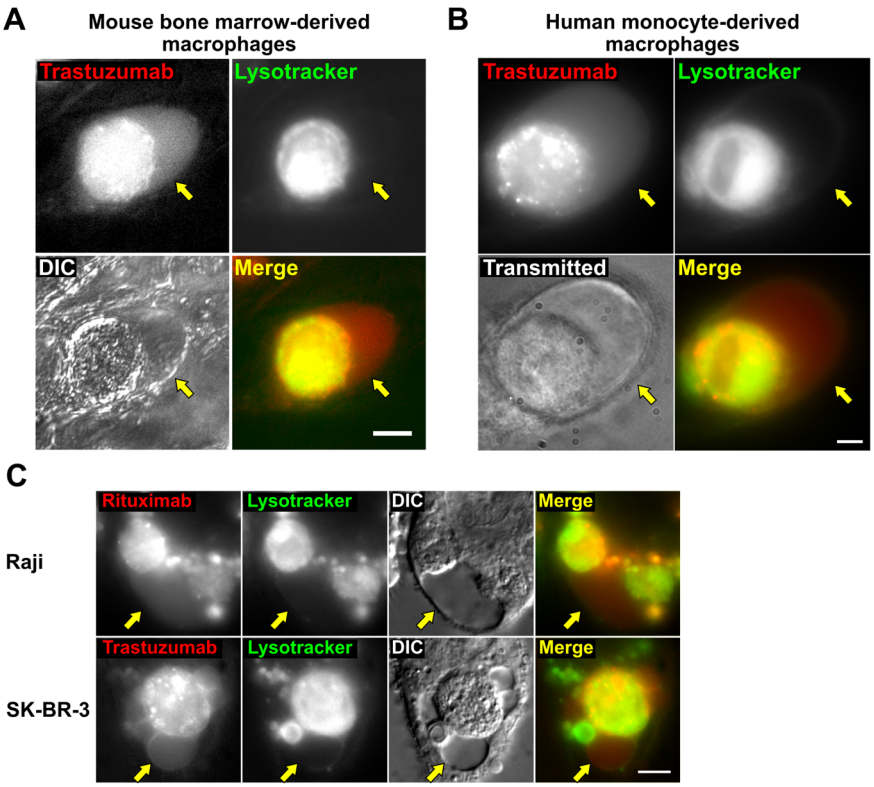

Figure 3-5 Phagosome-associated vacuoles are observed with multiple effector and target cell types

A, MDA-MB-453 cells opsonized with Alexa 488-labeled trastuzumab (pseudocolored red) were co-incubated with mouse bone marrow-derived macrophages for 6 hours, followed by addition of Lysotracker Red (pseudocolored green) and imaging. B, MDA-MB-453 cells opsonized with Alexa 647-labeled trastuzumab (pseudocolored red) were co-incubated with human monocyte-derived macrophages for 6 hours. Lysotracker Red (pseudocolored green) was then added to the medium, followed by imaging. C, Raji B cells opsonized with Alexa 647-labeled rituximab or SK-BR-3 cells opsonized with Alexa 488-labeled trastuzumab (pseudocolored red) were co-incubated with J774A.1 macrophages for 4.5 hours or 6 hours, respectively, followed by addition of Lysotracker Red (pseudocolored green) and imaging. Yellow arrows indicate the position of the vacuole. Scale bars = 5 μm.

anti-CD20 (rituximab)-opsonized Raji B cells were used as targets, indicating that the formation of this structure is not dependent on the target cell type or the specificity of the opsonizing antibody (Figure 3-5C).

3.2.5 The mTOR pathway regulates the size of phagosome-associated vacuoles

The presence of vacuoles adjacent to phagosomes containing live target cells, but not latex beads, suggested that vacuole formation is dependent on the generation of amino acids and/or other cellular metabolites by phagosomal degradation. The generation of amino acids in lysosomes is related to the mTOR signaling pathway [136]. This pathway affects lysosomal biogenesis and regeneration, with high levels of amino acids leading to the inhibition of transcription of genes associated with lysosome formation [137]. We therefore investigated whether treatment with Torin 1, an inhibitor of the mTOR pathway, altered the size of the vacuoles. Phagosome-associated vacuoles were observed in the presence of Torin 1 (Figure 3-6A), but their size increased (Figure 3-6B). These observations suggest that the formation of the phagosome-associated vacuole is related to the degradation and release of nutrients from the phagosome.

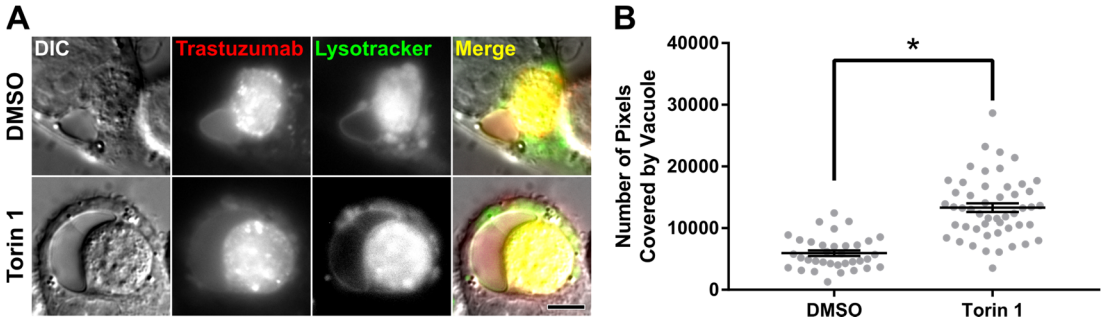

Figure 3-6 Inhibition of the mTOR pathway results in increased vacuole size

A, MDA-MB-453 cells opsonized with Alexa 488-labeled trastuzumab (pseudocolored red) were co-incubated with J774A.1 macrophages for 1 hour. The cells were then treated with DMSO vehicle control or Torin 1 (100 nM) in the presence of 10 mg/ml IVIG and incubated for 6 hours. LysoTracker Red (pseudocolored green) was then added to the medium and cells were imaged. Images show representative vacuoles observed for each treatment condition. B, the size of the vacuoles was quantitated by manually segmenting the areas positive for trastuzumab and negative for LysoTracker Red surrounding each phagosome and counting the number of pixels covered by these segmentations. The groups were compared using Student's t-test, and * indicates a statistically significant difference ($P < 0.01$). Scale bar = 5 µm.

3.3 DISCUSSION

In the current study, we describe a novel vacuolar structure that is formed during phagosomal maturation following macrophage-mediated phagocytosis of antibody-opsonized cancer cells. This vacuole is observed for three different macrophage:cancer cell combinations, suggesting that it is a universal structure associated with the phagocytic degradation of cellular targets. Although luminal space can be seen between the phagosomal 'body' and the limiting membrane of the phagosome in earlier electron micrographs, the space is contiguous with the phagosome [135,146,150]. By contrast, using EM and analyses of the differential accumulation of lysosomal tracers we demonstrate that the phagosome-associated vacuole described here is a discrete membrane-limited compartment (Figure 3-7).

Interestingly, LysoSensor Blue (DND-192) but not LysoTracker Red can be detected in the vacuole when these dyes are added shortly before microscopy analyses. However, fluorescence from both of these dyes, which are membrane permeant and localize to acidic compartments, is lower in the vacuole compared with the adjacent phagosome [151]. Two possibilities could explain this observation: first, the pH in the phagosome-associated vacuole may be higher than the pH in the phagosomal lumen. Second, the entry of these dyes into the vacuolar and phagosomal compartments differ. For example, if the phagosome-associated vacuole is encapsulated by multiple membrane layers, acidic pH in the lumen between these membrane layers could result in accumulation of the acidotropic probes in this space and limit their diffusion into the vacuole. This possibility is supported by the detection of Lysotracker fluorescence surrounding the vacuole. Nevertheless, the

higher fluorescent signal for LysoSensor relative to Lysotracker is likely to be due to the sensitivity of fluorescence of this dye to pH. Additional studies are required to establish the pH of the phagosome-associated vacuole and its permeability to such dyes.

We show that dextrans of distinct sizes are selectively excluded from the phagosome-associated vacuole. Differential sorting of molecules in macrophages has been previously observed to occur between lysosomes [149] and between lysosomes and phagosomes [148,152]. These studies led to the suggestion that such sorting might be caused by the diameter of the pores/tubules formed during potential kiss-and-run events that transfer solutes from one compartment to another [153]. Our data indicates that similar interconnections may exist between the phagosome and the associated vacuole. This is further supported by the exclusion of quantum dot nanoparticles from the vacuole.

The phagosome-associated vacuole appears to be specific for cellular targets since it was not observed for opsonized beads. A primary factor that differentiates cancer cells from other phagocytic targets is their composition: a typical mammalian cell has a protein concentration of 200 g/L [154]. Previous studies have indicated that signals produced by the release of amino acids from phagosomes feedback through the mTOR pathway to control the fate of the phagosome and its subsequent fission to generate lysosomal compartments [139]. We observe that phagosomes containing beads do not form associated vacuoles, indicating that the release of amino acids and activation of the mTOR pathway may be involved in their formation. Unexpectedly, we observe that the vacuole is enlarged when the mTOR pathway is inhibited, leading to the possibility that the inhibition of this

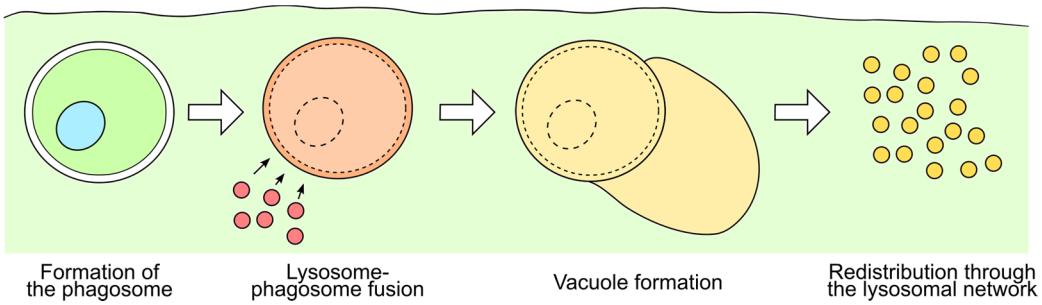

Figure 3-7 Schematic representation of the formation of the phagosome-associated vacuole

Following internalization of the antibody-opsonized cell, the lysosomes of the macrophage fuse with the phagosome. A distinct vacuole begins to form adjacent to the phagosome. Subsequently the phagosome and the vacuole shrink and their constituents are redistributed throughout the lysosomal network of the macrophage.

pathway triggers lysosomal biogenesis through the translocation of transcription factor EB (TFEB) [155]. This could result in increased lysosomal fusion with the maturing phagosome. Alternatively, the mTOR pathway is also known to play a role in the reformation of the lysosomal network from the phagosome [139,156,157]. Inhibition of the mTOR pathway could, therefore, inhibit the fission of the vacuole, resulting in enlargement.

While the function of the phagosome-associated vacuole appears to be primarily related to the controlled release of metabolites, additional functions may exist for this compartment. Early studies have suggested that the size of the phagosome may correlate with the quantity of metabolites it releases, due to excess osmotic pressure [135]. Similarly, the phagosome-associated vacuole could relieve such a buildup of osmotic pressure in a controlled manner. The differential accumulation of various solutes between the phagosome and the vacuole suggest that the vacuole may also act as a filter for the non-degradable or slowly degrading components of a large phagosome, separating and sequestering them from the degradable components. This possibility is supported by earlier reports suggesting that specialized lysosomal populations sequester such components [158,159].

Antigen presenting cells that are active in cross-presentation have been shown to maintain a higher pH in the antigen-loading compartments than cells that do not cross-present their antigen, indicating that lower degradative rates are important for this process [63,160,161]. Interestingly, our data are consistent with a higher pH in the vacuole compared with the phagosome, suggesting that this compartment could play a role in cross-presentation.

Although macrophages are typically regarded to be inefficient in this process, cross-presentation of antigen from target cells following ADCP has been reported [111]. Collectively, these observations suggest that the phagosome-associated vacuole may, therefore, be important for this pathway.

Collectively, our study has identified a novel vacuole-like compartment that is associated with maturing phagosomes that contain antibody-opsonized cells. Importantly, we demonstrate that this vacuole is distinct from the phagosome and is dependent on the release of nutrients such as amino acids. Future studies will be directed towards defining the role of this vacuole in antigen presentation and other cellular processes related to phagocytosis.

3.4 MATERIALS AND METHODS

3.4.1 Cell lines and primary cells

The cell lines J774A.1 (TIB-67), SK-BR-3 (HTB-30), Raji (CCL-86) and MDA-MB-453 (HTB-131) were purchased from the American Type Culture Collection. The cell lines were maintained in the following media supplemented with 10% fetal calf serum (FCS; Catalog no. 100-106, Gemini Bioproducts): macrophages and Raji cells, phenol red-free Dulbecco's Modified Eagle Medium (DMEM; 11965-092); MDA-MB-453, RPMI-1640 (11875-093); SK-BR-3, McCoy's (16600082). All experiments were conducted in medium containing FCS depleted of immunoglobulin G [131]. Long-term live imaging of macrophages was performed in Leibovitz's L-15 medium (11415-064) containing 10% FCS. Media were purchased from Thermo Fisher Scientific. Identities of the cancer cell lines were authenticated by short tandem repeat analysis (University of Arizona Genetics Core). Human monocytes were purchased frozen (Catalog no. 1008, Astarte Biologics) or were purified from peripheral blood mononuclear cells (PBMCs, kindly provided by Darrell Pilling, Texas A&M University) using the EasySep Human Monocyte Enrichment Kit (Catalog no. 19059, Stemcell Technologies). The monocytes were cultured in DMEM containing 10% FCS supplemented with 50 ng/ml Macrophage-Colony Stimulating Factor (Catalog no. 300-25, Peprotech) in MatTek glass bottom dishes (Catalog no. P35G-1.5-10-C). Bone-marrow derived macrophages were isolated from C57BL/6J mice (purchased from The Jackson Laboratory) as described previously [162].

3.4.2 Antibodies and other reagents

Clinical-grade trastuzumab, rituximab and IVIG (Gammunex) were obtained from the UT Southwestern Pharmacy. Trastuzumab and rituximab were labeled using Alexa 488 or 555 labeling kits (Thermo Fisher Scientific). The antibodies were labeled with 3-5 fluorophores per protein molecule. Trastuzumab was biotinylated as described previously [163]. Lysotracker Red (L7528), LysoSensor Blue DND-192, Alexa 488, 555 and 647-labeled dextran (10 kDa molecular weight; D-22910, D34679 and D-22914 respectively), FM 4-64FX (F34653), and F(ab')2-Goat anti-human IgG (H+L) secondary antibody conjugated Qdot 655 nanoparticles (Q-11221MP) were purchased from Thermo Fisher Scientific. Tetramethylrhodamine isothiocyanate-Dextran with average molecular weights of 155 kDa (T1287) or 65-85 kDa (represented as 75 kDa; T1162) were purchased from Sigma-Aldrich. Torin 1 (235-t-7887) was purchased from LC Labs. 10 μm-diameter Streptavidin-coated beads (CP01N) were purchased from Bangs Laboratories. All experiments were performed in cells plated in MatTek glass bottom dishes.

3.4.3 Sample pretreatment

For imaging phagosomes containing engulfed cancer cells, macrophages were first plated in MatTek glass bottom dishes. J774A.1 macrophages were plated overnight in the presence of 25 ng/ml murine Interferon-γ (Catalog no. 315-05, Peprotech). Mouse bone marrow-derived macrophages were similarly activated overnight with Interferon-γ. Purified human monocytes were directly plated in MatTek glass bottom dishes 6 days prior to the experiment. Human macrophages were activated with human Interferon-γ overnight. To label the lysosomes of macrophages with dextran, the macrophages were incubated

with medium containing 100 µg/ml labeled dextran for 1 hour, washed and incubated with medium for 2-4 hours prior to the addition of target cells. To label cancer cell lysosomes with dextran, they were incubated with 100 µg/ml dextran overnight, washed and incubated with medium for 4 hours prior to addition to the macrophages.

3.4.4 Phagocytosis of cancer cells by macrophages

The cancer cells were harvested from flasks by mild trypsinization, washed and incubated with 10 µg/ml labeled opsonizing antibody for 10 minutes at room temperature. The cells were then washed twice with Phosphate-Buffered Saline (PBS) followed by re-suspension in medium. Cancer cells were added to macrophages at 1:0.875 effector:target ratios (35,000 target cells were added to 40,000 plated macrophages in 10 mm MatTek glass bottom dishes) and incubated for various time points before imaging. If necessary, the medium in the dishes was replaced with medium containing 10 mg/ml IVIG to block further phagocytosis after one hour. Prior to imaging, Lysotracker Red (2 nm final concentration) and Lysosensor Blue (50 nm final concentration) were added to the medium and incubated at room temperature for 5 minutes to label the acidic compartments.

3.4.5 EM sample preparation

Cells were fixed on gridded MatTek dishes (Catalog no. P35G-1.5-14-CGRD-D) with 2.5% (v/v) glutaraldehyde in 0.1M sodium cacodylate buffer. After three rinses in 0.1 M sodium cacodylate buffer, they were post-fixed in 1% osmium tetroxide and 0.8 % K3[Fe(CN6)] in 0.1 M sodium cacodylate buffer for 1 h at room temperature. Cells were rinsed with water and en bloc stained with 2% aqueous uranyl acetate overnight. After

three rinses with water, specimens were dehydrated with increasing concentrations of ethanol, infiltrated with Embed-812 resin and polymerized in a 60°C oven overnight. Blocks were sectioned with a diamond knife (Diatome) on a Leica Ultracut UC7 ultramicrotome (Leica Microsystems) and collected on copper grids, followed by post-staining with 2% uranyl acetate in water and lead citrate. Images were acquired on a Tecnai G2 Spirit transmission electron microscope (FEI) equipped with a LaB6 source using a voltage of 120 kV.

3.4.6 Microscope configurations

For single time-point imaging, images were acquired using a Zeiss Axiovert 200M inverted fluorescence microscope with a Zeiss 63x/1.4NA Plan Apochromat objective as described previously [133]. Long-term live imaging of the formation of the vacuole was imaged using a Zeiss Axio Observer.A1 body and a Zeiss 63x/1.4NA Plan Apochromat objective. The sample was illuminated with a 488-nm solid-state laser (Coherent) for Alexa 488 excitation and a 543-nm diode laser (Opto Engine LLC) for Alexa 555 excitation. The illumination was directed to the sample and fluorescence filtered back using a polychroic beamsplitter/emission filter combination (488/543/633 RPC and 488/543 M; Chroma Technology Corporation). The fluorescence emission was detected using an Andor iXon EMCCD camera (Andor Technologies). The cameras were run on conventional gain mode and images were acquired in two colors along with a transmitted light image at an acquisition rate of 1 per minute. Camera acquisition and shuttering of excitation lasers were controlled using custom acquisition software written in LabWindows/CVI (National Instruments Corporation). The acquired images were registered and processed using the

Microscopy Image Analysis Tool (http://wardoberlab.com/software/miatool) [134] implemented in MATLAB (MathWorks, Inc). The temperature and humidity in the microscope system were maintained by a caged temperature-control system (OKOlabs). Long-term imaging of the degradation of the vacuoles, the imaging of Lysosensor staining and the imaging of the different molecular weight dextrans were performed using a Nikon A1R confocal microscope equipped with a 60X 1.4 NA Plan Apo objective and a temperature-control system. The acquired images were exported to TIFF format and processed with Microscopy Image Analysis Tool as described above.

CHAPTER FOUR
INTENSITY-BASED AXIAL LOCALIZATION APPROACHES FOR MULTIFOCAL PLANE MICROSCOPY

This study has been published in the journal *Optics Express* [Velmurugan R, Chao J, Ram S, Ward ES, and Ober RJ. (2017) Intensity-based axial localization approaches for multifocal plane microscopy. **Optics Exp** 25(4): 3394-3410]. It has been reprinted here with permission from the Optics Society of America.

4.1 INTRODUCTION

The ability to accurately estimate the three-dimensional (3D) location of a point source can now be achieved through several techniques such as multifocal plane microscopy (MUM) [79,96,100,164], the induction of astigmatism in the Point-Spread Function (PSF) [95], the engineering of the PSF to encode axial information [94,165] and interferometry-based approaches [166]. While all these methods achieve comparable levels of axial localization accuracy, the range of axial locations imaged by a MUM configuration can be increased just by adding more cameras to the setup. While other 3D imaging modalities can typically cover axial depths of up to 3 μm [165], MUM configurations with four focal planes can, for example, be used to image through axial depths greater than 8 μm, an imaging window that can cover the full thickness of a typical mammalian cell [98]. To estimate the axial location of a point source using MUM, images of the point source from different detectors (or different regions in the same detector), each capturing a different focal plane within the sample, can be fitted to a model that recapitulates the PSF of the microscope configuration. Such a parametric fitting algorithm, named the MUM Localization Algorithm (MUMLA),

was first described for the case of MUM with two focal planes [96,167], but has also been extended to MUM with more focal planes [98].

We have also previously developed a Practical Localization Accuracy Measure (PLAM) [88], a quantity based on Fisher information that gives the best possible accuracy, in terms of the standard deviation, with which a positional coordinate of an object can be estimated given the exact properties of the optical configuration. MUMLA has previously been shown to provide estimates whose standard deviation approaches the PLAM [96], and hence would be the method of choice if estimates of the highest accuracy are desired. However, a non-parametric algorithm that can rapidly provide an estimate of the axial location of a point source can complement MUMLA. A primary reason is that the fitting of a PSF model to MUM data requires complex PSF fitting algorithms, computational power to perform the fitting, and an appropriate choice of the PSF model. The ability to quickly calculate an estimate of the axial location of a point source can hence allow faster initial analyses of experimental data. Should more accurate results be required, non-parametric estimates can serve as initial conditions for more rigorous fitting algorithms like MUMLA.

Watanabe and colleagues [99] have previously published such a non-parametric method based on intensity ratios (the ratiometric method) that can be used to quickly calculate the axial location of a point source using data from a two-plane MUM setup. In this method, the peak intensities of a point source in the images from the two focal planes are used to calculate a ratio as described before [79]. Using a pre-determined lookup table of such

ratios for known axial positions of a calibration point source, the axial location of a given point source can be estimated based on its calculated ratio.

A similar method that utilizes a sharpness value has been characterized by Dalgarno and colleagues [100], where data from MUM configurations with more than two focal planes can also be utilized. These and earlier methods [79] estimate the axial location of a point source using a single intensity value calculated per focal-plane image of the point source. This motivates the question of how accurately the axial location of a point source can be estimated from such single-intensity calculations, and whether the accuracy of these methods can be improved by modifying these calculations.

We analyze this question by investigating the Fisher information and the associated PLAM that can potentially be attained by using intensity values from different regions of the detectors in a MUM setup. These analyses show that at least in some cases, using a single integrated intensity value per detector can provide an axial localization accuracy that is comparable to the accuracy obtained by applying MUMLA on the pixelated image as is. However, the PLAM calculations also show that such single-intensity-value methods cannot provide consistently good accuracy over large axial ranges. To address this important drawback, we propose a new axial location estimation approach, Multi-Intensity Lookup Algorithm (MILA), that is based on utilizing intensity values from several different parts of the point source's image. We show that this approach significantly improves on the associated PLAM over the use of a single intensity per detector. We establish that MILA provides good axial localization accuracy over a much wider axial range compared to

single-intensity localization methods. We also identify a bias encountered in MILA due to sub-pixel location differences between point sources, and demonstrate the use of multiple calibration point sources to overcome this problem. We evaluate the performance of MILA using both simulated and experimental data. We believe that the versatility and simplicity of our new method will prove useful in the analysis of MUM data.

4.2 RESULTS

4.2.1 Comparison of axial localization accuracy between single-intensity methods and MUMLA

Both the ratiometric [99] and the sharpness [168] methods estimate the axial location of a point source by utilizing just a single intensity value from the image of the point source captured by each detector. In order to understand whether a single integrated intensity value per detector can represent meaningful axial location information, we calculated the PLAM for the axial location when the axial location of the point source is estimated using one "summed-pixel" from each detector, obtained by adding all the pixels comprising the given sub-ROI. This Summed-Pixel Based PLAM (SPB-PLAM) represents the best axial localization accuracy that can potentially be attained by a method that utilizes only the single intensity value from each detector. Figure 4-1 shows plots of such SPB-PLAM values as a function of the axial position of a simulated point source when it is imaged by two-plane MUM configurations with increasing focal plane separations. For reference, the standard axial localization PLAM value for the same point source, when it is simulated as being captured in a pair of 13×13-pixel ROIs, is also plotted. This standard PLAM value [88] represents the best accuracy that can potentially be achieved with an estimation algorithm like MUMLA that uses all pixel intensities as they are in both ROIs.

We observe that for the 0.4-μm and 0.6-μm plane separations, the SPB-PLAM curves for summed-pixels of sizes 16 μm and 48 μm stay close to the standard PLAM curve over a large axial range of 1.5 μm, indicating that for small plane separations a single-intensity-based axial localization method may suffice for some applications. However, the same is

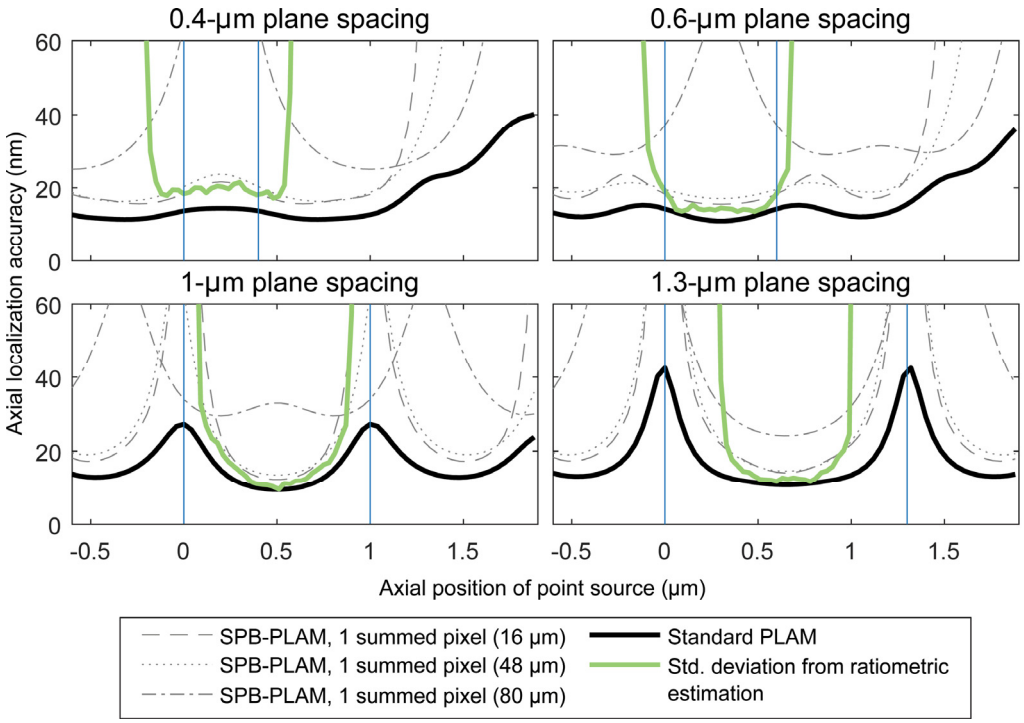

Figure 4-1: Plots of the standard PLAM and SPB-PLAMs for the axial location of a simulated point source as a function of its axial location

The standard deviation of 1000 axial location estimates obtained using the ratiometric method is also shown. Sub-panels show plots of these values in simulations with different focal plane spacings in a two-plane MUM configuration. PLAM calculations were performed with the following numerical values: magnification $M = 100$, numerical aperture $n_a = 1.45$, pixel size: $16\ \mu m \times 16\ \mu m$, ROI size: 13×13 pixels. Here, the 16-µm, 48-µm and 80-µm sizes of the summed-pixels correspond to areas that cover sub-ROIs of 1×1, 3×3 and 5×5 pixels, respectively, that are centered in the 13×13-pixel ROI. The point source was simulated such that a mean of 4000 photons were detected per image. The ratiometric method utilizes the entire 13×13-pixel ROI for its Gaussian fitting and its calibration data was generated using data from one simulated point source with all the same parameters except that a mean of 10000 photons were detected per image. Standard deviation values for the ratiometric method are only plotted for axial positions where the mean of the estimates does not deviate more than 50 nm from the simulated axial position. Vertical lines mark the positions of the focal planes in the object space.

not observed for a focal plane separation of 1 μm or higher, in which case no single SPB-PLAM curve stays consistently close to the standard PLAM over the same large axial range.

Watanabe and colleagues [99] described the ratiometric method that uses intensity estimates obtained by fitting 2D Gaussian profiles to images of the point source from two focal planes. The performance of this method was also tested for the same conditions using simulated images, and the standard deviation of the obtained axial location estimates is shown in Figure 4-1. The standard deviation is only plotted for axial locations where the mean estimated value does not differ from the simulated axial location by more than 50 nm. While the ratiometric method, which uses the entire 13 × 13-pixel ROI for the 2D Gaussian fitting, performs better than the SPB-PLAM values in some cases, the utility of this method is limited by the small axial region within which it is able to give estimates that are reasonably close to the true axial location.

Note that compared to all the SPB-PLAM curves, in all scenarios the standard PLAM always represents the best attainable accuracy. This is consistent with expectation because by taking into account the individual intensity values of all the pixels that comprise the ROI, the standard PLAM is based on the Fisher information content of the most fine-grained spatial representation of the PSF.

4.2.2 Performance of MILA as a non-parametric axial location estimator for MUM data

Since the SPB-PLAM values corresponding to a single summed-pixel per detector do not remain consistently close to the standard PLAM when large focal plane spacings are used, we hypothesized that a combination of multiple summed pixels per detector might provide more axial localization information throughout the axial range of a wide-spaced MUM configuration. Hence, we propose a new method, the Multi-Intensity Lookup Algorithm (MILA), which calculates the intensity values of multiple summed pixels from the ROI in each detector. A schematic representation of the method is shown in Figure 4-2A. If intensities are extracted from ROIs around the point source location as shown, we can generate a set of calibration curves (Figure 4-2B) which can then be used as a lookup table. The r sequence specifies the number and sizes of the sub-ROIs that are chosen to be used in this method (see Appendix 4-5 for the definition and an illustration of the r sequence).

To test the performance of MILA, we simulated images of a point source located at various axial positions as acquired using a two-plane MUM configuration. We then estimated the axial location of the point source using this method with two different r sequences. For comparison, we also estimated the axial location using the ratiometric method. From the upper panel of A, we observe that MILA ($r = 1,2$) (red line) is able to give us estimates

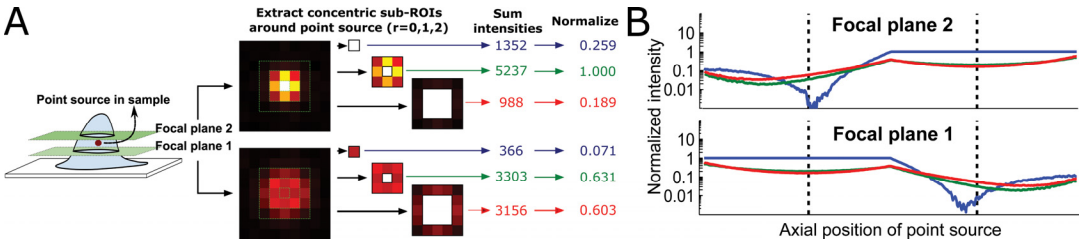

Figure 4-2: Schematic representation of the MILA method

A: Schematic representation of the method of extracting multiple summed intensity values from MUM images of a point source. B: Plot of normalized intensities for a typical point source as a function of its axial position. Vertical dotted lines indicate the position of the focal planes in the object space (focal plane 1 is the dotted line on the left).

with relatively low standard deviation over a wide range of axial locations that even extends to regions outside the two focal planes. While the ratiometric method (green line) also gives accurate estimation results for point sources situated between the two focal planes, the estimates from this method are not reliable when the point source is outside the focal planes due to bias in the estimated values (Figure 4-3A, lower panel). Thus, MILA can produce consistently good localization accuracy with relatively little bias over a wider axial range than the ratiometric method. Note that when only one sub-ROI (e.g., $r = 1$, Figure 4-3A, blue line) is used for intensity calculation, the results of MILA become comparable to the ratiometric method, giving high accuracies between the focal planes but being unusable outside that axial region due to unacceptably large bias.

In order to further understand the performance of MILA, we calculated an SPB-PLAM curve that gives the best accuracy attainable given the sub-ROIs used with this method. The top panel in Figure 4-3B shows that the SPB-PLAM curve calculated with two sub-ROIs ($r = 1,2$) trails the standard PLAM curve by less than 10 nm over a wide axial range. Further, we also observe that the standard deviation of estimates obtained using MILA ($r = 1,2$) trails the SPB-PLAM curve between the focal planes. However, this standard deviation diverges from the SPB-PLAM curve outside the focal planes, demonstrating that while MILA provides accurate axial location estimates over the entire axial range, the simple lookup method does not behave as a perfect estimation algorithm, whose accuracy would be expected to come close to the corresponding SPB-PLAM across all axial positions. From the bottom panel of Figure 4-3B, we observe that the SPB-PLAM curve for $r = 1$ rapidly increases beyond 50 nm when the axial position of the point source comes

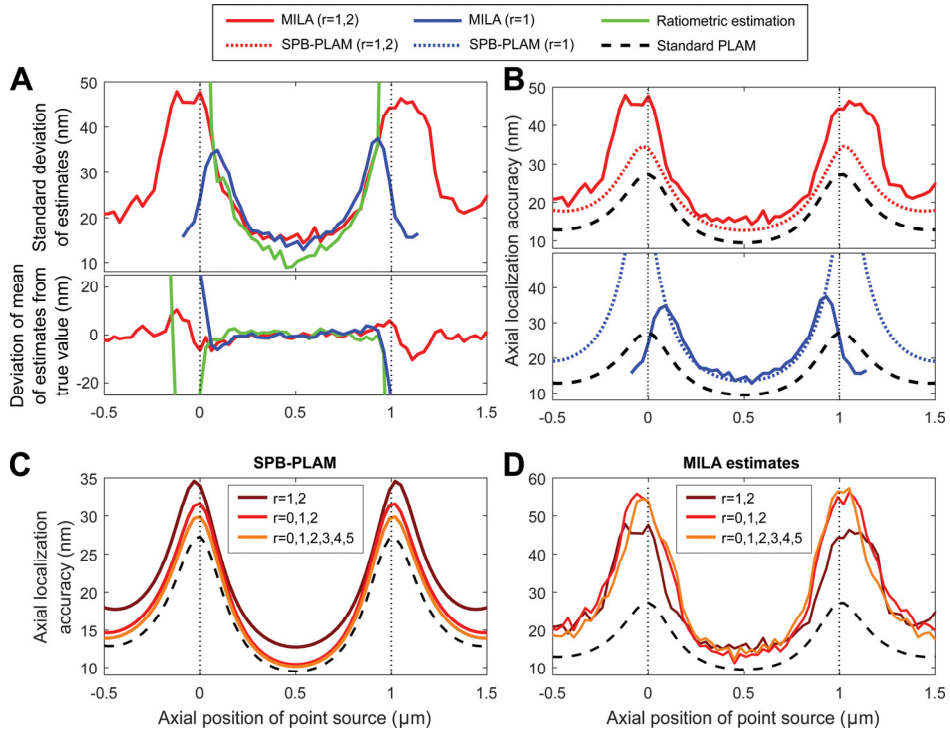

Figure 4-3: Performance of MILA as compared to other non-parametric axial localization methods

A: The top panel shows the standard deviation of axial location estimates, obtained from 3 non-parametric algorithms when applied to 1000 pairs of simulated two-plane MUM images of a point source from which a mean of 4000 photons were detected per image, as a function of the axial position of the point source. The bottom panel shows the deviation of the mean of the same estimates from the true axial position of the simulated point source. The red line shows the values obtained using MILA ($r = 1, 2$) and the green line represents values obtained using the ratiometric method. The blue line shows values obtained using MILA ($r = 1$), which uses only one sub-ROI. B: Plots of the SPB-PLAM and the standard deviation of MILA estimates for the axial location of a simulated point source calculated for $r = 1, 2$ (top) and $r = 1$ (bottom). C: Plots of SPB-PLAM curves for different sub-ROI combinations as indicated in the legend. D: Plots of the standard deviation of MILA estimates for the axial location of a simulated point source for different sub-ROI combinations as indicated in the legend. The dashed black line in B, C and D indicates the standard PLAM for axial localization from the full ROI. The simulations were performed with the following numerical values: magnification M = 100, numerical aperture $n_a = 1.45$, pixel size: $16\ \mu m \times 16\ \mu m$, ROI size: 15×15 pixels. The calibration data was generated using data from one simulated point source with all the same parameters except that a mean of 10000 photons were detected per image. Vertical dotted lines mark the positions of the focal planes in the object space.

close to either focal plane. The standard deviation of the corresponding MILA estimates also trails the SPB-PLAM curve between the two focal planes, but the two curves begin to diverge near the focal planes. Around the points of divergence, the SPB-PLAM continues to increase in magnitude as the MILA estimates become unusable due to excessive bias. To investigate the effect of using more sub-ROIs with MILA, SPB-PLAM curves were calculated with increasing numbers of sub-ROIs. Figure 4-3C shows that with increasing numbers of sub-ROIs, the SPB-PLAM curves gradually approach the standard PLAM curve, a pattern that is expected because the addition of sub-ROIs should increase the total Fisher information content of the data. However, Figure 4-3D shows that the standard deviations obtained from MILA estimations with the corresponding larger numbers of sub-ROIs did not improve concomitantly. This is possibly due to the estimation task being made more challenging by the inclusion of pixels with lower signal-to-noise ratios in the larger sub-ROIs. These are pixels that contain the same levels of background and read-out noise as the other pixels in the ROI, but detect significantly smaller levels of signal from the point source.

4.2.3 MILA can also be used in MUM configurations with more than two focal planes

Next, we characterized the performance of MILA when applied to data from MUM configurations having more than two focal planes. One of the primary applications of MUM is to study the dynamics of single particles that traverse the entire volume of mammalian cells, which are typically 6 to 8 μm thick. A four-camera MUM configuration with focal plane separations of about 1.5 to 2 μm between the detectors can cover such an

axial range [98]. Such wide plane spacings become particularly challenging for non-parametric methods due to the nature of the Fisher information landscape for axial location estimation in these configurations. Hence, we tested the performance of MILA in a four-plane configuration with the smallest plane spacings that can cover the axial thickness of a mammalian cell. The schematic of such a wide-spaced MUM configuration with four focal planes and the extracted ROIs and sub-ROIs are shown in Figure 4-4A. We performed estimations on simulated data arising from such a configuration, where the optical parameters were kept the same as in previous cases but the number of focal planes and the inter-plane spacing alone were increased.

As shown in the top panel of Figure 4-4B, even with an inter-plane spacing of 1.5 μm, MILA can provide axial location estimates with a standard deviation of less than 60 nm over an axial range of 6.5 μm when four detectors are simulated. However, given the larger focal-plane separation, more sub-ROIs ($r = 0,1,2,3,4,5$) are required for MILA to perform optimally and the standard deviation is consistently worse than the standard PLAM by 20 to 40 nm. Furthermore, the corresponding SPB-PLAM curve is observed to closely trail the standard PLAM, predicting that an estimator that uses the six-sub-ROI combination can potentially produce accurate axial location estimates comparable to the standard PLAM. In contrast to what was observed with the previous 1-μm plane spacing configuration (Figure 4-4C), SPB-PLAM curves with fewer sub-ROIs can significantly diverge from the standard PLAM near the focal planes, and this is illustrated in the bottom

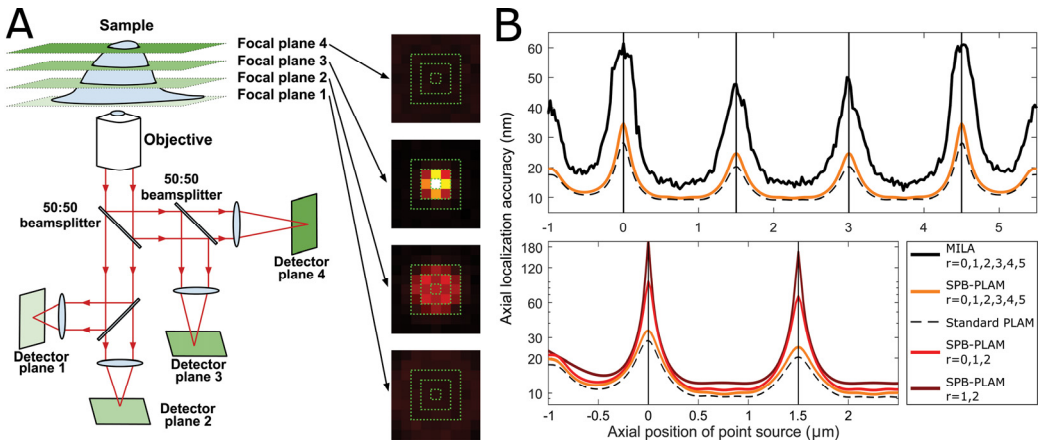

Figure 4-4: Performance of MILA in a four-plane MUM configuration

A: Schematic representation of a MUM configuration that simultaneously images four focal planes using independent detectors. Sample ROIs of a typical point source are also shown, along with a representation of the sub-ROIs that are used for intensity calculations. B: The top panel shows a plot of the accuracy reached by MILA ($r = 0, 1, 2, 3, 4, 5$) in the estimation of the axial location of a point source using four-plane MUM data. 1000 sets of four images corresponding to the four focal planes of a point source from which a mean of 2000 photons were detected per image were simulated and the point source's axial location was estimated using MILA. The standard deviation of these estimates is plotted as a function of the axial position of the simulated point source. The corresponding SPB-PLAM and standard PLAM for the axial location of the point source are also plotted. The bottom panel shows a plot of the SPB-PLAM calculated for different sub-ROI sequences for the same data as a function of the point source's axial location. The axial location range shown is restricted to one-half of the simulation range and the y-axis is depicted in log10 scale for display purposes. The simulations were performed using the following numerical values: magnification $M = 100$, numerical aperture $n_a = 1.45$, pixel size: $16\,\mu m \times 16\,\mu m$, ROI size: 15×15 pixels. The calibration data was generated using data from one simulated point source with all the same parameters except that a mean of 10000 photons were detected per image. Vertical lines mark the positions of the focal planes in the object space

panel of Figure 4-4B.

Based on what is seen in the top panel of Figure 4-4B, the simple lookup approach used in MILA appears to be unable to perform comparably to its corresponding SPB-PLAM in such a demanding MUM configuration with wide focal plane spacings. This shows again that although from an information-theoretic perspective, the addition of more sub-ROIs should only increase the amount of information available to an estimator, simple lookup methods like MILA may not be able to fully leverage the entirety of this information in certain scenarios. Hence, with demanding wide-spaced MUM configurations, parametric estimation methods that can come close to the standard PLAM may be preferred if estimating the axial location with very high accuracy levels is of importance.

4.2.4 Differences in the location of the point source within the center pixel can bias non-parametric axial location estimates

In the previous figures, the calibration data was obtained from only one point source whose position was the same as that of the test point source. However, point sources located at various positions within a single pixel will produce different images due to changes in the position of the pixel borders relative to the point source position (Figure 4-5A). Hence, the intensities calculated using a non-parametric method will not be the same even for similar point sources that differ only in their sub-pixel location. When the point source generating the calibration data is not located in the same sub-pixel location as the point source for which the location is being estimated, this discrepancy can lead to bias in the estimated axial location.

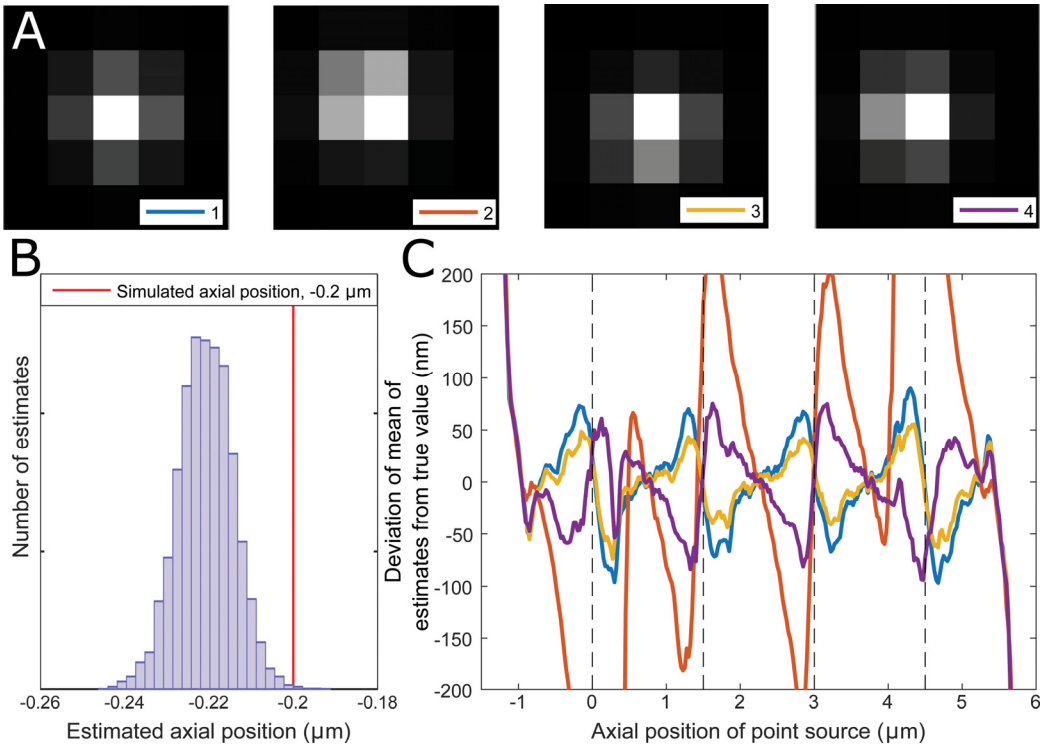

Figure 4-5: Effect of sub-pixel localization differences on the estimation of the axial location of the point source

A: Example images of four simulated point sources that differ only in their locations within the center pixel of the ROI. B: Histogram of 10000 axial location estimates of a point source obtained using MILA when the calibration point source used to generate the lookup table is located at a different sub-pixel location. Red line indicates the true axial position. C: Plot of the bias in the axial location estimates of four different point sources as a function axial location. The lateral positions of these point sources are shown in A. Each colored line represents bias in the estimates of one of the point sources. Bias is calculated as the difference between the mean of 1000 axial location estimates and the true axial location. The axial location was estimated using MILA from simulated four-plane MUM data. The point sources were simulated such that a mean of 2000 photons were detected per image. Simulations and estimations were performed using the following numerical values: magnification $M = 40$, numerical aperture $n_a = 1.45$, pixel size: $13\ \mu m \times 13\ \mu m$, ROI size: 11×11 pixels, sub-ROI sequence $r = 0, 1, 2$. The calibration data was generated as a series of images of a fifth point source located at another random position within the center pixel of the ROI, from which a mean of 10000 photons were detected per image. Vertical dotted lines mark the positions of the focal planes in the object space.

In order to demonstrate the extent of this potential bias, we simulated test images of four different point sources that only differ in their location within the center pixel of the ROI. Their axial locations were then estimated using calibration data generated using a single point source which was also located within the center pixel of the ROI. A histogram of such MILA estimates for one point source at one axial location shows a clear offset in the distribution of estimates from the simulated axial position, indicating that the deviation of the mean of these estimates might arise from systematic bias in the lookup method (Figure 4-5B). When the means of such estimations are calculated at different axial positions for each of the four test point sources, we observe that there are significant deviations of these mean values from their respective simulated axial positions (Figure 4-5C). We also observe that the bias is more pronounced for some point sources than others, indicating that the bias appears to depend on the particular position of the point source within the pixel with respect to the sub-pixel location of the calibration point source.

4.2.5 Including calibration data from several point sources in MILA reduces the sub-pixel localization bias

The bias caused in MILA by sub-pixel location differences can be reduced by using calibration data from several point sources instead of just one, as this increases the probability that we have calibration data from a point source that is similar in sub-pixel position to a given point source. In order to identify the axial location of a test point source using data from several calibration point sources, we perform a global least squares minimization (Appendix 4-5). Figure 4-6A shows a plot similar to Figure 4-5C, but where we utilize calibration data from 50 different point sources. One can see that the bias in the

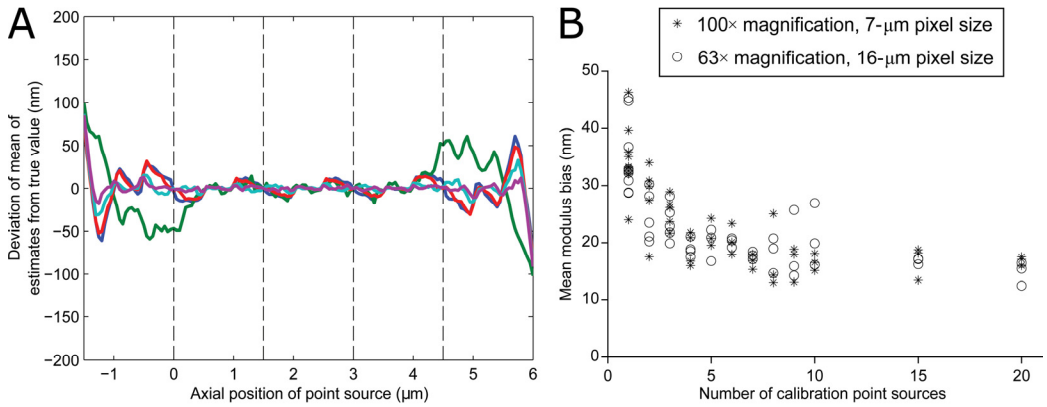

Figure 4-6: Correction of sub-pixel localization bias in MILA

A: Plots of the difference between the mean of 1000 axial location estimates and the true axial location as a function of the axial location for five simulated point sources that are imaged using a four-plane MUM setup. Calibration data from 50 different point sources were used. Each colored line represents bias in the estimates of one of the five test point sources. Simulations and estimations were performed using the following numerical values: focal-plane separation: 1.5 μm, magnification $M = 40$, numerical aperture $n_a = 1.45$, pixel size: $13\ \mu m \times 13\ \mu m$, ROI size: 11×11 pixels, sub-ROI sequence $r = 0, 1, 2$. The five test point sources were positioned in various locations within the center pixel of the ROI and the calibration data was generated as a series of images of 50 different point sources located in random locations within the same center pixel. A mean of 2000 photons were detected per image from each of the five test point sources, and a mean of 10000 photons were detected per image from each calibration point source. B: Plot of the mean modulus bias in the obtained axial location estimates as a function of the number of calibration point sources used. Test and calibration data were simulated similar to A, but calibration curves were generated with different numbers of point sources whose positions within the center pixel were randomized every time. For each test point source, datasets were simulated that differ by the axial location of the point source. The mean modulus bias is the average of themodulus bias of the axial estimates obtained for each dataset. All simulation parameters were maintained as above, except the magnification and pixel size were varied as indicated in the legend.

estimates has been significantly reduced at all the axial positions. One factor that affects the quality of this bias-correction method is the number of calibration point sources to use. To study this, axial location estimations similar to those carried out for Figure 4-6A were performed for two magnification-pixel size combinations using varying numbers of calibration point sources. For each test point source considered, datasets corresponding to multiple axial positions of the point source were subjected to MILA estimation, and an average was taken of the modulus bias of the axial location estimates obtained for each dataset. Plotting this mean modulus bias in the axial estimates against the number of calibration point sources shows that the average bias decreases rapidly as the number of calibration point sources used increases, but does not change significantly as long as more than five calibration point sources are used (Figure 4-6B).

4.2.6 Evaluation of MILA using experimental data

We tested the efficacy of MILA on bead data acquired from a four-plane MUM configuration. As shown in Figure 4-7A, the standard deviation for the axial location estimation of a typical bead is consistently maintained below 40 nm over a range of 4 μm between the four focal planes. This demonstrates that the method can also be successfully used with experimental data. The bias, as given by the deviation of the mean of the estimates from the expected axial location based on the step size used for the piezo nanopositioner between image acquisitions, is also kept low in these estimations (Figure 4-7B).

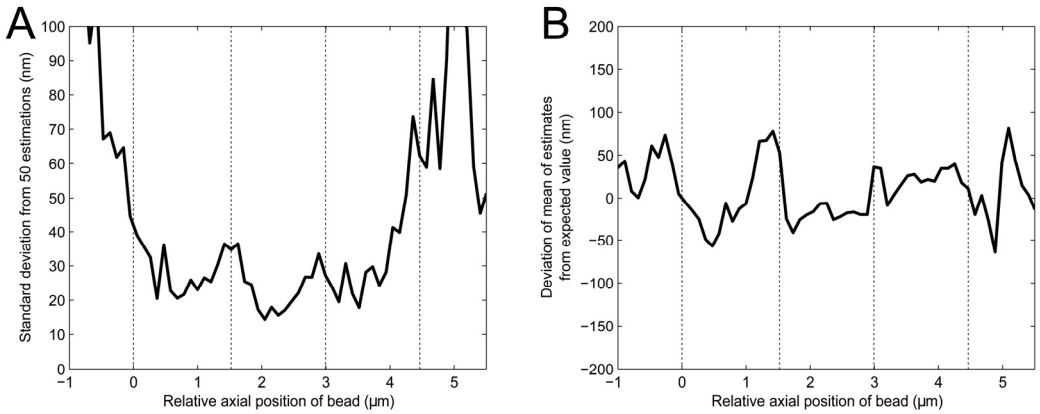

Figure 4-7: Performance of MILA in real data

A: Standard deviation of z estimates, obtained using MILA from 50 sets of four images (each corresponding to a distinct focal plane) per axial position of a typical 100-nm TetraSpeck fluorescent bead, as a function of the relative axial position of the bead. B: Deviation of the mean estimated z value from the expected z value for the same bead as a function of its relative axial position. The expected z value is determined based on the step size used for the piezo nanopositioner. The following estimation parameter values were used: ROI size: 13×13 pixels, sub-ROI sequence $r = 2, 3, 4$. Calibration data and test data were both generated using beads from the same sample but in different fields of view. For calibration data, 10 images of the beads were acquired per detector, followed by moving the piezo nanopositioner 25 nm and repeating the process over a wide axial range. Data from six beads was used for calibration. For the test data, 50 images of the beads were acquired per detector, followed by moving the piezo nanopositioner 100 nm similarly. Per acquisition, a combined total of at least 4000 photons were detected from each calibration bead, and approximately 6000 photons were detected from the test bead, within the ROIs from the four detector images. Vertical dotted lines indicate the calculated positions of the focal planes.

4.3 DISCUSSION

The accurate estimation of the 3D location of a point source represents a fundamental problem in single molecule microscopy with significant implications for single particle tracking applications and super-resolution microscopy. MUM has provided a solution to this 3D localization problem with the use of multiple detectors that simultaneously image different focal planes and rigorous estimation algorithms like MUMLA. However, because of the relatively long processing times required by algorithms like MUMLA, a faster, easier-to-implement method may be desired. Others have implemented several related non-parametric axial localization methods which roughly abstract to comparing the relative intensities of the point source image within a small region in each detector of the MUM configuration to a lookup table.

Here we explore how much axial location information can be obtained with such intensity comparison methods by using SPB-PLAM calculations. Our observations indicate that for MUM configurations with closely-spaced focal planes (e.g., plane spacing of around 0.5 μm), a single intensity calculated with the correct sub-ROI size can indeed provide accurate axial location estimates. However, this phenomenon becomes less reliable with wider focal plane spacings, wherein a particular sub-ROI size may provide only accurate estimates for a more limited set of axial locations of the point source (Figure 4-4). Given the practical importance of using wide-spaced MUM configurations, an ideal non-parametric axial localization method needs to provide consistently accurate axial location estimates for point sources over a wide axial range.

Here we introduce a simple yet robust non-parametric axial location estimation method, MILA, that satisfies this important criterion. MILA also calculates the axial location from intensity estimates, but uses more than one intensity value from each focal plane image of the point source. Using simulations, we show that the accuracy attainable with this method can be expected to be reasonably close to the standard PLAM over a relatively large axial range (Figure 4-3).

One of the primary benefits of this method is its simplicity: the implementation of this method does not require any a priori information about the PSF of the microscope configuration and involves only arithmetic manipulation of the raw data that can be implemented using most software frameworks. This enables both easier implementation of the algorithm and faster computation times, which are often difficult to achieve when using parametric fitting algorithms like MUMLA. The computational cost is of particular interest in certain practical applications (e.g., real-time processing). Algorithms like MUMLA which have to perform complex calculations using constructs such as Bessel functions can take a significantly longer time to run than non-parametric lookup-based methods such as MILA. Even without optimization of our software implementation, we have observed MILA-based estimation to generally complete in less than a millisecond per point source on regular desktop PCs. This acceleration of processing time makes MILA an attractive choice for preliminary analyses of the data despite its lower accuracy.

MILA should also work with data from configurations implementing various PSF engineering methods, though for systems with highly asymmetric PSFs, better accuracies

might be attained if we use sub-ROIs with shapes that take advantage of the intensity characteristics of those PSFs. For example, asymmetric ROIs covering the different skew areas of an asymmetric PSF may provide more information than concentric rings.

Further, we often observe that with a sufficient number of sub-ROI combinations, the MILA estimation accuracy is reasonably close to the standard PLAM (Figure 4-3) indicating that the accuracy attained by this method might be sufficient for studies where a small compromise in axial localization accuracy is permissible. However, it is also clear that the performance of MILA and other non-parametric methods does not fully reach the practical accuracy limits, unlike that of parametric axial location estimation methods like MUMLA [96]. The standard deviation of MILA estimates also does not necessarily improve with the addition of more sub-ROIs (Figure 4-3D). This is in contrast to what is predicted by SPB-PLAM calculations (Figure 4-3C), but is not unexpected for a relatively simple estimator like MILA that does not make use of mathematical descriptions of the image data that accurately model the PSF of the microscope system, the noise characteristics of the detectors, etc. PLAM values are calculated using such mathematical descriptions, and it is thus reasonable to expect that they are more likely to be attained by more sophisticated methods like MUMLA, which uses a maximum-likelihood estimator that fully utilizes the same or similar mathematical descriptions.

When MILA was applied to data from a four-plane MUM configuration with focal planes 1.5 μm apart (Figure 4-4), we observed that using just two or three sub-ROIs was not sufficient to obtain good estimates throughout the axial range (as predicted by SPB-PLAM

calculations shown in the bottom panel of Figure 4-4B). This is in contrast to what is seen in Figure 4-3C for a MUM configuration with a 1-μm focal plane spacing, where the SPB-PLAM calculations predict relatively small differences in accuracy when small and large numbers of sub-ROIs are used. Hence, the ideal number of sub-ROIs for a particular optical configuration needs to be optimized either empirically or through Fisher information calculations to obtain the best possible MILA results.

In this study, we have used beads deposited on a coverslip as an experimental model system for both lookup table and test data generation. In biological applications, however, the test point sources may often be found several microns deeper into the sample. While beads on the coverslip may give a reasonable estimate of the PSF, this estimate nevertheless might not reflect the PSF of point sources found deeper in an aqueous sample. The calibration data for MILA may be generated using 3D bead sample preparation protocols, however, to obtain PSF estimates that more closely reflect the PSF profiles of point sources deeper in the sample.

One issue that affects non-parametric methods is the bias resulting from the differences in the sub-pixel locations of point sources in the calibration and test data. We were able to address this problem by using lookup data from multiple calibration point sources (Figure 4-6). This solution should be implementable practically, since the calibration data is often obtained using fluorescent beads and utilizing data from images of many beads in a single field of view should suffice to address this sub-pixel localization bias.

The photon budget at which an estimator is expected to perform is also of importance. Here, we tested MILA on simulated and experimental data where thousands of photons were detected from the point source per acquisition over all the detectors, as such numbers are consistent with the typical photon counts that can be expected from single dye molecules in super-resolution experiments [169]. In the case of much lower photon budgets such as what might be expected from the use of a weak fluorescent dye, the performance of MILA and other non-parametric methods may be negatively impacted by the higher levels of noise relative to the point source signal in the image pixels.

Finally, we have tested the applicability of MILA to experimental data and shown that it can accurately recapitulate the axial location of fluorescent beads. Using a four-plane MUM configuration, we were able to calculate the axial position of the beads over a range of several microns (Figure 4-7). We hope that the simplicity and versatility of this method will make it a useful tool in applications requiring the determination of the 3D location of objects of interest from MUM data.

4.4 METHODS

4.4.1 Data simulation

For simulations, images of a point source were modeled as arising from a series of pixelated detectors collecting photons from the point source through a MUM setup. In all cases the Region Of Interest (ROI) was assumed to be a sub-region in the detector with the point source situated such that its location in the image is within the center pixel of the sub-region. Unless specified otherwise, the point source location is also centered within this pixel. The number of point source photons detected in each pixel of an ROI is then simulated as Poisson realizations of mean intensity values given by the Born and Wolf model for a 3D PSF [78]. A Gaussian random variable with a mean of 80 electrons and a standard deviation of 6 electrons was added to each pixel to simulate the offset and read-out noise associated with real detectors. A Poisson-distributed background noise component with a mean of 70 photons/pixel was also added to all simulations. Simulation of images for a given detector, which captures a distinct focal plane, was carried out with the axial location parameter of the point source offset by the distance of the detector's focal plane from the design location. The mean number of photons detected from the point source was partitioned equally between the detectors (e.g., if we simulate data as arising from a four-plane MUM setup, a point source from which 8000 photons are on average detected per exposure would be simulated such that 2000 photons are on average detected by each of the four cameras). The mean number of photons detected per focal plane image is given in the caption of each figure. All data were simulated with a wavelength of 655 nm. For each dataset, an accuracy benchmark given by the standard PLAM for the z position of the

point source was calculated. The standard PLAM is calculated based on the Fisher information content of each image as is, meaning all the intensity values in the pixels of an ROI are taken into account as they are. It is the PLAM that has been observed to be approached by the standard deviation of the parametric fitting algorithm MUMLA. In contrast, a Summed-Pixel-Based PLAM (SPB-PLAM) was also calculated for each dataset that is based on the Fisher information content of a combination of subsets of the ROI, or "sub-ROIs", each represented by a single intensity value obtained as the sum of the intensities of its component pixels. An SPB-PLAM is therefore applicable to intensity-based estimation algorithms such as the sharpness method [168] and MILA.

All simulations, PLAM calculations and estimations were performed using code written in MATLAB (MathWorks, Natick, MA) that forms the core of the FandPLimitTool (http:// http://wardoberlab.com/software/fandplimittool) and the EstimationTool (http://wardoberlab.com/software/estimationtool) software packages.

4.4.2 Generation of MUM images from fluorescent beads

To test MILA on experimental data, 100-nm Tetraspeck fluorescent beads (Invitrogen, Carlsbad, CA) were imaged using a four-plane MUM setup. The beads were deposited on MatTek dishes (MatTek, Ashland, MA) pretreated with poly-L-Lysine (Sigma Aldrich) by adding a solution containing the beads for 10 minutes and then washing with water. The dish was then filled with water and imaged using a Zeiss 63× 1.4 NA Plan-Apochromat objective mounted on a piezo nanopositioner (Physik Instrumente, Auburn, MA).

Excitation light from a 150-mW, 635-nm solid state laser (OptoEngine, Midvale, UT) was reflected to the objective and the emission light filtered using a quad-band dichroic/emission filter combination (Di01-R405/488/543/635 and FF01-446/515/588/700-25, Semrock, Rochester, NY). The configuration was housed on an Axio Observer.A1 microscope body (Carl Zeiss MicroImaging, Germany). The four-plane MUM configuration was assembled as described previously [79,96] using two Zeiss dual camera adapters attached on the output ports of another dual camera adapter that is attached to the output port of the microscope body. Four Andor iXon electron-multiplying charge-coupled device (EMCCD) cameras (three iXon DV887 and one iXon DU897, Andor Technology, South Windsor, CT) were attached to the four output ports. The cameras were used to image different focal planes by modifying the length of the spacer between the output port and each camera. Beamsplitters (50/50; Chroma Technology, Bellows Falls, VT) were used to equally partition the incoming emission light between the four cameras. Data was acquired using the conventional read-out mode in all four EMCCD cameras. The cameras were synchronously controlled via TTL pulses with custom software written using LabWindows CVI (National Instruments, Austin, TX). A field of view containing a sparse distribution of beads was selected and z-stack images of this field of view were acquired using the piezo nanopositioner. The images from the different cameras were registered as follows: the lateral coordinates of three or more beads were estimated from the in-focus images of the beads from all four detectors. The coordinates from the first detector and each of the other three detectors were used to generate affine transformation matrices. The

transformation matrices were then used to register the images from the three other detectors to the coordinates of the pixels in the first detector.

ROIs of selected beads were extracted from each image as small sub-regions such that the center of the bead coincided with the center pixel of the extracted ROI. Such extracted ROIs from all four images per z-slice acquisition of each bead were processed for MILA lookup table generation and axial location estimation.

4.4.3 Identification of the pixel containing the point source location in a given ROI

For the MILA approach, we identify the pixel where the point source is located and calculate the sum intensities of different sub-ROIs around this pixel. In order to efficiently estimate the point source's axial location using this method, the identification of this pixel needs to be performed accurately. For our bead data, this was achieved by fitting a 2D Gaussian profile to the image of the bead and identifying the pixel that contains the peak of the fitted Gaussian profile. In data where the image of the bead is identifiable in multiple detectors, the image from the detector where the bead was closest to being in focus (which was determined by choosing the image where the most number of photons were detected within the ROI) was used for this estimation. For our simulation data, this step was skipped as the center pixel of the ROI was simulated to contain the point source.

4.4.4 Estimation of the axial location by MILA

MILA is implemented as follows: the pixel that contains the point source of interest is identified using the image from the detector in the MUM configuration where the point source is closest to being in focus. Pixels corresponding to concentric square-shaped

regions around this center pixel are then taken from each focal plane image (Figure 4-2A), and the intensities of the component pixels of each region are summed after background subtraction. Hence, if we choose to extract summed intensities from 3 concentric regions in images from a two-plane MUM configuration, we will have 6 intensity values. These intensity values are then normalized by dividing with the highest intensity value among them. Typical normalized intensities from such simulated data are shown as a function of axial position of the point source in Figure 4-2B. A lookup table of such normalized intensity-values is calculated from images of one or several point sources at a series of known axial positions. The number of lookup positions within the axial range is then further increased using local regression-based smoothing and interpolation methods. Normalized intensities are then similarly calculated for an unknown point source and compared to the lookup table using a least squares method to estimate the axial location of the point source (a formal description of the method is provided in Appendix 4-5). For comparison with MILA, the ratiometric method was implemented as described previously [99].

Note that in this thesis, the term "axial localization accuracy" is used synonymously with the standard deviation of the axial location estimates obtained with a method such as MILA. In plots that give a comparison of the standard deviation of estimates and the associated PLAM, it is also used as an umbrella term that encompasses both types of quantities. This more general use of the term is justifiable as the PLAM is a lower bound on the standard deviation with which the axial location of a point source can be estimated.

4.5 APPENDIX: ESTIMATING THE AXIAL LOCATION OF A POINT SOURCE USING MILA

Let us consider data collected by D pixelated detectors represented by $d = 1, \ldots, D$, each capturing the image of a different focal plane in the object space. The images from all D detectors are assumed to be aligned so that the lateral positions of each pixel correspond between all the images.

The image obtained from each detector is cropped to a small ROI so that the point source of interest is situated in the center pixel of the image. The size of the ROI is chosen such that it includes all the pixels that receive the majority of the photons from the point source. For each detector $d = 1, \ldots, D$, a background estimate B_d can be calculated through an appropriate method, such as taking the median of the edge pixels of the ROI or by using adjacent time-series images in super-resolution datasets.

We then calculate a series of intensity values from each ROI by summing the background-subtracted double-precision intensities from pixels belonging to various sub-ROIs. The shapes of the sub-ROIs chosen in this report are concentric square regions as shown in Figure 4-8. However, the shapes can be customized so that the regions of the PSF that exhibit maximal changes in intensity as a function of the point source's axial position are optimally represented in the sub-ROIs. The concentric sub-ROIs used here are represented with the sequence $r = r_1, \ldots r_P$, where the sub-ROI $r_p, p = 1, \ldots, P$, comprises all the pixels that are located within r_P pixels of the center pixel in both the x and y dimensions and are not included as part of any smaller sub-ROI in the sequence. For

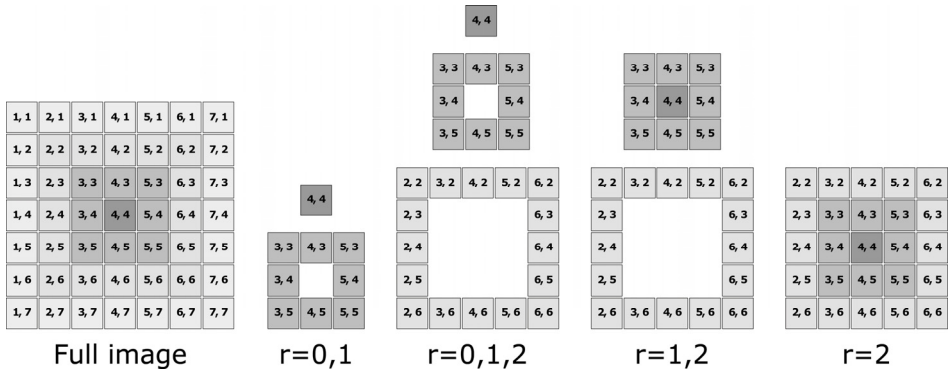

Figure 4-8: Example illustrations of different sub-ROI shapes used in MILA

example, the sequence $r = 1,2$ represents two sub-ROIs, the 3 × 3 square region around the center pixel and the next line of pixels around the 3 × 3 square region as depicted in Figure 4-8.

If A'_{d,r_p} denotes the sum of pixel intensities for sub-ROI r_P from the image of detector d, we normalize it as,

$$A_{d,r_P} = \frac{A'_{d,r_P}}{max\left\{A'_{d_1 r_{p_1}} \middle| d_1 = 1, \dots, D, p_1 = 1, \dots, P\right\}}, d = 1, \dots, D, p = 1, \dots, P.$$

In order to calculate the axial location of the point source using the normalized intensity values, we establish a lookup table by utilizing data acquired from a calibration experiment. A calibration experiment can be defined as one where we know the axial position of the point source whose images are acquired. In the case of simulations, we can simply simulate the images of point sources at various axial locations. In the case of practical experiments, the data can be acquired by recording images of a point source while linearly changing the focus of the microscope objective using a piezo nanopositioner. Thus, we acquire J sets of images per detector d, each set corresponding to a unique axial position z of the piezo nanopositioner.

The images for a point source in this calibration data can then be represented by $I_{z,d}^{lookup}, z = z_1, \dots, z_J, d = 1, \dots, D$. We then calculate the sets of normalized intensity values for each lookup position to yield $A_{z,d,r_p}^{lookup}, z = z_1, \dots z_J, d = ,1 \dots, D, p = 1, \dots, P$.

Now, given a set of images $I_d, d = 1, \ldots, D$ for an unknown point source, we can calculate an estimate $\hat{z}$ of the point source's axial location by calculating the corresponding A_{d,r_p} values and evaluating them against the lookup table to identify the value of z for which the A_{d,r_p} values are most similar to the A_{z,d,r_p}^{lookup} values:

$$\hat{z} = \underset{z \in (z_1, \ldots, z_J)}{\operatorname{argmin}} \left\{ \sum_{p=1}^{P} \sum_{d=1}^{D} \left(A_{z,d,r_p}^{lookup} - A_{d,r_p} \right)^2 \right\}.$$

The accuracy attainable with this lookup method is, however, limited by the number of z values in the lookup table (for example, if we only have a lookup value every 25 nm, then the estimated axial positions can only be calculated in relatively coarse 25-nm increments). This can be addressed by calculating the A_{z,d,r_p}^{lookup} values for more z positions between z_j and $z_{j+1}, j = 1, \ldots J - 1$, using (linear) interpolation methods. Depending on the quality of the calibration data, smoothing methods may also be used to remove deviations in the calibration curve due to local variations.

In order to address sub-pixel localization bias issues, we can utilize calibration data from multiple point sources. If we have calibration data from C point sources, then we can represent lookup tables from all these point sources as $A_{z,d,r_p}^{lookup}, z = z_1, \ldots z_J, d = ,1 \ldots, D, p = 1, \ldots, P, c = 1, \ldots, C$. Using each lookup table, we first obtain an axial location estimate as described above. Hence, when given intensities A_{d,r_p} from an unknown point source, we compute C axial location estimates:

$$z_c = \underset{z\in(z_1,\ldots,z_J)}{\operatorname{argmin}} \left\{ \sum_{p=1}^{P} \sum_{d=1}^{D} \left(A_{z,d,r_p.c}^{lookup} - A_{d,r_p} \right)^2 \right\}, c = 1, \ldots C.$$

Of all the C estimates z_c, the z_c estimate corresponding to the smallest summation value from this equation is then taken as the best estimate $\hat{z}$ for the axial location of our unknown point source.

BIBLIOGRAPHY

1. Murphy K, Weaver C: *Janeway's Immunobiology, 9th edition*. Garland Science; 2016.

2. Ademokun AA, Dunn-Walters D: *Immune Responses: Primary and Secondary*. John Wiley & Sons, Ltd; 2001.

3. Challa DK, Velmurugan R, Ober RJ, Sally Ward E: **FcRn: from molecular interactions to regulation of IgG pharmacokinetics and functions**. *Curr Top Microbiol Immunol* 2014, **382**:249–272.

4. Köhler G, Milstein C: **Continuous cultures of fused cells secreting antibody of predefined specificity.** *Nature* 1975, **256**:495–497.

5. Khazaeli MB, Conry RM, LoBuglio AF: **Human immune response to monoclonal antibodies.** *J Immunother* 1994, **15**:42–52.

6. Ober RJ, Radu CG, Ghetie V, Ward ES: **Differences in promiscuity for antibody-FcRn interactions across species: implications for therapeutic antibodies**. *Int Immunol* 2001, **13**:1551–1559.

7. Morrison SL, Johnson MJ, Herzenberg LA, Oi VT: **Chimeric human antibody molecules: mouse antigen-binding domains with human constant region domains.** *Proc Natl Acad Sci USA* 1984, **81**:6851–6855.

8. Jones PT, Dear PH, Foote J, Neuberger MS, Winter G: **Replacing the complementarity-determining regions in a human antibody with those from a mouse.** *Nature* 1986, **321**:522–525.

9. McCafferty J, Griffiths AD, Winter G, Chiswell DJ: **Phage antibodies: filamentous phage displaying antibody variable domains.** *Nature* 1990, **348**:552–554.

10. Lonberg N, Taylor LD, Harding FA, Trounstine M, Higgins KM, Schramm SR, Kuo CC, Mashayekh R, Wymore K, McCabe JG: **Antigen-specific human antibodies from mice comprising four distinct genetic modifications.** *Nature* 1994, **368**:856–859.

11. Green LL, Hardy MC, Maynard-Currie CE, Tsuda H, Louie DM, Mendez MJ, Abderrahim H, Noguchi M, Smith DH, Zeng Y, et al.: **Antigen-specific human monoclonal antibodies from mice engineered with human Ig heavy and light chain YACs.** *Nat Genet* 1994, **7**:13–21.

12. McLaughlin P, Grillo-López AJ, Link BK, Levy R, Czuczman MS, Williams ME, Heyman MR, Bence-Bruckler I, White CA, Cabanillas F, et al.: **Rituximab**

chimeric anti-CD20 monoclonal antibody therapy for relapsed indolent lymphoma: half of patients respond to a four-dose treatment program. *J Clin Oncol* 1998, **16**:2825–2833.

13. Maximiano S, Magalhães P, Guerreiro MP, Morgado M: **Trastuzumab in the Treatment of Breast Cancer.** *BioDrugs* 2016, **30**:75–86.

14. Ecker DM, Jones SD, Levine HL: **The therapeutic monoclonal antibody market.** *MAbs* 2015, **7**:9–14.

15. Hudis CA: **Trastuzumab--mechanism of action and use in clinical practice.** *N Engl J Med* 2007, **357**:39–51.

16. Gennari R, Menard S, Fagnoni F, Ponchio L, Scelsi M, Tagliabue E, Castiglioni F, Villani L, Magalotti C, Gibelli N, et al.: **Pilot study of the mechanism of action of preoperative trastuzumab in patients with primary operable breast tumors overexpressing HER2.** *Clin Cancer Res* 2004, **10**:5650–5655.

17. Varchetta S, Gibelli N, Oliviero B, Nardini E, Gennari R, Gatti G, Silva LS, Villani L, Tagliabue E, Menard S, et al.: **Elements related to heterogeneity of antibody-dependent cell cytotoxicity in patients under trastuzumab therapy for primary operable breast cancer overexpressing Her2.** *Cancer Res* 2007, **67**:11991–11999.

18. Golay J, Lazzari M, Facchinetti V, Bernasconi S, Borleri G, Barbui T, Rambaldi A, Introna M: **CD20 levels determine the in vitro susceptibility to rituximab and complement of B-cell chronic lymphocytic leukemia: further regulation by CD55 and CD59.** *Blood* 2001, **98**:3383–3389.

19. Di Gaetano N, Cittera E, Nota R, Vecchi A, Grieco V, Scanziani E, Botto M, Introna M, Golay J: **Complement activation determines the therapeutic activity of rituximab in vivo.** *J Immunol* 2003, **171**:1581–1587.

20. Leidi M, Gotti E, Bologna L, Miranda E, Rimoldi M, Sica A, Roncalli M, Palumbo GA, Introna M, Golay J: **M2 macrophages phagocytose rituximab-opsonized leukemic targets more efficiently than M1 cells in vitro**. *J Immunol* 2009, **182**:4415–4422.

21. Griffin FM, Griffin JA, Silverstein SC: **Studies on the mechanism of phagocytosis. II. The interaction of macrophages with anti-immunoglobulin IgG-coated bone marrow-derived lymphocytes.** *J Exp Med* 1976, **144**:788–809.

22. Hubert P, Heitzmann A, Viel S, Nicolas A, Sastre-Garau X, Oppezzo P, Pritsch O, Osinaga E, Amigorena S: **Antibody-dependent cell cytotoxicity synapses**

form in mice during tumor-specific antibody immunotherapy. *Cancer Res* 2011, **71**:5134–5143.

23. Gul N, Babes L, Siegmund K, Korthouwer R, Bogels M, Braster R, Vidarsson G, Hagen ten TL, Kubes P, van Egmond M: **Macrophages eliminate circulating tumor cells after monoclonal antibody therapy**. *J Clin Invest* 2014, **124**:812–823.

24. Overdijk MB, Verploegen S, Bogels M, van Egmond M, Lammerts van Bueren JJ, Mutis T, Groen RW, Breij E, Martens AC, Bleeker WK, et al.: **Antibody-mediated phagocytosis contributes to the anti-tumor activity of the therapeutic antibody daratumumab in lymphoma and multiple myeloma**. *MAbs* 2015, **7**:311–321.

25. Weiskopf K, Weissman IL: **Macrophages are critical effectors of antibody therapies for cancer**. *MAbs* 2015, **7**:303–310.

26. Taskinen M, Karjalainen-Lindsberg M-L, Nyman H, Eerola L-M, Leppä S: **A high tumor-associated macrophage content predicts favorable outcome in follicular lymphoma patients treated with rituximab and cyclophosphamide-doxorubicin-vincristine-prednisone.** *Clin Cancer Res* 2007, **13**:5784–5789.

27. Grugan KD, McCabe FL, Kinder M, Greenplate AR, Harman BC, Ekert JE, van Rooijen N, Anderson GM, Nemeth JA, Strohl WR, et al.: **Tumor-associated macrophages promote invasion while retaining Fc-dependent anti-tumor function**. *J Immunol* 2012, **189**:5457–5466.

28. Desjarlais JR, Lazar GA: **Modulation of antibody effector function.** *Exp Cell Res* 2011, **317**:1278–1285.

29. Elgundi Z, Reslan M, Cruz E, Sifniotis V, Kayser V: **The state-of-play and future of antibody therapeutics.** *Adv Drug Deliv Rev* 2016, doi:10.1016/j.addr.2016.11.004.

30. Subramaniam JM, Whiteside G, McKeage K, Croxtall JC: **Mogamulizumab: first global approval.** *Drugs* 2012, **72**:1293–1298.

31. Sachdeva M, Dhingra S: **Obinutuzumab: A FDA approved monoclonal antibody in the treatment of untreated chronic lymphocytic leukemia.** *Int J Appl Basic Med Res* 2015, **5**:54–57.

32. Lazar GA, Dang W, Karki S, Vafa O, Peng JS, Hyun L, Chan C, Chung HS, Eivazi A, Yoder SC, et al.: **Engineered antibody Fc variants with enhanced effector function**. *Proc Natl Acad Sci USA* 2006, **103**:4005–4010.

33. Richards JO, Karki S, Lazar GA, Chen H, Dang W, Desjarlais JR: **Optimization of antibody binding to FcγRIIa enhances macrophage phagocytosis of tumor cells**. *Mol Cancer Ther* 2008, **7**:2517–2527.

34. Stavenhagen JB, Gorlatov S, Tuaillon N, Rankin CT, Li H, Burke S, Huang L, Vijh S, Johnson S, Bonvini E, et al.: **Fc optimization of therapeutic antibodies enhances their ability to kill tumor cells in vitro and controls tumor expansion in vivo via low-affinity activating Fcγ receptors**. *Cancer Res* 2007, **67**:8882–8890.

35. Stewart R, Thom G, Levens M, Güler-Gane G, Holgate R, Rudd PM, Webster C, Jermutus L, Lund J: **A variant human IgG1-Fc mediates improved ADCC.** *Protein Eng Des Sel* 2011, **24**:671–678.

36. Ahmed AA, Keremane SR, Vielmetter J, Bjorkman PJ: **Structural characterization of GASDALIE Fc bound to the activating Fc receptor FcγRIIIa.** *J Struct Biol* 2016, **194**:78–89.

37. Bournazos S, Chow S-K, Abboud N, Casadevall A, Ravetch JV: **Human IgG Fc domain engineering enhances antitoxin neutralizing antibody activity.** *J Clin Invest* 2014, **124**:725–729.

38. DiLillo DJ, Ravetch JV: **Differential Fc-Receptor Engagement Drives an Anti-tumor Vaccinal Effect.** *Cell* 2015, **161**:1035–1045.

39. Jung ST, Kelton W, Kang TH, Ng DT, Andersen JT, Sandlie I, Sarkar CA, Georgiou G: **Effective phagocytosis of low Her2 tumor cell lines with engineered, aglycosylated IgG displaying high FcγRIIa affinity and selectivity**. *ACS Chem Biol* 2013, **8**:368–375.

40. Sazinsky SL, Ott RG, Silver NW, Tidor B, Ravetch JV, Wittrup KD: **Aglycosylated immunoglobulin G1 variants productively engage activating Fc receptors.** *Proc Natl Acad Sci USA* 2008, **105**:20167–20172.

41. Borrok MJ, Jung ST, Kang TH, Monzingo AF, Georgiou G: **Revisiting the role of glycosylation in the structure of human IgG Fc.** *ACS Chem Biol* 2012, **7**:1596–1602.

42. Metchnikoff O: *Life of Elie Metchnikoff*. The Floating Press; 1921.

43. Hirsch JG: **Phagocytosis.** *Annu Rev Microbiol* 1965, **19**:339–350.

44. Greenberg S, Grinstein S: **Phagocytosis and innate immunity.** *Curr Opin Immunol* 2002, **14**:136–145.

45. Flannagan RS, Jaumouillé V, Grinstein S: **The cell biology of phagocytosis.** *Annu Rev Pathol* 2012, **7**:61–98.

46. Levin R, Grinstein S, Canton J: **The life cycle of phagosomes: formation, maturation, and resolution.** *Immunol Rev* 2016, **273**:156–179.

47. Xu H, Ren D: **Lysosomal physiology.** *Annu Rev Physiol* 2015, **77**:57–80.

48. Freeman SA, Grinstein S: **Phagocytosis: receptors, signal integration, and the cytoskeleton.** *Immunol Rev* 2014, **262**:193–215.

49. Hogarth PM: **Fc Receptors: Introduction.** *Immunol Rev* 2015, **268**:1–5.

50. Bakema JE, van Egmond M: **The human immunoglobulin A Fc receptor FcαRI: a multifaceted regulator of mucosal immunity.** *Mucosal Immunol* 2011, **4**:612–624.

51. MacGlashan D: **IgE and FcεRI regulation.** *Clin Rev Allergy Immunol* 2005, **29**:49–60.

52. Nimmerjahn F, Ravetch JV: **Antibody-mediated modulation of immune responses**. *Immunol Rev* 2010, **236**:265–275.

53. Nimmerjahn F, Ravetch JV: **Fcγ receptors as regulators of immune responses**. *Nat Rev Immunol* 2008, **8**:34–47.

54. Hogarth PM, Pietersz GA: **Fc receptor-targeted therapies for the treatment of inflammation, cancer and beyond**. *Nat Rev Drug Discov* 2012, **11**:311–331.

55. Ghiran I, Barbashov SF, Klickstein LB, Tas SW, Jensenius JC, Nicholson-Weller A: **Complement receptor 1/CD35 is a receptor for mannan-binding lectin.** *J Exp Med* 2000, **192**:1797–1808.

56. Ross GD, Reed W, Dalzell JG, Becker SE, Hogg N: **Macrophage cytoskeleton association with CR3 and CR4 regulates receptor mobility and phagocytosis of iC3b-opsonized erythrocytes.** *J Leukoc Biol* 1992, **51**:109–117.

57. Humphries JD: **Integrin ligands at a glance**. *J Cell Sci* 2006, **119**:3901–3903.

58. Brubaker SW, Bonham KS, Zanoni I, Kagan JC: **Innate immune pattern recognition: a cell biological perspective.** *Annu Rev Immunol* 2015, **33**:257–290.

59. Green DR: *Means to an end: apoptosis and other cell death mechanisms*. Cold Spring Harbor Laboratory Press; 2011.

60. Crowley MT, Costello PS, Fitzer-Attas CJ, Turner M, Meng F, Lowell C, Tybulewicz VL, DeFranco AL: **A critical role for Syk in signal transduction and phagocytosis mediated by Fcγ receptors on macrophages.** *J Exp Med* 1997, **186**:1027–1039.

61. Desjardins M, Huber LA, Parton RG, Griffiths G: **Biogenesis of phagolysosomes proceeds through a sequential series of interactions with the endocytic apparatus.** *J Cell Biol* 1994, **124**:677–688.

62. Lukacs GL, Rotstein OD, Grinstein S: **Determinants of the phagosomal pH in macrophages. In situ assessment of vacuolar H(+)-ATPase activity, counterion conductance, and H+ "leak".** *J Biol Chem* 1991, **266**:24540–24548.

63. Savina A, Jancic C, Hugues S, Guermonprez P, Vargas P, Moura IC, Lennon-Duménil A-M, Seabra MC, Raposo G, Amigorena S: **NOX2 controls phagosomal pH to regulate antigen processing during crosspresentation by dendritic cells.** *Cell* 2006, **126**:205–218.

64. Joly E, Hudrisier D: **What is trogocytosis and what is its purpose?** *Nat Immunol* 2003, **4**:815–815.

65. Miller RA, Maloney DG, Warnke R, Levy R: **Treatment of B-cell lymphoma with monoclonal anti-idiotype antibody.** *N Engl J Med* 1982, **306**:517–522.

66. Adams GP, Weiner LM: **Monoclonal antibody therapy of cancer.** *Nat Biotechnol* 2005, **23**:1147–1157.

67. Kennedy AD, Beum PV, Solga MD, DiLillo DJ, Lindorfer MA, Hess CE, Densmore JJ, Williams ME, Taylor RP: **Rituximab infusion promotes rapid complement depletion and acute CD20 loss in chronic lymphocytic leukemia.** *J Immunol* 2004, **172**:3280–3288.

68. Beum PV, Lindorfer MA, Taylor RP: **Within peripheral blood mononuclear cells, antibody-dependent cellular cytotoxicity of rituximab-opsonized Daudi cells is promoted by NK cells and inhibited by monocytes due to shaving.** *J Immunol* 2008, **181**:2916–2924.

69. Beum PV, Mack DA, Pawluczkowycz AW, Lindorfer MA, Taylor RP: **Binding of rituximab, trastuzumab, cetuximab, or mAb T101 to cancer cells promotes trogocytosis mediated by THP-1 cells and monocytes.** *J Immunol* 2008, **181**:8120–8132.

70. Beum PV, Peek EM, Lindorfer MA, Beurskens FJ, Engelberts PJ, Parren PW, van de Winkel JG, Taylor RP: **Loss of CD20 and bound CD20 antibody from**

opsonized B cells occurs more rapidly because of trogocytosis mediated by Fc receptor-expressing effector cells than direct internalization by the B cells. *J Immunol* 2011, **187**:3438–3447.

71. Taylor RP: **Gnawing at Metchnikoff's paradigm**. *Blood* 2013, **122**:2922–2924.

72. Rossi EA, Goldenberg DM, Michel R, Rossi DL, Wallace DJ, Chang C-H: **Trogocytosis of multiple B-cell surface markers by CD22 targeting with epratuzumab.** *Blood* 2013, **122**:3020–3029.

73. Taylor RP, Lindorfer MA: **Fcγ-receptor-mediated trogocytosis impacts mAb-based therapies: historical precedence and recent developments**. *Blood* 2015, **125**:762–766.

74. Campana S, De Pasquale C, Carrega P, Ferlazzo G, Bonaccorsi I: **Cross-dressing: an alternative mechanism for antigen presentation.** *Immunol Lett* 2015, **168**:349–354.

75. Huang JF, Yang Y, Sepulveda H, Shi W, Hwang I, Peterson PA, Jackson MR, Sprent J, Cai Z: **TCR-Mediated internalization of peptide-MHC complexes acquired by T cells.** *Science* 1999, **286**:952–954.

76. Ralston KS, Solga MD, Mackey-Lawrence NM, Somlata, Bhattacharya A, Petri WAJ: **Trogocytosis by Entamoeba histolytica contributes to cell killing and tissue invasion**. *Nature* 2014, **508**:526–530.

77. Lichtman JW, Conchello J-A: **Fluorescence microscopy**. *Nat Meth* 2005, **2**:910–919.

78. Born M, Wolf E: *Principles of Optics*. Cambridge University press; 1999.

79. Prabhat P, Ram S, Ward ES, Ober RJ: **Simultaneous imaging of different focal planes in fluorescence microscopy for the study of cellular dynamics in three dimensions**. *IEEE Trans Nanobioscience* 2004, **3**:237–242.

80. Prabhat P, Ram S, Ward ES, Ober RJ: **Simultaneous imaging of several focal planes in fluorescence microscopy for the study of cellular dynamics in 3D**. *Proc SPIE* 2006, **6090**:115–121.

81. Prabhat P, Gan Z, Chao J, Ram S, Vaccaro C, Gibbons S, Ober RJ, Ward ES: **Elucidation of intracellular recycling pathways leading to exocytosis of the Fc receptor, FcRn, by using multifocal plane microscopy**. *Proc Natl Acad Sci USA* 2007, **104**:5889–5894.

82. Gan Z, Ram S, Ober RJ, Ward ES: **Using multifocal plane microscopy to**

reveal novel trafficking processes in the recycling pathway. *J Cell Sci* 2013, **126**:1176–1188.

83. Ober RJ, Ram S, Ward ES: **Localization accuracy in single-molecule microscopy**. *Biophys J* 2004, **86**:1185–1200.

84. Saxton M, Jacobson K: **Single-particle tracking: applications to membrane dynamics**. *Annu Rev Biophys Biomol Struct* 1997, **26**:373–399.

85. Betzig E, Patterson GH, Sougrat R, Lindwasser OW, Olenych S, Bonifacino JS, Davidson MW, Lippincott-Schwartz J, Hess HF: **Imaging intracellular fluorescent proteins at nanometer resolution**. *Science* 2006, **313**:1642–1645.

86. Rust MJ, Bates M, Zhuang X: **Sub-diffraction-limit imaging by stochastic optical reconstruction microscopy (STORM)**. *Nat Meth* 2006, **3**:793–795.

87. Hess ST, Gould TJ, Gudheti MV, Maas SA, Mills KD, Zimmerberg J: **Dynamic clustered distribution of hemagglutinin resolved at 40 nm in living cell membranes discriminates between raft theories**. *Proc Natl Acad Sci USA* 2007, **104**:17370–17375.

88. Abraham AV, Ram S, Chao J, Ward ES, Ober RJ: **Quantitative study of single molecule location estimation techniques**. *Opt Exp* 2009, **17**:23352–23373.

89. Stallinga S, Rieger B: **Position and orientation estimation of fixed dipole emitters using an effective Hermite point spread function model.** *Opt Exp* 2012, **20**:5896–5921.

90. Zhang B, Zerubia J, Olivo-Marin J-C: **Gaussian approximations of fluorescence microscope point-spread function models.** *Appl Opt* 2007, **46**:1819–1829.

91. Gibson S, Lanni F: **Diffraction by a circular aperture as a model for three-dimensional optical microscopy**. *J Opt Soc Am* 1989, **6**:1357–1367.

92. Gibson S, Lanni F: **Experimental test of an analytical model of aberration in an oil-Immersion objective lens used in three-dimensional light microscopy**. *J Opt Soc Am* 1991, **8**:1601–1613.

93. Ram S, Ward ES, Ober RJ: **How accurately can a single molecule be localized in three dimensions using a fluorescence microscope?** *Proc SPIE* 2005, **5699**:426–435.

94. Pavani SR, Thompson MA, Biteen JS, Lord SJ, Liu N, Twieg RJ, Piestun R, Moerner WE: **Three-dimensional, single-molecule fluorescence imaging**

beyond the diffraction limit by using a double-helix point spread function. *Proc Natl Acad Sci USA* 2009, **106**:2995–2999.

95. Kao HP, Verkman AS: **Tracking of single fluorescent particles in three dimensions: use of cylindrical optics to encode particle position**. *Biophys J* 1994, **67**:1291–1300.

96. Ram S, Prabhat P, Chao J, Ward ES, Ober RJ: **High accuracy 3D quantum dot tracking with multifocal plane microscopy for the study of fast intracellular dynamics in live cells**. *Biophys J* 2008, **95**:6025–6043.

97. Tahmasbi A, Ram S, Chao J, Abraham AV, Ward ES, Ober RJ: **An information-theoretic approach to designing the plane spacing for multifocal plane microscopy.** *Proc SPIE Int Soc Opt Eng* 2015, **9330**:933011.

98. Ram S, Kim D, Ober RJ, Ward ES: **3D single molecule tracking with multifocal plane microscopy reveals rapid intercellular transferrin transport at epithelial cell barriers**. *Biophys J* 2012, **103**:1594–1603.

99. Watanabe TM, Sato T, Gonda K, Higuchi H: **Three-dimensional nanometry of vesicle transport in living cells using dual-focus imaging optics**. *Biochem Biophys Res Commun* 2007, **359**:1–7.

100. Dalgarno PA, Dalgarno HIC, Putoud A, Lambert R, Paterson L, Logan DC, Towers DP, Warburton RJ, Greenaway AH: **Multiplane imaging and three dimensional nanoscale particle tracking in biological microscopy.** *Opt Exp* 2010, **18**:877–884.

101. Williams ME, Densmore JJ, Pawluczkowycz AW, Beum PV, Kennedy AD, Lindorfer MA, Hamil SH, Eggleton JC, Taylor RP: **Thrice-weekly low-dose rituximab decreases CD20 loss via shaving and promotes enhanced targeting in chronic lymphocytic leukemia.** *J Immunol* 2006, **177**:7435–7443.

102. Daubeuf S, Lindorfer MA, Taylor RP, Joly E, Hudrisier D: **The direction of plasma membrane exchange between lymphocytes and accessory cells by trogocytosis is influenced by the nature of the accessory cell**. *J Immunol* 2010, **184**:1897–1908.

103. Chao MP, Alizadeh AA, Tang C, Myklebust JH, Varghese B, Gill S, Jan M, Cha AC, Chan CK, Tan BT, et al.: **Anti-CD47 antibody synergizes with rituximab to promote phagocytosis and eradicate non-Hodgkin lymphoma**. *Cell* 2010, **142**:699–713.

104. Pham T, Mero P, Booth JW: **Dynamics of macrophage trogocytosis of rituximab-coated B cells**. *PLoS One* 2011, **6**:e14498.

105. Boross P, Jansen JH, Pastula A, van der Poel CE, Leusen JH: **Both activating and inhibitory Fcγ receptors mediate rituximab-induced trogocytosis of CD20 in mice**. *Immunol Lett* 2012, **143**:44–52.

106. Desjarlais JR, Lazar GA, Zhukovsky EA, Chu SY: **Optimizing engagement of the immune system by anti-tumor antibodies: an engineer's perspective**. *Drug Discov Today* 2007, **12**:898–910.

107. Herter S, Birk MC, Klein C, Gerdes C, Umana P, Bacac M: **Glycoengineering of therapeutic antibodies enhances monocyte/macrophage-mediated phagocytosis and cytotoxicity**. *J Immunol* 2014, **192**:2252–2260.

108. Herter S, Herting F, Mundigl O, Waldhauer I, Weinzierl T, Fauti T, Muth G, Ziegler-Landesberger D, Van Puijenbroek E, Lang S, et al.: **Preclinical activity of the type II CD20 antibody GA101 (obinutuzumab) compared with rituximab and ofatumumab in vitro and in xenograft models**. *Mol Cancer Ther* 2013, **12**:2031–2042.

109. Scott AM, Wolchok JD, Old LJ: **Antibody therapy of cancer**. *Nat Rev Cancer* 2012, **12**:278–287.

110. Trombetta ES, Mellman I: **Cell biology of antigen processing in vitro and in vivo**. *Annu Rev Immunol* 2005, **23**:975–1028.

111. Tseng D, Volkmer JP, Willingham SB, Contreras-Trujillo H, Fathman JW, Fernhoff NB, Seita J, Inlay MA, Weiskopf K, Miyanishi M, et al.: **Anti-CD47 antibody-mediated phagocytosis of cancer by macrophages primes an effective antitumor T-cell response**. *Proc Natl Acad Sci USA* 2013, **110**:11103–11108.

112. Brown AC, Oddos S, Dobbie IM, Alakoskela JM, Parton RM, Eissmann P, Neil MA, Dunsby C, French PM, Davis I, et al.: **Remodelling of cortical actin where lytic granules dock at natural killer cell immune synapses revealed by super-resolution microscopy**. *PLoS Biol* 2011, **9**:e1001152.

113. Cretella D, Saccani F, Quaini F, Frati C, Lagrasta C, Bonelli M, Caffarra C, Cavazzoni A, Fumarola C, Galetti M, et al.: **Trastuzumab emtansine is active on HER-2 overexpressing NSCLC cell lines and overcomes gefitinib resistance**. *Mol Cancer* 2014, **13**:143.

114. Kang JC, Poovassery JS, Bansal P, You S, Manjarres IM, Ober RJ, Ward ES: **Engineering multivalent antibodies to target heregulin-induced HER3 signaling in breast cancer cells**. *MAbs* 2014, **6**:340–453.

115. Lefebvre ML, Krause SW, Salcedo M, Nardin A: **Ex vivo-activated human**

macrophages kill chronic lymphocytic leukemia cells in the presence of rituximab: mechanism of antibody-dependent cellular cytotoxicity and impact of human serum. *J Immunother* 2006, **29**:388–397.

116. Agus DB, Akita RW, Fox WD, Lewis GD, Higgins B, Pisacane PI, Lofgren JA, Tindell C, Evans DP, Maiese K, et al.: **Targeting ligand-activated ErbB2 signaling inhibits breast and prostate tumor growth**. *Cancer Cell* 2002, **2**:127–137.

117. Franklin MC, Carey KD, Vajdos FF, Leahy DJ, de Vos AM, Sliwkowski MX: **Insights into ErbB signaling from the structure of the ErbB2-pertuzumab complex**. *Cancer Cell* 2004, **5**:317–328.

118. Cho HS, Mason K, Ramyar KX, Stanley AM, Gabelli SB, Denney DWJ, Leahy DJ: **Structure of the extracellular region of HER2 alone and in complex with the Herceptin Fab**. *Nature* 2003, **421**:756–760.

119. Taylor RB, Duffus WP, Raff MC, de Petris S: **Redistribution and pinocytosis of lymphocyte surface immunoglobulin molecules induced by anti-immunoglobulin antibody.** *Nat New Biol* 1971, **233**:225–229.

120. Nimmerjahn F, Ravetch JV: **Divergent immunoglobulin G subclass activity through selective Fc receptor binding**. *Science* 2005, **310**:1510–1512.

121. Smith P, DiLillo DJ, Bournazos S, Li F, Ravetch JV: **Mouse model recapitulating human Fcγ receptor structural and functional diversity**. *Proc Natl Acad Sci USA* 2012, **109**:6181–6186.

122. Qian BZ, Pollard JW: **Macrophage diversity enhances tumor progression and metastasis**. *Cell* 2010, **141**:39–51.

123. Michel RB, Mattes MJ: **Intracellular accumulation of the anti-CD20 antibody 1F5 in B-lymphoma cells.** *Clin Cancer Res* 2002, **8**:2701–2713.

124. Rudnicka D, Oszmiana A, Finch DK, Strickland I, Schofield DJ, Lowe DC, Sleeman MA, Davis DM: **Rituximab causes a polarization of B cells that augments its therapeutic function in NK-cell-mediated antibody-dependent cellular cytotoxicity**. *Blood* 2013, **121**:4694–4702.

125. Taylor RP, Lindorfer MA: **Analyses of CD20 monoclonal antibody-mediated tumor cell killing mechanisms: rational design of dosing strategies**. *Mol Pharmacol* 2014, **86**:485–491.

126. Shi Y, Fan X, Deng H, Brezski RJ, Rycyzyn M, Jordan RE, Strohl WR, Zou Q, Zhang N, An Z: **Trastuzumab triggers phagocytic killing of high HER2**

cancer cells in vitro and in vivo by interaction with Fcγ receptors on macrophages. *J Immunol* 2015, **194**:4379–4386.

127. Blum JS, Wearsch PA, Cresswell P: **Pathways of antigen processing**. *Annu Rev Immunol* 2013, **31**:443–473.

128. Nakamura K, Nakayama M, Kawano M, Amagai R, Ishii T, Harigae H, Ogasawara K: **Fratricide of natural killer cells dressed with tumor-derived NKG2D ligand**. *Proc Natl Acad Sci USA* 2013, **110**:9421–9426.

129. Ahmed KA, Munegowda MA, Xie Y, Xiang J: **Intercellular trogocytosis plays an important role in modulation of immune responses**. *Cell Mol Immunol* 2008, **5**:261–269.

130. Davis DM: **Mechanisms and functions for the duration of intercellular contacts made by lymphocytes**. *Nat Rev Immunol* 2009, **9**:543–555.

131. Ober RJ, Martinez C, Vaccaro C, Zhou J, Ward ES: **Visualizing the site and dynamics of IgG salvage by the MHC class I-related receptor, FcRn**. *J Immunol* 2004, **172**:2021–2029.

132. Horton RM, Hunt HD, Ho SN, Pullen JK, Pease LR: **Engineering hybrid genes without the use of restriction enzymes: gene splicing by overlap extension**. *Gene* 1989, **77**:61–68.

133. Gan Z, Ram S, Vaccaro C, Ober RJ, Ward ES: **Analyses of the recycling receptor, FcRn, in live cells reveal novel pathways for lysosomal delivery**. *Traffic* 2009, **10**:600–614.

134. Chao J, Ward ES, Ober RJ: **A software framework for the analysis of complex microscopy image data**. *IEEE Trans Inf Technol Biomed* 2010, **14**:1075–1087.

135. Segal AW, Geisow M, Garcia R, Harper A, Miller R: **The respiratory burst of phagocytic cells is associated with a rise in vacuolar pH.** *Nature* 1981, **290**:406–409.

136. Saxton RA, Sabatini DM: **mTOR Signaling in Growth, Metabolism, and Disease.** *Cell* 2017, **168**:960–976.

137. Puertollano R: **mTOR and lysosome regulation**. *F1000Prime Rep* 2014, **6**:52.

138. Zoncu R, Bar-Peled L, Efeyan A, Wang S, Sancak Y, Sabatini DM: **mTORC1 senses lysosomal amino acids through an inside-out mechanism that requires the vacuolar H(+)-ATPase.** *Science* 2011, **334**:678–683.

139. Krajcovic M, Krishna S, Akkari L, Joyce JA, Overholtzer M: **mTOR regulates**

phagosome and entotic vacuole fission. *Mol Biol Cell* 2013, **24**:3736–3745.

140. Braster R, O'Toole T, van Egmond M: **Myeloid cells as effector cells for monoclonal antibody therapy of cancer.** *Methods* 2014, **65**:28–37.

141. Noy R, Pollard JW: **Tumor-Associated Macrophages: From Mechanisms to Therapy**. *Immunity* 2014, **41**:49–61.

142. Velmurugan R, Challa DK, Ram S, Ober RJ, Ward ES: **Macrophage-Mediated Trogocytosis Leads to Death of Antibody-Opsonized Tumor Cells.** *Mol Cancer Ther* 2016, **15**:1879–1889.

143. Mantegazza AR, Magalhaes JG, Amigorena S, Marks MS: **Presentation of phagocytosed antigens by MHC class I and II.** *Traffic* 2013, **14**:135–152.

144. Chazotte B: **Labeling lysosomes in live cells with LysoTracker.** *Cold Spring Harb Protoc* 2011, **2011**:pdb.prot5571.

145. Lin HJ, Herman P, Kang JS, Lakowicz JR: **Fluorescence lifetime characterization of novel low-pH probes.** *Anal Biochem* 2001, **294**:118–125.

146. Brooks CR, Yeung MY, Brooks YS, Chen H, Ichimura T, Henderson JM, Bonventre JV: **KIM-1-/TIM-1-mediated phagocytosis links ATG5-/ULK1-dependent clearance of apoptotic cells to antigen presentation.** *EMBO J* 2015, **34**:2441–2464.

147. Spence M, Johnson ID: *The molecular probes handbook: a guide to fluorescent probes and labeling technologies*. Molecular Probes; 2010.

148. Kasmapour B, Gronow A, Bleck CKE, Hong W, Gutierrez MG: **Size-dependent mechanism of cargo sorting during lysosome-phagosome fusion is controlled by Rab34.** *Proc Natl Acad Sci USA* 2012, **109**:20485–20490.

149. Berthiaume EP, Medina C, Swanson JA: **Molecular size-fractionation during endocytosis in macrophages.** *J Cell Biol* 1995, **129**:989–998.

150. Muraille E, Gounon P, Cazareth J, Hoebeke J, Lippuner C, Davalos-Misslitz A, Aebischer T, Muller S, Glaichenhaus N, Mougneau E: **Direct visualization of peptide/MHC complexes at the surface and in the intracellular compartments of cells infected in vivo by Leishmania major.** *PLoS Pathog* 2010, **6**:e1001154.

151. Han J, Burgess K: **Fluorescent Indicators for Intracellular pH**. *Chem Rev* 2010, **110**:2709–2728.

152. Desjardins M, Nzala NN, Corsini R, Rondeau C: **Maturation of phagosomes is**

accompanied by changes in their fusion properties and size-selective acquisition of solute materials from endosomes. *J Cell Sci* 1997, **110 (Pt 18)**:2303–2314.

153. Bright NA, Davis LJ, Luzio JP: **Endolysosomes Are the Principal Intracellular Sites of Acid Hydrolase Activity.** *Curr Biol* 2016, **26**:2233–2245.

154. Milo R: **What is the total number of protein molecules per cell volume? A call to rethink some published values.** *BioEssays* 2013, **35**:1050–1055.

155. Sardiello M, Palmieri M, di Ronza A, Medina DL, Valenza M, Gennarino VA, Di Malta C, Donaudy F, Embrione V, Polishchuk RS, et al.: **A gene network regulating lysosomal biogenesis and function.** *Science* 2009, **325**:473–477.

156. Michaillat L, Baars TL, Mayer A: **Cell-free reconstitution of vacuole membrane fragmentation reveals regulation of vacuole size and number by TORC1.** *Mol Biol Cell* 2012, **23**:881–895.

157. Krishna S, Palm W, Lee Y, Yang W, Bandyopadhyay U, Xu H, Florey O, Thompson CB, Overholtzer M: **PIKfyve Regulates Vacuole Maturation and Nutrient Recovery following Engulfment.** *Dev Cell* 2016, **38**:536–547.

158. Tassin MT, Lang T, Antoine JC, Hellio R, Ryter A: **Modified lysosomal compartment as carrier of slowly and non-degradable tracers in macrophages.** *Eur J Cell Biol* 1990, **52**:219–228.

159. Astarie-Dequeker C, Carreno S, Cougoule C, Maridonneau-Parini I: **The protein tyrosine kinase Hck is located on lysosomal vesicles that are physically and functionally distinct from CD63-positive lysosomes in human macrophages.** *J Cell Sci* 2002, **115**:81–89.

160. Lennon-Duménil A-M, Bakker AH, Maehr R, Fiebiger E, Overkleeft HS, Rosemblatt M, Ploegh HL, Lagaudrière-Gesbert C: **Analysis of protease activity in live antigen-presenting cells shows regulation of the phagosomal proteolytic contents during dendritic cell activation.** *J Exp Med* 2002, **196**:529–540.

161. Wagner CS, Grotzke J, Cresswell P: **Intracellular regulation of cross-presentation during dendritic cell maturation.** *PLoS One* 2013, **8**:e76801.

162. Lin K-M, Hu W, Troutman TD, Jennings M, Brewer T, Li X, Nanda S, Cohen P, Thomas JA, Pasare C: **IRAK-1 bypasses priming and directly links TLRs to rapid NLRP3 inflammasome activation.** *Proc Natl Acad Sci USA* 2014, **111**:775–780.

163. Vaccaro C, Bawdon R, Wanjie S, Ober RJ, Ward ES: **Divergent activities of an engineered antibody in murine and human systems have implications for therapeutic antibodies**. *Proc Natl Acad Sci USA* 2006, **103**:18709–18714.

164. Abrahamsson S, Chen J, Hajj B, Stallinga S, Katsov AY, Wisniewski J, Mizuguchi G, Soule P, Mueller F, Dugast Darzacq C, et al.: **Fast multicolor 3D imaging using aberration-corrected multifocus microscopy.** *Nat Meth* 2013, **10**:60–63.

165. Lew MD, Lee SF, Badieirostami M, Moerner WE: **Corkscrew point spread function for far-field three-dimensional nanoscale localization of pointlike objects.** *Opt Letts* 2011, **36**:202–204.

166. Shtengel G, Galbraith JA, Galbraith CG, Lippincott-Schwartz J, Gillette JM, Manley S, Sougrat R, Waterman CM, Kanchanawong P, Davidson MW, et al.: **Interferometric fluorescent super-resolution microscopy resolves 3D cellular ultrastructure.** *Proc Natl Acad Sci USA* 2009, **106**:3125–3130.

167. Ram S, Chao J, Prabhat P, Ward ES, Ober RJ: **A novel approach to determining the three-dimensional location of microscopic objects with applications to 3D particle tracking**. 2007, **6443**:D1–D7.

168. Dalgarno HIC, Dalgarno PA, Dada AC, Towers CE, Gibson GJ, Parton RM, Davis I, Warburton RJ, Greenaway AH: **Nanometric depth resolution from multi-focal images in microscopy.** *J R Soc Interface* 2011, **8**:942–951.

169. Dempsey GT, Vaughan JC, Chen KH, Bates M, Zhuang X: **Evaluation of fluorophores for optimal performance in localization-based super-resolution imaging.** *Nat Meth* 2011, **8**:1027–1036.